

Magnetic Stability of Single Lanthanide Atoms on Graphene

THÈSE N° 8342 (2018)

PRÉSENTÉE LE 26 JANVIER 2018
À LA FACULTÉ DES SCIENCES DE BASE
LABORATOIRE DE NANOSTRUCTURES SUPERFICIELLES
PROGRAMME DOCTORAL EN PHYSIQUE

ÉCOLE POLYTECHNIQUE FÉDÉRALE DE LAUSANNE

POUR L'OBTENTION DU GRADE DE DOCTEUR ÈS SCIENCES

PAR

Romana BALTIC

acceptée sur proposition du jury:

Prof. C. Hébert, présidente du jury
Prof. H. Brune, Dr S. Rusponi, directeurs de thèse
Prof. F. Nolting, rapporteur
Dr T. Lau, rapporteur
Prof. O. Yazyev, rapporteur



ÉCOLE POLYTECHNIQUE
FÉDÉRALE DE LAUSANNE

Suisse
2018

Mami i Julianu

Abstract

This thesis presents a study of the magnetism of surface supported atoms performed principally with XMCD spectroscopy and multiplet calculations. The objective of the research was twofold: first, to study the underlying interactions and conditions governing the magnetization stability of surface supported atoms, with the aim of achieving long magnetic lifetimes, and second, to assemble single atom magnets in an ordered pattern.

Through our study of $4f$ lanthanide atoms on supporting substrates, we established that their magnetic stability is governed by their quantum level structure, in particular their ground J_z state and the height of the energy barrier for thermally assisted magnetization reversal. These features are ruled through the crystal field interaction with their supporting surface. The adsorption site of adatoms governs the symmetry of the crystal field and, consequently, the coupling between the different J_z levels. This in turn enables magnetization reversal either through quantum tunneling between J_z states or via scattering with the electrons and phonons of the substrate. To reduce the scattering events, it is necessary to decouple the adatoms from the metal substrate by using decoupling layers. Here we show that a single layer of graphene is sufficient to decouple Dy atoms from the underlying Ir(111) substrate, resulting in a magnetic lifetime of about 1000 s at 2.5 K. In addition, we show that the moiré pattern of the graphene/Ir(111) surface can be used as a template for the self-assembly of these single atom magnets into well ordered superlattices. Further, by studying multiple graphene/metal substrates we show that the interaction of graphene with the supporting substrate greatly influences the magnetization stability of adsorbed atoms. Finally, we show that replacing graphene with an insulating layer does not result in a stable magnetization of adsorbed atoms if its superior decoupling is not accompanied with an adequate crystal field symmetry.

Key words: XAS, XMCD, multiplet calculations, single atom magnets, lanthanides, self-assembly, superlattice, graphene, moiré, crystal field, QTM

Résumé

Cette thèse présente une étude des propriétés magnétiques d'atomes supportés en surface, effectuée principalement avec spectroscopie XMCD et calculs de multiplets. L'objectif de la recherche comprend deux parties ; premièrement, l'étude des interactions sous-jacentes et les conditions gouvernant la stabilité magnétique d'atomes supportés en surface, avec comme but la recherche de longues durées de vie magnétiques, puis, l'assemblage d'aimants d'atomes uniques en une structure ordonnée.

Notre étude des atomes lanthanides $4f$ sur substrats, nous a permis d'établir que la stabilité de ces derniers est déterminée par leur structure de niveaux quantiques, plus particulièrement leur état J_z non-excité et la hauteur de la barrière d'énergie pour l'inversion magnétique assistée thermiquement. Ces facteurs sont dépendant de l'interaction du champ cristallin avec la surface qui le supporte. Les sites d'adsorption des atomes ajoutés gouvernent la symétrie du champ cristallin, et en conséquence le couplage entre les différents niveaux J_z . Il en découle la possibilité de renversement magnétique soit par effet tunnel entre les états J_z , soit par dispersion avec les électrons et les phonons du substrat. Afin de réduire les événements de dispersion, il est nécessaire de découpler les atomes ajoutés du substrat métallique en utilisant des couches de découplage. Ici, nous montrons qu'une seule couche de graphène est suffisante pour découpler les atomes de Dy du substrat Ir(111) sous-jacent, ce qui résulte en une durée de vie magnétique d'environ 1000 s à 2.5 K. En plus, nous montrons que le motif Moiré de la surface graphène/Ir(111) peut être utilisé comme matrice pour l'auto-assemblage de ces aimants à atome unique en super-réseaux bien ordonnés. En étudiant de multiples substrats graphène/métal, nous montrons que l'interaction du graphène avec le substrat sous-jacent a une grande influence sur la stabilité magnétique des atomes adsorbés. Finalement, nous montrons que le remplacement du graphène par une couche isolante ne résulte pas en une stabilité magnétique des atomes adsorbés si le découplage supérieur n'est pas accompagné par une symétrie du champ cristallin adéquate.

Mots clefs : XAS, XMCD, calculs de multiplets, aimant à atome unique, lanthanides, auto-assemblage, super-réseau, graphène, Moiré, champ cristallin, QTM

Contents

Abstract (English/Français)	i
List of figures	ix
List of tables	xi
Introduction	1
1 Magnetism of surface adsorbed atoms	5
1.1 Origin of magnetism in free atoms	5
1.2 Atom in a crystal field	6
1.2.1 Crystal field Hamiltonian	7
1.2.2 Magnetic levels in C_{3v} and C_{6v} crystal field symmetry	8
1.2.3 Quantum tunneling of magnetization in lanthanide atoms	10
1.2.4 Scattering with electrons and phonons in lanthanide atoms	11
1.3 Atom in a magnetic field	12
2 Methods	15
2.1 XAS and XMCD spectroscopy	15
2.1.1 Transition probability	15
2.1.2 Dipole selection rules	17
2.2 XMLD spectroscopy	17
2.3 Experimental aspects	18
2.3.1 Spectral analysis	18
2.3.2 Experimental setup and measurements	20
2.3.3 Sample preparation	21
2.4 Multiplet calculations	23
2.5 Scanning Tunneling Microscopy	24
3 Dy atoms on graphene/Ir(111)	25
3.1 Moiré pattern of graphene/Ir(111)	25
3.2 STM measurements of Dy on graphene/Ir(111)	26
3.2.1 Disordered Dy on graphene/Ir(111)	26
3.2.2 Self-assembly of Dy superlattice on graphene/Ir(111)	26
3.2.3 Adsorption site of Dy on graphene/Ir(111)	29

Contents

3.2.4	Dy monomers and dimers	30
3.3	XMCD measurements for Dy atoms on graphene/Ir(111)	32
3.3.1	Magnetism of Dy atoms on graphene/Ir(111)	32
3.3.2	Magnetic lifetime of Dy atoms on graphene/Ir(111)	36
3.4	Multiplet calculations for Dy atoms on graphene/Ir(111)	38
3.5	Steps in Dy hysteresis	42
3.6	Temperature dependence of Dy magnetic lifetime	44
3.7	Coverage dependent measurements	44
3.7.1	Coverage dependence of Dy XAS spectra	44
3.7.2	Coverage dependence of Dy magnetization curve	47
3.8	Exposure time dependence of Dy XAS spectra	48
3.9	Coverage calibration	48
4	Dy on Ir(111) and several decoupling substrates	51
4.1	Dy atoms on Ir(111)	51
4.2	Dy on graphene/Cu foil	53
4.2.1	Preparation of graphene/Cu substrate	53
4.2.2	Magnetism of Dy atoms on graphene/Cu foil	54
4.3	Dy on graphene/Ru(0001)	57
4.3.1	Properties of graphene/Ru(0001)	57
4.3.2	Magnetism of Dy atoms on graphene/Ru(0001)	57
4.4	Dy on HOPG	60
4.4.1	Properties of HOPG	60
4.4.2	Magnetism of Dy atoms on HOPG	61
4.4.3	Magnetic lifetime of Dy atoms on HOPG	63
4.5	Dy on <i>h</i> -BN/Ir(111)	64
4.5.1	Properties of <i>h</i> -BN	64
4.5.2	Magnetism of Dy atoms on <i>h</i> -BN/Ir(111)	64
5	Magnetism of Nd, Ho, Er and Tb on graphene/Ir(111)	69
5.1	Nd on graphene/Ir(111)	69
5.2	Ho on graphene/Ir(111)	73
5.3	Er on graphene/Ir(111)	77
5.4	Tb on graphene/Ir(111)	80
5.5	4 <i>f</i> occupation of lanthanides on graphene/Ir(111)	84
5.6	Magnetic stability of lanthanides on graphene/Ir(111)	84
5.7	Magnetic lifetime of lanthanides on graphene/Ir(111)	85
5.8	Sensitivity to contamination of lanthanides on graphene/Ir(111)	86
5.8.1	Exposure time dependence of Nd XAS spectra	86
5.8.2	Exposure time dependence of Ho XAS spectra	88
5.8.3	Exposure time dependence of Er XAS spectra	88
5.8.4	Exposure time dependence of Tb XAS spectra	91
5.9	Sum rules for lanthanide atoms	91

6 Co atoms on hexagonal boron nitride	95
6.1 Co on <i>h</i> -BN	95
6.1.1 Co on <i>h</i> -BN/Ru(0001)	96
6.1.2 Co on <i>h</i> -BN/Ir(111)	100
6.2 Discussion	102
Conclusion and outlook	105
A Crystal field parameters	109
B Tunnel splitting $\Delta_{7,-8}$ for Dy on graphene/Ir(111)	113
Bibliography	124
Acknowledgements	125
Curriculum Vitae	127

List of Figures

1.1	Adatom in C_{3v} and C_{6v} crystal field symmetry	8
1.2	Splitting of J_z levels in a crystal field	9
1.3	Mechanisms of magnetization reversal	10
2.1	Experimental geometry of XMCD and XMLD spectroscopy with representative spectra	19
2.2	End-station of the EPFL/PSI X-treme beamline	20
3.1	Sketch of graphene on Ir(111) surface	26
3.2	Ensemble of disordered Dy atoms	27
3.3	STM image of Dy superlattice	27
3.4	Dy adsorption site with respect to graphene moiré	28
3.5	Autocorrelation function of the STM image of Dy superlattice	29
3.6	Adsorption site of Dy atoms on graphene/Ir(111)	30
3.7	Dy monomers and dimers	31
3.8	XAS and XMCD spectra of Dy atoms on graphene/Ir(111)	33
3.9	Magnetization curves of Dy atoms on graphene/Ir(111)	34
3.10	Evolution of Dy XMCD spectra at $B = -0.1$ T	35
3.11	Grazing magnetization curve of Dy atoms on graphene/Ir(111)	35
3.12	Measurement of magnetic lifetime of Dy atoms on graphene/Ir(111)	37
3.13	Point charge crystal field for Dy on graphene/Ir(111)	38
3.14	Multiplet calculations for Dy on graphene/Ir(111)	40
3.15	The zero field splitting of the Dy lowest multiplet	41
3.16	Zeeman diagram of Dy magnetic levels	43
3.17	Temperature dependence of Dy magnetic lifetime	44
3.18	Coverage dependence of Dy XAS spectra	45
3.19	STM study of Dy coverage dependence.	46
3.20	Coverage dependence of Dy magnetization curve.	47
3.21	Exposure time dependence of Dy XAS spectra.	48
3.22	Calculation of the coverage for Dy samples	50
4.1	X-ray absorption spectra of Dy on Ir(111)	52
4.2	Sample holder with the graphene/Cu foil	54
4.3	X-ray absorption spectra of Dy atoms on graphene/Cu foil	55

List of Figures

4.4	Magnetization curves of Dy atoms on graphene/Cu foil	56
4.5	X-ray absorption spectra of Dy on graphene/Ru(0001)	58
4.6	STM image of Dy atoms on graphene/Ru(0001)	59
4.7	Magnetization curves of Dy atoms on graphene/Ru(0001)	59
4.8	ABA stacking of graphene layers in HOPG	60
4.9	X-ray absorption spectra of Dy on HOPG	62
4.10	Magnetization curve and Zeeman diagram of Dy atoms on HOPG	63
4.11	X-ray absorption spectra of Dy on <i>h</i> -BN/Ir(111)	65
4.12	Magnetization curves of Dy atoms on <i>h</i> -BN/Ir(111)	66
4.13	Point charge crystal field for Dy on <i>h</i> -BN/Ir(111)	67
4.14	Energy diagram of Dy atoms on <i>h</i> -BN/Ir(111)	67
5.1	X-ray absorption spectra of Nd atoms on graphene/Ir(111)	70
5.2	Magnetization curves of Nd atoms on graphene/Ir(111)	71
5.3	Point charge crystal field for Nd atoms on graphene/Ir(111)	72
5.4	Energy diagram of Nd atoms on graphene/Ir(111)	73
5.5	X-ray absorption spectra of Ho atoms on graphene/Ir(111)	74
5.6	Magnetization curves of Ho atoms on graphene/Ir(111)	75
5.7	Point charge crystal field for Ho on graphene/Ir(111)	76
5.8	Energy diagram of Ho atoms on graphene/Ir(111)	76
5.9	X-ray absorption spectra of Er atoms on graphene/Ir(111)	78
5.10	Point charge crystal field for Er on graphene/Ir(111)	79
5.11	Energy diagram of Er atoms on graphene/Ir(111)	79
5.12	X-ray absorption spectra of Er atoms on graphene/Ir(111)	81
5.13	Magnetization curves of Tb atoms on graphene/Ir(111)	82
5.14	Point charge crystal field for Tb on graphene/Ir(111)	82
5.15	Energy diagram of Tb atoms on graphene/Ir(111)	83
5.16	Exposure time dependence of Nd XAS spectra	87
5.17	Exposure time dependence of Ho XAS and XMCD spectra	88
5.18	Exposure time dependence of Er XAS and XMCD spectra	89
5.19	Estimating the share of divalent Er atoms in XAS spectrum	90
5.20	Exposure time and coverage dependence of Tb XAS and XMCD spectra	91
6.1	X-ray absorption spectra of Co atoms on <i>h</i> -BN/Ru(0001)	97
6.2	Point charge crystal field for TM atoms on <i>h</i> -BN	98
6.3	X-ray absorption spectra of Co atoms on <i>h</i> -BN/Ir(111)	101
6.4	Zeeman diagram of Co magnetic levels	103
B.1	Evaluation of tunnel splitting $\Delta_{7,-8}$	114

List of Tables

3.1	Share of divalent and trivalent Dy species in XAS spectra	50
5.1	$4f$ occupation, J , J_z and U_{rev} for lanthanide atoms resulting from multiplet calculations.	85
5.2	Magnetic lifetime of lanthanide atoms on graphene/Ir(111) at 2.5 K	86
5.3	Comparison of angular momenta resulting from sum rules and multiplet calculations	92
6.1	Effective spin and orbital magnetic momenta of Co on h -BN/Ru(0001)	99
6.2	Effective spin and orbital magnetic momenta of Co on h -BN/Ir(111)	102
A.1	Point charge CF scheme for Dy on graphene/Ir(111)	109
A.2	Point charge CF scheme for Dy on h -BN/Ir(111)	110
A.3	Point charge CF scheme for Nd on graphene/Ir(111)	110
A.4	Point charge CF scheme for Ho on graphene/Ir(111)	110
A.5	Point charge CF scheme for Er on graphene/Ir(111)	111
A.6	Point charge CF scheme for Tb on graphene/Ir(111)	111
A.7	Point charge CF scheme for Co on h -BN/Ru(0001)	111
A.8	Point charge CF scheme for Co on h -BN/Ir(111)	112

Introduction

Single magnetic atoms on surfaces are currently the center of a vibrant field of research. The main goal of the investigations is to identify model systems for data storage at ultimate scales, where one atom serves as one unit of information. Aside from this technological appeal, these systems have an even more fundamental allure. Single atoms on surfaces offer a playground for investigating the underlying interactions governing magnetism at the atomic scale. In addition, their assembly in well ordered superlattices would provide an identical environment to each unit and a controlled distance among them, allowing for example to tune their mutual interactions. This would not only facilitate comparison with theory, but would also, from a technological point of view, provide the desired highest possible storage densities of a magnetic medium.

For an atom to be considered as a bit, it must possess an easy magnetization axis and a long lifetime of its magnetization. This can be attained through interaction with the surrounding crystal field, generated either by the supporting surface, or by the surrounding molecular cage. Hence, there are currently two approaches in achieving the magnetic stability and long range order in single atoms. One is by using single-ion molecular magnets [1, 2] and metal-organic networks [3]. Here, a molecular cage protects an atom from contamination. However, the coupling with electrons and vibrational modes of the surrounding ligands destabilizes the atom's magnetic moment. The other approach, and the one that we are following in this thesis, is placing atoms directly on supporting substrates. This reduces the number of bonds and may reduce the atoms' interaction with the environment, resulting in their greater magnetic stability. In addition, it makes the comparison with theory easier.

In a classical picture, the stability of an atom's magnetization is considered to be ruled by the size of the magnetic anisotropy energy barrier (MAE) between the two stable directions of an atom's magnetic moment. The bigger this barrier is, the more resistant the magnetic moment will be against thermally induced magnetization reversal, and consequently, the longer the magnetic lifetime of an atom. The idea that large MAE would necessarily result in long magnetic lifetime initiated the search for the atom/substrate combinations that yield large MAE. Initially, the investigated systems were 3d transition metal (TM) atoms, and large values of MAE were observed [4–7], culminating in the discovery of the record high MAE of 58 meV for Co atoms on MgO [8]. Yet, none of the systems studied yielded desired long magnetic lifetime. As it turned out, strong hybridization of TM atoms with substrates

enables efficient scattering with the substrate's electrons and lowers their spin relaxation times [9]. Throughout the research, it was also established that, in many cases, a classical picture is insufficient for describing the magnetism of surface supported atoms. A quantum mechanical description, in which quantum tunneling of magnetization can cause temperature independent magnetization reversal, is a more appropriate approach.

The hybridization with the electrons of the substrate can be reduced by using $4f$ lanthanide atoms. Their $4f$ orbitals, responsible for their magnetism, are strongly localized and interact mainly electrostatically with the surrounding crystal field generated by the supporting substrate. This approach has proven to be more prosperous and it has, to this day, yielded two systems of single atom magnets. One are Ho atoms on MgO/Ag(100) showing magnetic stability up to 40 K, and a magnetic lifetime of about 1500 s at 10 K [10], and the other are Dy atoms on graphene/Ir(111) showing a magnetic lifetime of about 1000 s at 2.5 K, as will be shown in this thesis. Achieving the magnetic stability in these two systems has emphasized the role of the decoupling layers in stabilizing atom's magnetization. Namely, the same lanthanide atoms, when placed directly on a bare metal surface, do not show neither hysteresis nor magnetic remanence [11, 12]. This indicates that, despite their high localization, $4f$ orbitals necessarily need to be protected from electron and phonon scattering. Furthermore, the achieved stability has underlined the crystal field symmetry as one of the key factors in determining the magnetic properties and stability of adsorbed atoms.

The objective of this thesis is twofold. First, by studying the magnetic properties of $4f$ lanthanide and $3d$ transition atoms on primarily decoupling layers, we aim to investigate the underlying interactions and conditions that lead to the magnetic stability in single atoms. In particular, we focus on atoms in two types of crystal field symmetries, namely C_{3v} and C_{6v} crystal field symmetry, provided by the h -BN and graphene surface, respectively. As a second objective, we investigate the possibility to use the moiré pattern of the graphene/Ir(111) surface as a template for a self-assembly of single atom magnets. The following paragraphs summarize the structure of this thesis.

Chapter 1 reviews the fundamentals of atomic magnetism. First, we address the origin of magnetism in free atoms, after which we focus on atoms in the crystal field environment of a supporting substrate. In particular, we discuss the influence of two different crystal field symmetries, namely C_{3v} and C_{6v} symmetry, on the magnetic levels of an atom. Further, we analyze two magnetization reversal mechanisms arising for an atom in a crystal field: quantum tunneling of magnetization and scattering with electrons and phonons of a substrate, with respect to these two crystal field symmetries. Finally, we address the influence of a magnetic field on the magnetic levels of an atom.

Chapter 2 introduces the main methods employed in investigating the magnetic properties of surface supported atoms. Fundamental principles of x-ray absorption spectroscopy, x-ray magnetic circular and linear dichroism are given. Further, we introduce multiplet calculations, a method for simulating experimental spectra and calculating energy level diagrams of

investigated systems. In addition, this Chapter also presents sample preparation techniques as well as the experimental setup.

Chapter 3 presents our combined STM, XMCD and multiplet calculations study of Dy atoms on graphene/Ir(111). In the first part of this Chapter, we investigate the moiré pattern of graphene/Ir(111) as a template for the self-assembly of Dy atoms. We determine the conditions for the growth of the superlattice of Dy atoms. Further, we determine the adsorption site of Dy atoms with respect to the moiré pattern and graphene lattice. The remainder of the chapter is devoted to the study of magnetic properties of Dy atoms. We present XMCD measurements of Dy atoms in both ordered and disordered ensembles, and show that in both cases Dy atoms show long magnetic lifetime at $T = 2.5$ K. To elucidate the origin of their remarkable magnetic stability, we investigate the crystal field environment provided by graphene and the resulting electronic configuration and magnetic level diagram of Dy atoms. Further, we investigate the magnetization reversal mechanisms arising from the scattering with electrons and phonons, as well as graphene's ability to decouple Dy atoms from these scattering events. Finally, we investigate the influence of temperature on the magnetic stability of Dy atoms, as well as the impact of the employed x-ray flux on the measured lifetime.

Chapter 4 extends the study of the magnetic and electronic properties of surface supported Dy atoms with five additional substrates. First, to further clarify graphene's capacity as a decoupling layer, we investigate Dy atoms on a bare Ir(111) surface. Second, to investigate the influence of the graphene/substrate hybridization on the properties of adsorbed Dy atoms, we extend our study with HOPG and two other graphene/metal substrates, namely graphene/Cu and graphene/Ru(0001). Similar to graphene on Ir(111), graphene forms only a weak bond with Cu, whereas it strongly hybridizes with Ru(0001) surface. HOPG represents another weakly bound system, as it consists of weakly bound parallel graphene layers. Finally, to compare graphene's decoupling potential to one of an insulator, we investigate Dy electronic and magnetic properties on *h*-BN/Ir(111). This further enables the investigation of the importance of the crystal field symmetry in comparison with the decoupling in stabilizing the atom's magnetization. *h*-BN offers superior electronic decoupling from the metal substrate; however, it provides a lower crystal field symmetry in comparison with graphene. Dy atoms on graphene are subjected to the C_{6v} , whereas on *h*-BN they are subjected to the C_{3v} crystal field symmetry.

Chapter 5 addresses the magnetic and electronic properties of Nd, Ho, Er and Tb atoms on graphene/Ir(111). For each atom, we determine the crystal field environment provided by the graphene/Ir(111) substrate and investigate its influence on the electronic configuration and the magnetic level structure of adsorbed lanthanide atoms. We evaluate the magnetic stability of these atoms based on their ground state and energy level diagram and determine the main mechanism for magnetization reversal in each case. Further, we examine the underlying interactions ruling their electronic configuration on this surface. In addition, this Chapter addresses the sensitivity of lanthanide atoms to contamination and the validity of the sum rule analysis of their XAS and XMCD spectra, whose results we compare to those obtained from multiplet calculations.

Introduction

Chapter 6 addresses the magnetic properties of Co atoms on an *h*-BN surface. We investigate whether it is possible to achieve magnetic stability in this transition metal atom by placing it on a wide band-gap insulator like *h*-BN. Further, by using two different *h*-BN/metal substrates, we study the effect of the substrate hybridization on its magnetic levels and stability. Namely, we use strongly interacting *h*-BN/Ru(0001) and weakly interacting *h*-BN/Ir(111) systems.

Finally, at the end of this thesis, the main results are summarized and outlook on the future work is given.

1 Magnetism of surface adsorbed atoms

This chapter introduces the concepts for describing the magnetism of adatoms on surfaces. Section 1.1 gives an overview of the origin of magnetism in free atoms. The influence of the crystal field environment on the magnetism and magnetic levels of adatoms is discussed in Section 1.2. In addition, a detailed analysis for two particular cases, C_{3v} and C_{6v} crystal field symmetries, is given. Finally, Section 1.3 describes the evolution of the magnetic levels of an atom in an external magnetic field.

1.1 Origin of magnetism in free atoms

The magnetism of atoms originates from electrons in their partially filled electronic orbitals. For both transition metal and lanthanide atoms, the two categories of atoms studied throughout this thesis, the Coulomb interaction between electrons is stronger than the spin-orbit interaction between their individual angular momenta. The electron-electron interaction is typically of the order of 1 eV, whereas spin-orbit interaction is of the order of 0.1 eV for 4f lanthanide and $10 - 10^2$ meV for 3d transition metal atoms [13, 14]. In this case, the interaction between spin and orbital angular momenta can be described by LS or Russell–Saunders coupling [15]. In this coupling scheme, the Coulomb interaction couples individual orbital momenta into the total orbital momentum \mathbf{L} , and exchange interaction couples the individual spin and orbital angular momenta into the total spin momentum. Finally, the spin-orbit interaction couples the resulting \mathbf{L} and \mathbf{S} into the total angular momentum of an atom, \mathbf{J} .

The quantum numbers of total angular momentum \mathbf{J} assume the following values: $|L - S| \leq J \leq L + S$. Further, each J consists of $(2J + 1)$ J_z energy levels which are degenerate in the case of free atoms, and their degeneracy can be lifted by imposing an anisotropy to an atom. The ground state J multiplet can be determined by the three Hund's rules [16, 17]. These rules determine the filling of the electronic orbitals that minimizes the Coulomb interaction between the electrons. The filling of the orbitals is further restricted by Pauli exclusion principle, from which follows that two electrons in the same orbital must have their spins anti-aligned. According to the first two Hund's rules, the ground state configuration is the one with the maximal S and L

Chapter 1. Magnetism of surface adsorbed atoms

values. The third Hund's rule determines the J value for which the energy due to the spin-orbit interaction,

$$H_{SOC} = -\zeta \mathbf{L} \cdot \mathbf{S}, \quad (1.1)$$

is the lowest; ζ is the constant of the spin-orbit coupling. In the case of more than half-filled orbitals, the spin and orbital angular momentum are parallel to each other and the ground state is $J = L + S$. Less than half-filled orbitals have their angular momenta anti-parallel and their ground state is given by $J = |L - S|$. Finally, half-filled shells have $L = 0$ and $J = S$.

The total magnetic moment of an atom is given by

$$\mathbf{m} = -\mu_B (g_L \mathbf{L} + g_S \mathbf{S}) = -\mu_B g_J \mathbf{J}, \quad (1.2)$$

where μ_B is the Bohr magneton, $\mu_B = 5.79 \times 10^{-5} \text{ eV/T}$, g_L , g_S and g_J are g -factors of electron orbital, spin, and total angular momentum, respectively. The g_J - or Landé factor of the total angular momentum is given by:

$$g_J = \frac{3}{2} + \frac{S(S+1) - L(L+1)}{2J(J+1)}, \quad (1.3)$$

while the other two g -factors are $g_L = 1$ and $g_S \approx 2$ [18]. In a free atom, the magnetic moment does not have a preferential axis and its orientation fluctuates in space. This results in zero net magnetization of a free atom. Placing an atom in a crystal field or applying a magnetic field creates an anisotropy that stabilizes the magnetic moment in a preferential orientation.

1.2 Atom in a crystal field

Surface adsorbed atoms feel the electrostatic potential of the surrounding charges generated by the electrons and ions of a surface. This potential is called crystal or ligand field, and it interacts primarily with the orbital angular momentum of the adsorbed atom. The interaction with the spin is indirect, and it occurs via the spin-orbit coupling.

The magnetism of lanthanide atoms originates from electrons in their well shielded $4f$ orbitals. In this case, the spin-orbit interaction between electrons is much larger than their interaction with the crystal field, with the latter being of the order of 10 meV [14]. Hence, the crystal field interaction can be viewed as a perturbation to the overall energy of an atom and J remains a good quantum number for describing the system. The crystal field lifts the degeneracy of the lowest J multiplet and imposes its symmetry to J_z states. In the case of the pure uniaxial anisotropy, J_z states are simply displaced in energy and J_z remains a good quantum number. In the case where additional transverse crystal field parameters are present, several J_z states are mixed into new eigenstates and J_z is no longer a good quantum number. This will be addressed in detail for two specific crystal field symmetries further on in this chapter.

The magnetism of transition metals originates from their outer $3d$ electrons that strongly interact with the electrons of the surface. Here, the interaction with the crystal field is of the order of 1 eV [13] and it is much stronger than the spin-orbit interaction. Here, the spin-orbit interaction may be viewed as a perturbation, and, consequently, J is no longer a good quantum number.

The interaction with a crystal field can greatly reduce or even completely quench the orbital momentum of transition metal atoms on surfaces. In this respect, there are two distinct cases. In systems where crystal field completely quenches the orbital angular momentum, its value can be partially restored through the spin-orbit interaction. This is the so-called second-order orbital momentum and is observed, for example, in Fe atoms on MgO [19]. Due to orbital momentum being partially restored, the spin-orbit coupling can further split the lowest multiplet whose multiplicity is given by the spin angular momentum. To interpret the response of an atom subjected to a magnetic field, one can consider an equivalent magnetic moment in a classical magnetic anisotropy barrier. In this case, the total magnetic moment is given by the sum of spin and orbital moment of the ground state of an atom, whereas the height of the barrier is given by the total energy splitting of the lowest multiplet.

Systems where crystal field does not quench the orbital momentum, *i.e.*, systems with first-order orbital momenta, have to be treated with a complete quantum mechanical approach. This is, for example, the case for Co atoms on MgO [8]. Here, both spin and orbital angular momentum contribute to the multiplicity of the ground state multiplet, with the latter being determined by solving the effective spin Hamiltonian. In this case, the crystal field imposes its symmetry to the magnetic levels of an atom, as discussed further in this chapter.

1.2.1 Crystal field Hamiltonian

In spherical tensor notation, the crystal field Hamiltonian can be expressed in terms of the Stevens operators \hat{O}_m^n and coefficients B_m^n [18, 20]:

$$H_{CF} = \sum_{n,m} B_m^n \hat{O}_m^n. \quad (1.4)$$

Stevens coefficients are real numbers, whereas Stevens operators are functions of spherical tensor operators \hat{J}_z , \hat{J}_+ and \hat{J}_- , with the latter two being the ladder operators within the J multiplet. Due to the orthogonality of the spherical harmonics and time reversal symmetry, only even values of m are allowed. Real values of operators are obtained for $m = 2, 4, \dots, 2J$ and $n \leq m$ [21]. In addition, values of n are further limited by the crystal field symmetry, $C_{\chi\nu}$, and can only take values $n = k\chi$, where k is an integer, $k = 0, 1, \dots$ [22].

The symmetry of the crystal field is determined by the packing of the atoms of the surface and the adsorption site of an adatom on it. Throughout this thesis, atoms on three substrates are studied. These substrates generate crystal fields with two different symmetries, C_{3v} and C_{6v} , which are depicted in Figure 1.1. In the following, relevant Stevens operators and their

influence on the magnetic states J_z will be discussed.

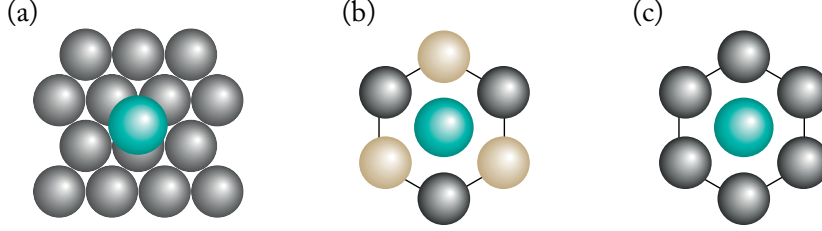


Figure 1.1 – Adatom adsorbed on the three-fold symmetric adsorption site of (a) (111) surface, e.g. Ir(111), and (b) hexagonal ring composed of two different atomic species (e.g. hexagonal boron nitride). (c) Adsorption of an adatom on the six-fold symmetric adsorption site of hexagonal ring composed of single atomic species, e.g. graphene.

1.2.2 Magnetic levels in C_{3v} and C_{6v} crystal field symmetry

The expansion of the crystal field Hamiltonian given by Equation 1.4 in C_{3v} and C_{6v} symmetry can have many terms; however, only the ones of the lowest order will have a considerable effect on the magnetic levels of an atom. In C_{3v} symmetry, the Hamiltonian with relevant Stevens operators is reduced to [23]

$$H_{3v} = B_2^0 \hat{O}_2^0 + B_4^0 \hat{O}_4^0 + B_4^3 \hat{O}_4^3 + B_6^0 \hat{O}_6^0 + B_6^3 \hat{O}_6^3 + B_6^6 \hat{O}_6^6, \quad (1.5)$$

whereas the one in C_{6v} symmetry is given by:

$$H_{6v} = B_2^0 \hat{O}_2^0 + B_4^0 \hat{O}_4^0 + B_6^0 \hat{O}_6^0 + B_6^6 \hat{O}_6^6. \quad (1.6)$$

The Stevens operators in Equations 1.5 and 1.6 expressed in terms of angular momentum operators [18], with the abbreviation $X = J(J+1)$, are:

$$\begin{aligned} \hat{O}_2^0 &= 3\hat{J}_z^2 - X, \\ \hat{O}_4^0 &= 35\hat{J}_z^4 - (30X - 25)\hat{J}_z^2 + 3X^2 - 6X, \\ \hat{O}_6^0 &= 231\hat{J}_z^6 - (315X - 735)\hat{J}_z^4 + (105X^2 - 525X + 294)\hat{J}_z^2 - 5X^3 + 40X^2 - 60X, \\ \hat{O}_4^3 &= \frac{1}{4}(\hat{J}_+^3 - \hat{J}_-^3)\hat{J}_z + \hat{J}_z(\hat{J}_+^3 - \hat{J}_-^3), \\ \hat{O}_6^3 &= \frac{1}{4}[(\hat{J}_+^3 + \hat{J}_-^3)(11\hat{J}_z^3 - (3X + 59)\hat{J}_z) + (11\hat{J}_z^3 - (3X + 59)\hat{J}_z)(\hat{J}_+^3 + \hat{J}_-^3)], \\ \hat{O}_6^6 &= \frac{1}{2}(\hat{J}_+^6 - \hat{J}_-^6). \end{aligned}$$

The first three listed operators, \hat{O}_2^0 , \hat{O}_4^0 and \hat{O}_6^0 , are the uniaxial crystal field operators. They partially lift the degeneracy of J_z states, that is, J_z levels with different absolute value get split

in energy, while those with the same absolute value remain degenerate. The uniaxial operators determine the total zero field splitting, *i.e.*, the energy difference between the lowest and the highest lying J_z state. In analogy with classical systems, this value is commonly related to the magnetic anisotropy energy.

The lowest order uniaxial crystal field consists of only the first term in the expansion of the Hamiltonian in Equations 1.5 and 1.6, $B_2^0 \hat{O}_2^0$. In this case, the factor $J(J+1)$ of Stevens operator \hat{O}_2^0 equally shifts in energy all the magnetic levels, and the second order operator \hat{J}_z^2 displaces them in a shape of parabola. The sign of B_2^0 coefficient determines the orientation of this parabola, and hence the resulting anisotropy of the system. For negative coefficients, the parabola is pointing downwards and the system has an out-of-plane anisotropy with a maximal J_z ground state doublet (Figure 1.2(a)). For positive coefficients, the parabola is pointing upwards, and the system has an in-plane anisotropy with a minimal J_z ground state (Figure 1.2(b)). Introducing higher order operators like \hat{J}_z^4 and \hat{J}_z^6 results in non-monotonic distribution of J_z levels. This can even lead to an intermediate J_z doublet as a ground state.

The last three operators, \hat{O}_4^3 , \hat{O}_6^3 and \hat{O}_6^6 , are the transverse crystal field operators. They mix J_z states differing by $\Delta J_z = \pm 3$ and $\Delta J_z = \pm 6$, resulting in eigenstates that are a mixture of several J_z states. These operators introduce quantum tunneling of magnetization (QTM) to a system [24], and can open new relaxation paths by spin scattering with electrons and phonons of a substrate. The mixing of the states in C_{3v} crystal field symmetry is depicted in Figure 1.2(c).

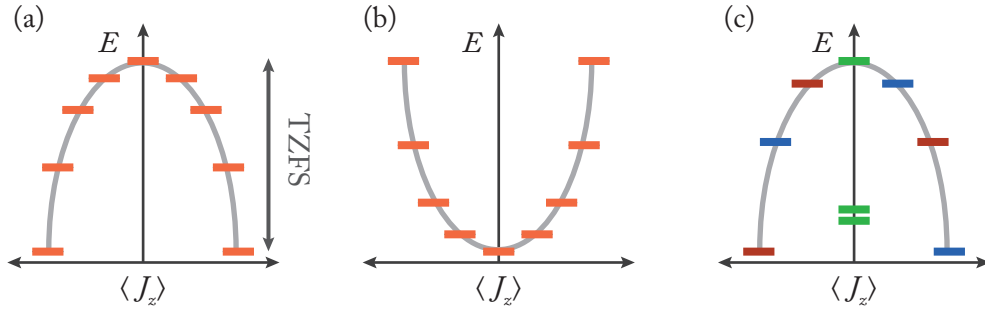


Figure 1.2 – (a,b) Schematic representation of magnetic levels in $H_{CF} = B_2^0 \hat{O}_2^0$ for an atom with $J = 4$; (a) $B_2^0 < 0$ results in an out-of-plane anisotropy, and (b) $B_2^0 > 0$ in an in-plane anisotropy. An arrow in (a) marks the height of the total zero field splitting (TZFS). (c) Mixing of J_z levels in C_{3v} crystal field symmetry. Different colors represent three classes of eigenstates created by the three-fold symmetry. The eigenstate marked in green consists of $J_z = 0$ state on top of the barrier, and a tunnel-split doublet with quenched $\langle J_z \rangle$ at a lower energy.

In the absence of transverse crystal field operators, the system has to go over the entire barrier to reverse the direction of its magnetization. The presence of transverse operators, and in particular quantum tunneling of magnetization, can greatly reduce this barrier and facilitate magnetization reversal. These processes are depicted in Figure 1.3. In the following, we discuss the influence of the transverse crystal field parameters on the magnetic stability of atoms. In

particular, we examine the magnetic stability of lanthanide atoms in C_{3v} and C_{6v} crystal field symmetry.

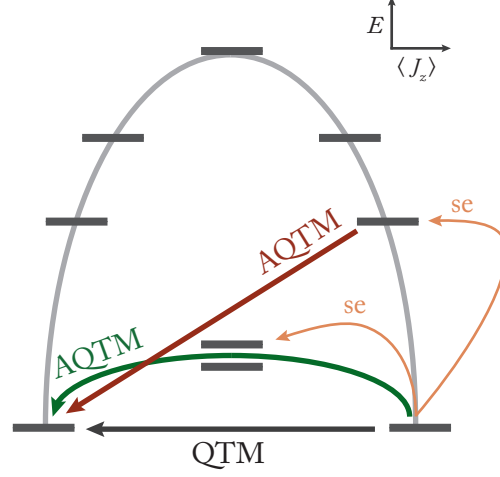


Figure 1.3 – Schematic representation of different mechanisms of magnetization reversal in the presence of transverse crystal field operators; quantum tunneling of magnetization (QTM) between two ground states and assisted QTM (AOTM) via spin excitations (se) to higher energy levels.

1.2.3 Quantum tunneling of magnetization in lanthanide atoms

The quantum tunneling of magnetization is the direct consequence of the coupling between different J_z states which are nearly matching in energy [25]. The coupling between two J_z states in C_{3v} crystal field symmetry can be expressed in the following way:

$$\langle J_z = n | \hat{O}_4^3 | J_z = m \rangle \neq 0, \quad |n - m| = 3, 6, 9, 12, 15. \quad (1.7)$$

Note that the maximal difference between coupled levels $|n - m|$ depends on the total number of available J_z states in a particular atom. In Equation 1.7, values are given for $J = 8$ multiplet and its 17 J_z states; lower J multiplets will have less available $|n - m|$ values. The C_{6v} crystal field symmetry couples fewer levels into a single eigenstate:

$$\langle J_z = n | \hat{O}_6^6 | J_z = m \rangle \neq 0, \quad |n - m| = 6, 12. \quad (1.8)$$

In the case of integer J systems all states except $J_z = \pm 3, \pm 6$ are protected against QTM at $B = 0$ T in both crystal field symmetries. At $B = 0$ T, the $J_z = \pm 3, \pm 6$ states form tunnel-split doublets with quenched $\langle J_z \rangle$. If one of these doublets is a ground state, QTM occurs and there is no stable magnetization. Alternatively, these states provide a shortcut that greatly reduces the energy barrier for magnetization reversal.

In half-integer J systems, all possible ground states are protected against QTM. Even if they

are coupled with the transverse term, the magnetic states of half-integer J systems are always degenerate in absence of external magnetic field. This is due to the time reversal symmetry (TRS), as expressed by Kramers theorem, and no QTM can occur [26].

Both non-Kramers doublets of non-integer J systems and Kramers doublets of integer J systems can be classified into two categories: perfectly axial and non-axial doublets [27]. Non-axial doublets include those allowing QTM identified by Equations 1.7 and 1.8, as well as Kramers doublets that tunnel split in the presence of the transverse perturbations, originating from the transverse magnetic field. These non-axial doublets facilitate magnetization reversal, as is discussed in the next Section.

1.2.4 Scattering with electrons and phonons in lanthanide atoms

Scattering with electrons and phonons of the substrate can cause additional magnetization relaxation mechanisms. In the absence of magnetic field, the scattering can facilitate the magnetization reversal via excitation to higher energy levels, whereas in finite fields, it can produce a direct transition between the two states of the lowest J_z doublet.

The scattering probability is governed by the product of the density of states of scattering particles (phonons or electrons) and the transition matrix element of a particular transition. At $B = 0$ T, due to the degeneracy of the ground states, no direct transition between them can occur as the density of states of interacting particles vanishes when the energy needed to be exchanged is zero. At finite magnetic fields, the probability of direct transition strongly depends on the matrix element, which is directly related to whether or not the TRS needs to be broken for that transition to occur. The transitions which are TRS allowed will occur at the higher rate than those which are TRS forbidden at $B = 0$ T [26].

In general, scattering with electrons can produce transitions between levels differing by

$$\Delta J_z = 0, \pm 1, \quad (1.9)$$

as it is given by the magnetic dipole selection rules. For scattering with phonons, in addition to transitions given by Equation 1.9, the transitions between levels differing by $\Delta J_z = \pm 2$ can occur [28]. However, due to their weak effect, they will not be considered in the further discussion.

The coupling of J_z levels in C_{3v} and C_{6v} crystal field symmetry expressed by Equations 1.7 and 1.8, respectively, allows additional transitions for phonon and electron scattering, with respect to those expressed with Equation 1.9. In particular, in C_{3v} symmetry Equation 1.9 can be extended to:

$$\Delta J_z = 0 \pm 3k, -1 \pm 3k, 1 \pm 3k \quad (1.10)$$

whereas in C_{6v} symmetry it takes the following form:

$$\Delta J_z = 0 \pm 6k, -1 \pm 6k, 1 \pm 6k, \quad (1.11)$$

where k assumes positive integer values that reflect the coupling between different J_z states expressed with Equations 1.7 and 1.8. Explicitly, from Equation 1.11, it follows that in C_{6v} symmetry a direct transition can occur between levels differing by $\Delta J_z = 0, 6, 12, \pm 1, \pm 7, \pm 13, \pm 5, \pm 11$. Hence, at $B = 0$ T, for integer J systems, all possible ground states apart from $J_z = \pm 3$ and $J_z = \pm 6$ are protected against direct transitions, as they cannot be connected with the listed ΔJ_z values. As mentioned before, $J_z = \pm 3$ and $J_z = \pm 6$ are tunnel-split doublets that support QTM. In the case of half-integer J systems, the direct transition between two ground states with a single electron scattering can occur in all cases apart from $J_z = \pm 3/2, \pm 9/2, \pm 15/2$ at $B \neq 0$ T. The transition between these states would require multiple electron scattering events. From similar considerations for integer and non-integer J systems in the C_{3v} and $B \neq 0$ T, it follows that none of their ground state doublets is protected against direct transition with a single scattering event, as already $\Delta J_z = \pm 1$ can connect any two ground states in this case.

Relaxation paths at $B = 0$ T are provided by thermally activated QTM. By absorbing energy from electrons or phonons of the substrate, a system can be excited to a level for which QTM is allowed. This will result in a magnetization reversal. In the case of integer J , this happens for excitation to tunnel split doublets with $J_z = \pm 3$ and $J_z = \pm 6$. For atoms with half-integer J , assisted QTM can occur through levels that are, due to the transverse perturbations, non-axial. In case of C_{6v} and C_{3v} symmetry, these are all states that are not mixed with $J_z = \pm 3/2$ states [27].

1.3 Atom in a magnetic field

The interaction between the magnetic moment of an atom and the uniaxial magnetic field can be described with the following Zeeman Hamiltonian:

$$H_Z = -\mu_B g_J \mathbf{J} \cdot \mathbf{B} = -\mu_B g_J J_z B_z. \quad (1.12)$$

This interaction shifts the energy levels with positive J_z values to a higher energy, whereas the ones with negative J_z get lowered in energy. As a consequence, magnetic field lifts the remaining double degeneracy of J_z states and splits the tunnel-split doublets of integer J systems.

As was noted in the previous section, the presence of the magnetic field breaks the time reversal symmetry and enables the magnetization reversal by scattering with electrons and phonons which was otherwise, due to these symmetry considerations, prohibited. Magnetic field can even provide an additional magnetization reversal path. For certain crystal field splittings of J_z levels, it is possible to match two different J_z levels in energy by applying a particular value of magnetic field. At this point, these two J_z levels are quasi-degenerate and

mixed by the transverse magnetic anisotropy [29]. This enables QTM and, as a consequence, the reversal of magnetization.

2 Methods

This chapter introduces the main methods employed in the study of magnetic properties of surface adsorbed atoms. In Sections 2.1 and 2.2, the main theoretical principles of XAS, XMCD and XMLD spectroscopy are given. Section 2.3 presents the main experimental aspects of these techniques, including the experimental setup and the sample preparation. Multiplet calculations are presented in Section 2.4, and Section 2.5 briefly presents the details of the STM characterization.

2.1 XAS and XMCD spectroscopy

Investigating the electronic and magnetic properties of individual atoms on surfaces requires an appropriate experimental probe. X-ray magnetic circular dichroism (XMCD), along with X-ray absorption spectroscopy (XAS), is an unparalleled tool to study their properties as it allows investigating the properties of systems in the sub-monolayer regime. In particular, it can be used to probe the magnetic properties of systems with coverages down to $\Theta = 0.002$ ML [30]. This technique, developed in the late 1980 and early 1990s [31–40], apart from its extremely high sensitivity, offers the possibility of probing separately the magnetic properties of multiple elements on the same surface. The theoretical aspects of XMCD are well established and their details can be found for example in [13, 41]. In the following, only the main theoretical concepts of this method are presented.

2.1.1 Transition probability

X-ray magnetic circular dichroism is based on the polarization dependent photon absorption in magnetic materials. It corresponds to the difference in x-ray absorption for two different helicities of circularly polarized x-rays.

In an atom, an incoming photon of energy $E = \hbar\omega$ can induce a transition of a core electron into an empty valence state if the energy difference between these two states matches the energy of a photon. For a single electron process, the transition probability per unit time from

Chapter 2. Methods

an initial state $|i\rangle$ to a final state $|f\rangle$ is given by the Fermi's Golden rule [13, 42]:

$$W_{fi} = \frac{2\pi}{\hbar} \sum_f |\langle f | H_{\text{int}} | i \rangle|^2 \delta_{E_f - E_i - \hbar\omega}, \quad (2.1)$$

where H_{int} is the Hamiltonian describing the interaction between an electron and a photon, E_i and E_f are the energies of an initial and a final state of the system, respectively, and the delta function ensures the energy conservation of the system. The interaction Hamiltonian expressed in terms of the photon vector potential \mathbf{A} and electron momentum operator \mathbf{p} is [13]

$$H_{\text{int}} = \frac{e}{m_e} \mathbf{p} \cdot \mathbf{A}, \quad (2.2)$$

where, for an incident electromagnetic wave, the vector potential is given by $\mathbf{A} = A_0 \hat{\mathbf{e}} e^{i\mathbf{k} \cdot \mathbf{r}}$, with A_0 being the amplitude of the vector potential and $\hat{\mathbf{e}}$ the unit vector of the photon polarization. Given the relation between \mathbf{A} and electric field \mathbf{E} in free space, $\mathbf{E} = -\frac{\partial \mathbf{A}}{\partial t}$, it is clear that the transitions are induced by the electric field of the incoming electromagnetic wave.

In the electric dipole approximation, which is valid for the small absorbing atomic shell in comparison with the x-ray wavelength, $\mathbf{k} \cdot \mathbf{r} \ll 1$ [13], we can use the approximation $e^{i\mathbf{k} \cdot \mathbf{r}} \simeq 1 + i\mathbf{k} \cdot \mathbf{r}$. In addition, using the commutation law, $\mathbf{p} = \frac{m_e}{i\hbar} [\mathbf{r}, H]$, the transition matrix element of Equation 2.1 becomes

$$M_{if} = \langle f | H_{\text{int}} | i \rangle \propto \langle f | \mathbf{p} \cdot \hat{\mathbf{e}} | i \rangle \propto \langle f | \mathbf{r} \cdot \hat{\mathbf{e}} | i \rangle, \quad (2.3)$$

giving the transition probability per unit time in the electric dipole approximation [43]

$$W_{fi} = \frac{2\pi e^2 A_0^2}{m_e^2 \hbar} \sum_f |\langle f | \mathbf{r} \cdot \hat{\mathbf{e}} | i \rangle|^2 \delta_{E_f - E_i - \hbar\omega}. \quad (2.4)$$

The dipole operator $\mathbf{r} \cdot \hat{\mathbf{e}}$ expressed in terms of spherical harmonics $Y_{l,m}(\theta, \phi)$ for three different polarizations of light propagating in $\hat{\mathbf{z}}$ direction [13] is:

$$\begin{aligned} -\frac{1}{\sqrt{2}}(x + iy) &= r \sqrt{\frac{4\pi}{3}} Y_{1,1}, \\ \frac{1}{\sqrt{2}}(x - iy) &= r \sqrt{\frac{4\pi}{3}} Y_{1,-1}, \\ z &= r \sqrt{\frac{4\pi}{3}} Y_{1,0}, \end{aligned} \quad (2.5)$$

for right circular, left circular and linear polarization, respectively.

2.1.2 Dipole selection rules

The transition matrix element M_{if} can be calculated only when the initial and final states are known. Nevertheless, its angular part can be written in terms of the Wigner $3j$ symbols [44] which imposes the so-called dipole selection rules to it. For states that can be described with (L, L_z, S) quantum numbers, the dipole selection rules state that the transitions are possible only between initial and final states differing by $\Delta L = \pm 1$ and $\Delta L_z = 0, \pm 1$. As the interaction with photon only affects the orbital angular momentum of an electron, the spin angular momentum remains unchanged, $\Delta S = 0$ [13, 44].

The states originating from spin-orbit split levels are described with (J, J_z) quantum numbers. In this case, as a consequence of the spin-orbit coupling between L and S into J , the angular momentum of a photon will be partially transmitted to the spin angular momentum of an electron. The dipole selection rules state that transitions are possible between states differing by $\Delta J = 0, \pm 1$ and $\Delta J_z = 0, \pm 1$ [44].

The detailed treatment of transitions in the case of spin-orbit split levels can be found for example in [45]. However, the basic principles behind the XMCD originating from spin-orbit split levels can be described using a simplified two step model [13, 46] summarized in the following. In the first step, the photons transfer their angular momentum to core electrons, which creates spin-polarized photoelectrons. The polarization of their spins depends on both the helicity of the incoming photon, as well as on the sign of the spin-orbit coupling of level from which they originate. For example, at the L_2 edge for which $J = L - S$, x-rays with helicity $q = +1$ excite 25% of spin up and 75% of spin down electrons, whereas at the L_3 with $J = L + S$, they excite 62.5% of spin up, and 37.5% of spin down electrons. Opposite percentages are valid for x-rays with helicity $q = -1$. Here, spin directions are defined with respect to the direction of x-rays. In the second step, these photoelectrons are excited into the valence band, where photoelectrons with spin up occupy empty spin up states and photoelectrons with spin down occupy empty spin down states. In case there is an equal number of empty spin up and spin down states available, this results in equal absorption of the left and right circularly polarized photons and gives no dichroic signal. However, in case of an imbalance in spin up and spin down empty states, *i.e.*, in case that the investigated system has a net magnetic moment, there will be an imbalance in absorption of the left and right circularly polarized photons, resulting in an XMCD signal.

2.2 XMLD spectroscopy

In addition to XMCD, we used x-ray magnetic linear dichroism (XMLD) to characterize the properties of surface adsorbed atoms. Similar to XMCD spectroscopy, this method is based on the polarization dependent photon absorption in magnetic materials. However, in this case, linearly polarized x-rays are used.

In atoms with finite magnetic moments, the spin-orbit interaction distorts their spherical

charge distribution, resulting in a uniaxial charge distribution along their spin axis [13]. When probing these atoms with two types of linearly polarized x-rays, namely x-rays with their electric field vector \mathbf{E} being parallel and perpendicular to the sample magnetization, a dichroic signal will arise. The observed dichroism is a consequence of the different number of valence holes for the two directions of the atomic volume [13]. Further details on XMLD spectroscopy can be found in [13, 47].

2.3 Experimental aspects

2.3.1 Spectral analysis

For an ensemble of atoms exposed to x-rays, an abrupt increase in the adsorption occurs when the energy of the incoming x-rays corresponds to the binding energy of a core level of these atoms. This is the so-called absorption edge. The soft x-ray range, corresponding to energies between 0.2 and 2 keV, includes the absorption edges of $3d$ transition metals and $4f$ lanthanides relevant for the study of their magnetism. These are the $L_{2,3}$ edges in transition metals, where of interest are the transitions from spin-orbit split $2p_{1/2,3/2}$ levels to empty states of $3d$ orbitals. In lanthanides, these are the $M_{4,5}$ edges, where of interest are the transitions from spin-orbit split $3d_{3/2,5/2}$ to empty states of $4f$ orbitals. The acquired polarization dependent XAS spectra are the fingerprint of the electronic and magnetic ground state of the investigated system.

Figure 2.1(a) shows the XAS spectra acquired with left and right circularly polarized x-rays, together with the sketch of the experimental geometry, at Dy $M_{4,5}$ edges for these atoms on graphene/Ir(111)¹. The sum of these spectra corresponds to the total XAS spectrum and their difference to the XMCD spectrum. Throughout this thesis, only the sum and the difference, and not the individual components, will be given. Figure 2.1(b) shows the absorption spectra at Dy $M_{4,5}$ edges acquired with two different linear polarizations of x-rays, namely one with its electric field vector oscillating in plane of the sample, and the other with its electric field vector oscillating in the direction normal to the surface of the sample. Throughout this thesis, only their difference, corresponding to XMLD, will be given.

Expectation values of the orbital $\langle L_z \rangle$ and the effective spin magnetic $\langle S_{\text{eff}} \rangle$ moment of the investigated system can be obtained by applying the so-called sum rules to the integrated XAS and XMCD spectra [37, 48]. Here, $\langle S_{\text{eff}} \rangle$ contains both the contribution from spin magnetic moment $\langle S_z \rangle$ and spin dipole magnetic moment $\langle T_z \rangle$, as with sum rules it is not possible to determine their contributions independently. The spin dipole magnetic moment originates from the distortion of the spherical atomic cloud, either due to the spin-orbit coupling or the crystal field effects [48]. Note that the values here have subscript z , as they refer to the values projected onto the investigated direction of the x-rays (and applied magnetic field). By labeling the integral of the total XAS area with t , integral over the total XMCD area with q , and

¹The spectra are presented here for illustrative purposes only and their detailed analysis is given in Chapter 3.

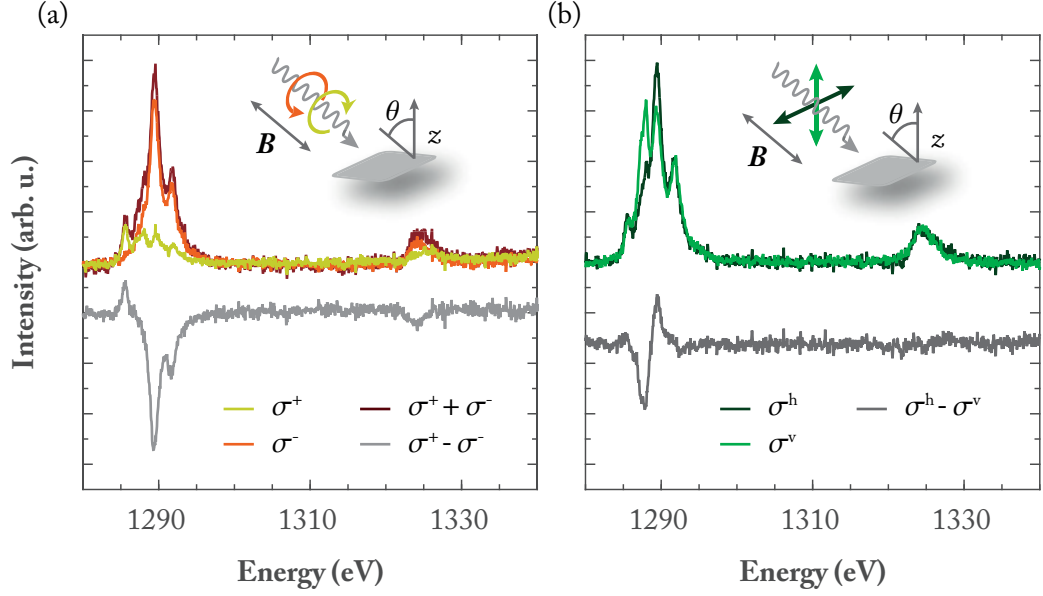


Figure 2.1 – Example of spectra acquired with circularly (a) and linearly (b) polarized x-rays, together with their experimental geometries. The presented spectra were acquired for Dy atoms on graphene/Ir(111). (a) Circular spectra were acquired with two types of circularly polarized x-rays, σ^+ and σ^- . Their sum ($\sigma^+ + \sigma^-$) corresponds to the total XAS, whereas their difference ($\sigma^+ - \sigma^-$) corresponds to the XMCD spectrum. (b) Linear spectra were acquired with two different linearly polarized x-rays, σ^h and σ^v . Their difference ($\sigma^h - \sigma^v$) corresponds to the XLD spectrum. In all experiments, the applied magnetic field \mathbf{B} was collinear with the direction of x-rays and they were employed at the angle θ with respect to the surface normal.

integral over the L_3 or M_5 edge with p , for transition metals the sum rules are

$$\langle L_z \rangle = -\frac{4}{3} n_h \frac{q}{t} \quad \langle S_{\text{eff}} \rangle = 2 \langle S_z \rangle + 7 \langle T_z \rangle = -n_h \frac{6p-4q}{t} \quad (2.6)$$

whereas for lanthanides they are:

$$\langle L_z \rangle = -2 n_h \frac{q}{t} \quad \langle S_{\text{eff}} \rangle = 2 \langle S_z \rangle + 6 \langle T_z \rangle = -n_h \frac{5p-3q}{t} \quad (2.7)$$

where n_h marks the number of holes in the $3d$ transition metal or $4f$ lanthanide orbitals. Note that these sum rules are valid only in the case of isotropic absorption of x-rays using both linear and circular x-rays.

In the case of lanthanide atoms, where the crystal field is weak in comparison with the spin-orbit interaction of the $4f$ electrons, it is possible to separate the contributions of $\langle S_z \rangle$ and $\langle T_z \rangle$ from $\langle S_{\text{eff}} \rangle$. Their absolute values will change in the presence of the crystal field, however their ratio will remain roughly the same as the one obtained for the free atoms [49]. In this

approximation, the spin magnetic moment can be calculated from the following relation:

$$\langle S_z \rangle = \frac{\langle S_{\text{eff}} \rangle}{2 + 6 \frac{\langle T_z \rangle_{\text{free}}}{\langle S_z \rangle_{\text{free}}}}. \quad (2.8)$$

By performing angle dependent XAS and XMCD measurements, information about the magnetic anisotropy of the investigated system can be obtained. In addition, by acquiring the maximum of the XMCD signal as a function of the external magnetic field, magnetization curves can be acquired. The XMLD spectra represent an additional fingerprint of the magnetic ground state of a system. Throughout this thesis, we used them as parameters in our multiplet calculations, to determine the both electronic configuration and magnetic ground state of investigated systems.

2.3.2 Experimental setup and measurements

Performing the XMCD measurements requires a source that can provide a wide range of x-ray energies, high brilliance and a high degree of circular polarization. Therefore, XMCD measurement are performed at synchrotron facilities. All measurements presented in this thesis were performed at the end-station of the EPFL/PSI X-Treme beamline of the Swiss Light Source at Paul Scherrer Institute in Villigen, Switzerland (Figure 2.2). The detailed description of the end-station and the beamline specifications can be found in [50], and in the following only their main characteristics are summarized.

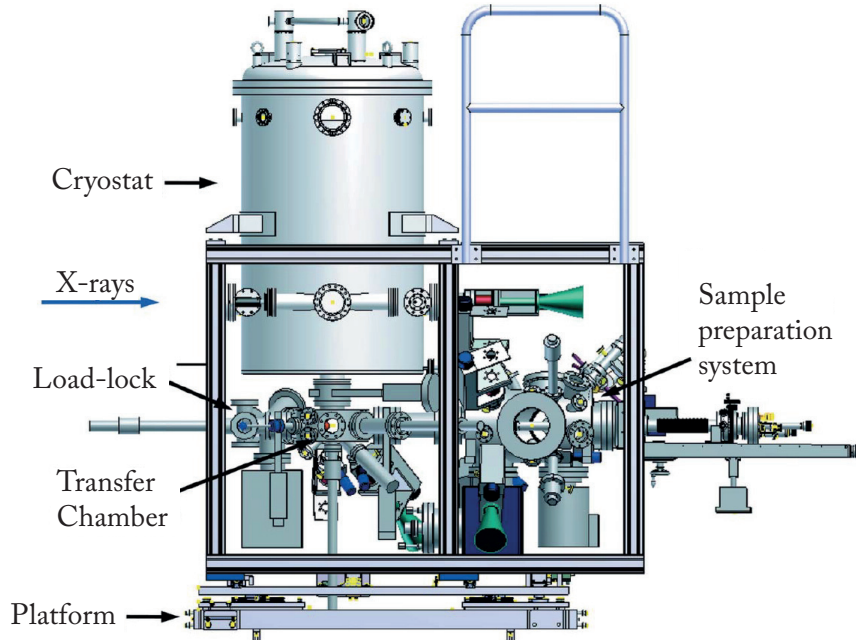


Figure 2.2 – Drawing of the end-station of the EPFL/PSI X-treme beamline where all XAS and XMCD measurements presented in this thesis were performed. The figure is taken from [50].

The X-Treme beamline enables polarization-dependent x-ray absorption spectroscopy in the soft x-ray range, $E = 260 - 2000$ eV. The cryostat of the end-station is equipped with a superconducting vector magnet which can generate magnetic fields up to $B = 7$ T parallel to the direction of x-rays and up to $B = 2$ T in the direction perpendicular to them. Further, in this chamber, a sample is attached to the variable temperature insert which allows adjusting the sample temperature in the $T = 2 - 370$ K range.

The end-station is equipped with the *in situ* sample preparation chamber. This chamber is equipped with an ion sputter gun and heating/cooling stage which enables preparation of samples in $T = 30 - 1800$ K range. In addition, it offers the possibility of attaching evaporators, and is equipped with a variable temperature scanning tunneling microscope. The preparation chamber is connected to the cryostat through the transfer chamber which is kept at the UHV pressure. This enables the transfer of prepared substrates to the cryostat without breaking the vacuum.

The detection of the x-ray absorption signal is carried out by measuring the total electron yield (TEY), where the total number of electrons escaping the sample surface is ascertained from the drain current. Namely, the relaxation of atoms from excited to ground state can result in the emission of high-energy Auger electrons. Subsequently, by inelastic scattering, these electrons produce secondary electrons in the surrounding surface. Due to the very small mean free path of these secondary electrons, TEY is a surface sensitive method, and hence an ideal tool for measuring the adsorption spectrum of surface adsorbed atoms. Furthermore, it allows investigating the systems with coverages down to $\Theta = 0.002$ ML [30]. To eliminate the influence of the variation in the beam intensity on acquired data, the TEY signal was normalized with respect to the beam intensity, I_0 , measured in real-time on the metal grid placed before the cryostat. The absolute photon flux ϕ reaching the sample was measured with a photodiode placed after the last optical element of the beamline and is given in units of $\phi_0 = 3 \times 10^{-3}$ photons nm⁻²s⁻¹.

The measurements were performed for two incidence angles with respect to the surface normal, namely normal incidence at $\theta = 0^\circ$ and grazing incidence at $\theta = 60^\circ$. In both cases the magnetic field was collinear with the incident x-rays. To take into account the different surface areas illuminated by x-rays in the two geometries, the acquired spectra were normalized with respect to the absorption pre-edge of the corresponding element. In addition, prior to the deposition of atoms, the spectra of the clean surface were acquired. They were subsequently subtracted from the acquired atomic spectra to eliminate any contribution from the substrate. The magnetization curves were acquired by recording the maximum of the XMCD intensity as a function of the external magnetic field for each element.

2.3.3 Sample preparation

We used the preparation chamber of the X-Treme beamline to clean and prepare all the surfaces used as supporting substrates for single lanthanide and transition metal atoms. Through this

thesis two monocrystalline metal substrates were used: Ir(111) and Ru(0001). Both substrates were prepared by repeated cycles of Ar^+ sputtering at $T = 300$ K and annealing at $T = 1300$ K. After the cleaning cycles were completed, these substrates were either used for growth of decoupling layers, or were directly, without breaking the vacuum, transferred to the cryostat where the subsequent deposition of atoms took place.

We employed chemical vapor deposition for the growth of two decoupling layers on clean metal substrates, graphene and hexagonal boron nitride (*h*-BN). Graphene was grown by the exposure of 100 Langmuir of ethylene (C_2H_4) to a metal substrate kept at $T = 1400$ K [51, 52], whereas *h*-BN was grown by the exposure of 125 Langmuir of borazine ($\text{B}_3\text{H}_6\text{N}_3$) to a metal substrate kept at 1030 K [53, 54]. Both reactions are self-limiting to one monolayer since the catalytic dissociation of respective precursor molecule requires bare metal areas.

In addition to monocrystalline substrates and *in situ* prepared decoupling layers, we used two commercially available substrates: graphene grown on copper foil and highly oriented pyrolytic graphite (HOPG). Both of these substrates were exposed to air prior to being placed into the preparation chamber. Therefore, to outgas the air contaminations from the inert surface carbon layer, we annealed these substrates at $T = 870$ K. In addition, before the insertion into the preparation chamber, HOPG substrates were cleaved. More detail on these substrates and their preparation is given in Chapter 4.

Lanthanide and transition metal atoms were deposited from high purity rods (99.9%) using an electron-beam evaporator. The atoms were deposited at surfaces kept at low temperatures, normally of about $T = 4$ K; however, in the case of dysprosium, depositions at $T = 40$ K were also made (see Chapter 3 for more details). Prior to experiments, these rods were degassed until a pressure of $p \leq 4 \times 10^{-11}$ mbar was reached. Furthermore, during the beamtime, we kept these rods in the degassing conditions, to degas them even further. Throughout our experiments, we established that lanthanide atoms are particularly sensitive to the contamination. Occasionally, despite using the same experimental procedure, the resulting spectra would differ depending on whether the sample was prepared at the beginning or towards the end of the beamtime. Hence, each sample was prepared multiple times, and only those samples whose spectra did not show any further change with the preparation were considered. A detailed discussion on the effects of the contamination on the spectra of lanthanide atoms will be given in Chapter 5.

Throughout this thesis, the coverage of atoms is given in monolayers (ML). In the case of graphene and *h*-BN, the coverage of $\Theta = 1$ ML corresponds to one atom per their unit cell, whereas in the case of metallic substrates, it is defined as one adsorbate atom per one substrate atom. Further discussion on the coverage determination is given in Chapter 3.

2.4 Multiplet calculations

In addition to sum rules, an analysis of experimental XAS and XMCD spectra can be made by their comparison with simulations carried out within an adequate theoretical frame. One of them is the atomic multiplet theory [55, 56], which together with ligand field theory [57, 58], enables simulating the spectra of atoms subjected to a crystal field by calculating the transitions from the ground to the permitted final states. In the case of $3d$ transition metals, of interest are $2p^6 3d^n \rightarrow 2p^5 3d^{n+1}$ transitions, whereas in the case of lanthanides those are the $3d^{10} 4f^n \rightarrow 3d^9 4f^{n+1}$ transitions. Such multiplet calculations can provide a deeper understanding on the magnetic stability, as they give the complete energy diagram of the investigated system.

The simulation of the polarization dependent XAS spectra is based on the calculations of the transition probabilities presented in Section 2.1.1, and the detailed description of the multiplet calculations can be found in [59, 60]. As previously mentioned, the transition matrix element can be evaluated only when the initial and final states of a system of interest are known. These states are obtained by diagonalization of the Hamiltonian of an atom of interest, to which an electrostatic term representing a crystal field is added [60],

$$H = H_A + H_{CF}. \quad (2.9)$$

Here, the atomic Hamiltonian is given by

$$H_A = \sum_i^N \frac{p_i^2}{2m_e} + \sum_i^N \frac{-Ze^2}{r_i} + \sum_{i<j}^N \frac{e^2}{r_{i,j}} + \sum_i^N \zeta(r_i) \mathbf{l}_i \cdot \mathbf{s}_i, \quad (2.10)$$

where N is the number of electrons in an atom, Z the charge of its nucleus and ζ is the spin-orbit coupling constant. The first term of this Hamiltonian is the kinetic energy of the electrons, the second one represents the electrostatic interaction of these electrons with the nucleus, the third one is the electron-electron repulsion, and the last one is the spin-orbit interaction of each electron. If an atom is subjected to an external magnetic field, a Zeeman term is added to this Hamiltonian,

$$H_Z = \frac{\mu_B}{\hbar} \sum_i^N \mathbf{B} \cdot (2\mathbf{s}_i + \mathbf{l}_i). \quad (2.11)$$

The crystal field Hamiltonian has the following form

$$H_{CF} = -e\phi, \quad (2.12)$$

where ϕ is the potential describing the surrounding ligand field. As has been shown in the previous chapter, the crystal field can be expressed in terms of the Stevens operators and coefficients. However, it can also be expressed in terms of the point charge electrostatic model. Here, the surrounding ligand field is approximated with the collection of point charges, and

the resulting crystal field Hamiltonian is [14]

$$H_{CF} = -e \sum_i^N \sum_j^M \frac{Q_j}{r_{ij}}, \quad (2.13)$$

where Q_j is the strength of the j^{th} point charge. This type of crystal field is suitable for atoms with localized valence electrons which interact only electrostatically with the surrounding crystal field. This is in particular the case for the lanthanide atoms and their well shielded $4f$ orbitals [61, 62].

In the scope of this thesis, we performed multiplet calculations using the multiX code². As explained in the publication describing the working principles of this code [63], it determines the multiplets “from a Dirac density functional atomic calculation, followed by the exact diagonalization of the Coulomb, spin-orbit and crystal field interactions for the electrons in the open shells.” As an input, this code requires the investigated element and its exact electronic configuration. Only integer occupations of valence states are permitted. Further, the crystal field is given in a form of point charges. The coordinates of these charges, as well as their strength, are entered manually and are used as parameters in simulating the XAS, XMCD and XMLD spectra. Finally, the code allows to scale the Coulomb and spin-orbit interactions with respect to their Hartree-Fock values, in order to optimize the simulated spectra.

2.5 Scanning Tunneling Microscopy

The scanning tunneling microscopy (STM) measurements were performed with a homemade low temperature STM, operating at 5 K [64]. Tungsten (W) tips were used for all measurements and the STM images were acquired in constant current mode. The bias voltages given in the figure captions refer to the sample; therefore, at the negative values used, electrons tunnel from occupied states of the sample into empty states of the tip. The samples measured with the STM were prepared using the same procedure described earlier in this Chapter. In this case as well, the samples were transferred to the cryostat without breaking the vacuum and the atoms deposited on the cold surface kept either at $T = 10$ K or $T = 40$ K.

²The code, together with the manual, is available at <https://www.psi.ch/cmt/project-multix>.

3 Dy atoms on graphene/Ir(111)

Dysprosium (Dy) atoms on a graphene/Ir(111) surface make the first superlattice of single atom magnets. This chapter in its first part presents our scanning tunneling microscopy (STM) investigation of the adsorption of Dy atoms on graphene/Ir(111). The remainder of the chapter is devoted to the investigation of the magnetic properties of Dy atoms and their origin by combined XMCD measurements and multiplet calculations.

The majority of the results presented in this chapter are published in R. Baltic, *et al.* Superlattice of Single Atom Magnets on Graphene, *Nano Lett.* **16**, 7610-7615 (2016). The data on coverage and exposure time dependence of Dy XAS spectra will be presented in R. Baltic, *et al.*, Magnetic properties of single rare earth atoms on graphene/Ir(111), *in preparation*.

Work contribution. *As part of a team led by Dr. Stefano Rusponi, I contributed to all XMCD measurements presented in this Chapter. All STM measurements and analysis were performed by Dr. Marina Pivetta. Dr. Stefano Rusponi carried out the multiplet calculations presented in this Chapter. I performed the remaining data analysis. In particular, the analysis presented in Sections 3.3, 3.7, 3.8 and 3.9.*

3.1 Moiré pattern of graphene/Ir(111)

The surface atoms of Ir(111) are ordered in a triangular lattice with the lattice constant of $a_{0,Ir} = 2.73 \text{ \AA}$ [65]. Graphene, on the other hand, consists of carbon atoms ordered in a honeycomb, *i.e.*, hexagonal, lattice. However, the centers of its hexagonal rings form a triangular lattice with a lattice constant $a_{0,g} = 2.46 \text{ \AA}$ [65]. The overlapping of these two triangular lattices, due to the about 10% difference in their constants, results in a moiré pattern. This pattern also has a triangular lattice symmetry with periodicity of about 2.5 nm [66, 67].

Graphene is only weakly bound to the Ir(111) surface through van der Waals forces. This results in their large mean distance of $d_{g-Ir} = 3.4 \text{ \AA}$. As a consequence, the resulting corrugation of the moiré structure is small, and it amounts to less than 0.5 Å over the moiré unit cell [68].

A sketch of graphene adsorbed on Ir(111) is shown in Figure 3.1. It shows three different regions with respect to the positions of the centers of graphene hexagonal rings and iridium atoms [67]. The region where the center of the ring is placed on top of the iridium atom is called *atop* region. This is the weakest bound region of the graphene and, consequently, graphene is here the furthest away from its supporting substrate. The other two, more bound, regions are the so called *fcc* and *hcp* regions. They correspond to the centers of the hexagonal rings being on top of the three-fold hollow sites of Ir(111) surface. The difference between them comes from the atom beneath this hollow site. If the atom below is from the second layer of the iridium surface, this is the *hcp* region, and if it originates from the third layer, it is the *fcc* region.

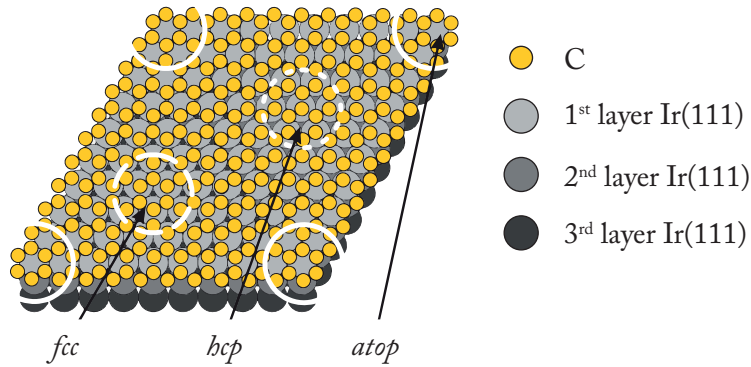


Figure 3.1 – Sketch of graphene on Ir(111) surface. White arcs mark the *atop* regions, dashed circles *fcc* region and dotted circles *hcp* regions. Adapted from [67].

3.2 STM measurements of Dy on graphene/Ir(111)

3.2.1 Disordered Dy on graphene/Ir(111)

Ensembles of individual Dy atoms on graphene/Ir(111) can be obtained by their deposition with an *e*-beam evaporator. Figure 3.2 shows a STM image of one such ensemble after depositing $\Theta = 0.01$ ML of Dy on the substrate kept at $T_{\text{dep}} = 10$ K. Here, one monolayer (ML) is defined as one Dy atom per graphene unit cell. In this image Dy atoms appear as a randomly distributed protrusions on graphene/Ir(111) surface.

3.2.2 Self-assembly of Dy superlattice on graphene/Ir(111)

The scanning tunneling microscopy image in Figure 3.3 shows an ensemble of Dy atoms on graphene/Ir(111) after deposition of $\Theta = 0.01$ ML Dy at $T_{\text{dep}} = 40$ K. At this substrate temperature, surface diffusion of Dy atoms is activated and they can reach the most favorable adsorption site within the moiré unit cell. This results in a superlattice of single Dy atoms.

The potential landscape ruling the formation of the Dy superlattice consists of three com-

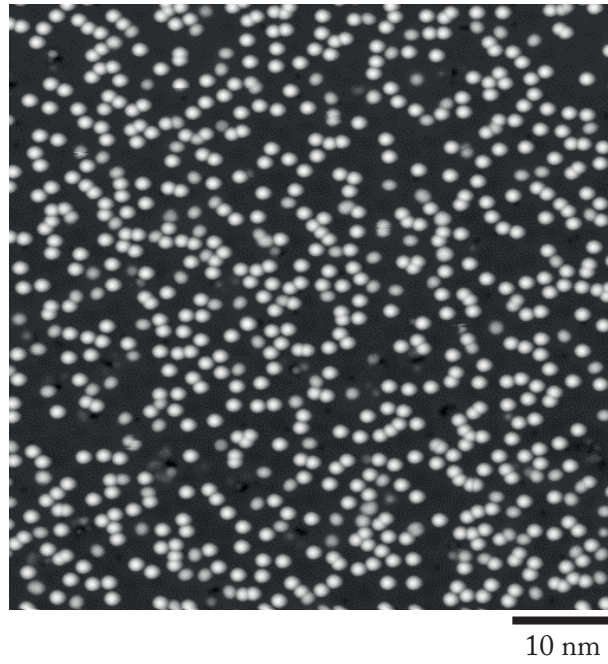


Figure 3.2 – STM image acquired for $\Theta = 0.01$ ML of Dy on graphene/Ir(111) ($V_t = -0.5$ V, $I_t = 20$ pA; $T_{\text{dep}} = 10$ K, $T = 5$ K).

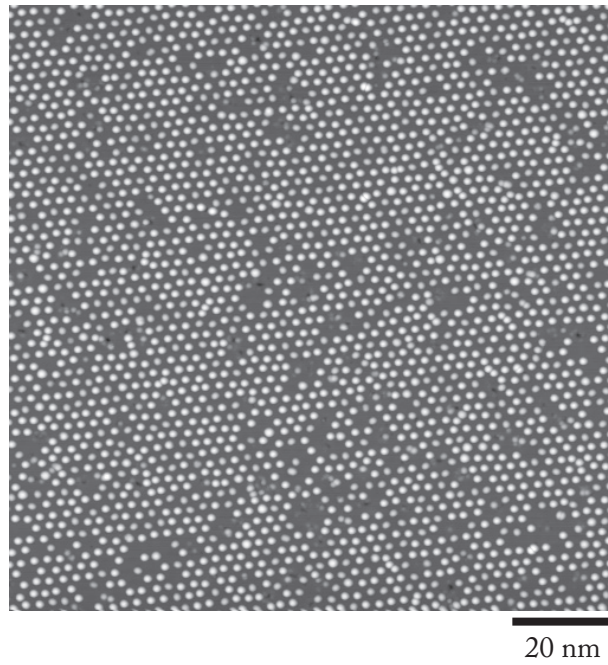


Figure 3.3 – STM image of Dy superlattice on graphene/Ir(111) ($V_t = -0.2$ V, $I_t = 100$ pA; $\Theta = 0.01$ ML, $T_{\text{dep}} = 40$ K, $T = 5$ K).

ponents: the atomic corrugation of the graphene lattice, the long period surface potential due to the graphene moiré, and the Coulomb repulsion between the atoms due to the strong charge transfer from the Dy to the graphene of about $0.7 - 0.8 e$ [69–71]. Similar to the case of Cs atoms on graphene/6H-SiC(0001) [72], the observed superlattice results from the joint effect of the three components. Here the Coulomb repulsion prevents dimer formation upon diffusion, and the moiré potential defines the array of stable adsorption sites.

The equilibrium positions of Dy atoms on the graphene/Ir(111) surface can be determined by comparing the image of pristine graphene with the one with Dy atoms adsorbed on top. These images need to be acquired with similar tunneling conditions, as the apparent heights of the *atop*, *fcc* and *hcp* stacking areas depend on the tunneling parameters [67]. Figure 3.4(a) shows an atomically resolved graphene structure with *atop* regions appearing dark and the *fcc* and *hcp* regions appearing bright. Figure 3.4(b) shows an enlarged detail of the superlattice. By comparing these two STM images, it can be seen that the Dy atoms of the superlattice adsorb in the *atop* stacking region of the moiré pattern, *i.e.*, where the C_6 ring of graphene is centered above an Ir substrate atom. Hence, the mean distance of Dy atoms in the superlattice corresponds to the periodicity of the graphene moiré structure, 2.5 nm.

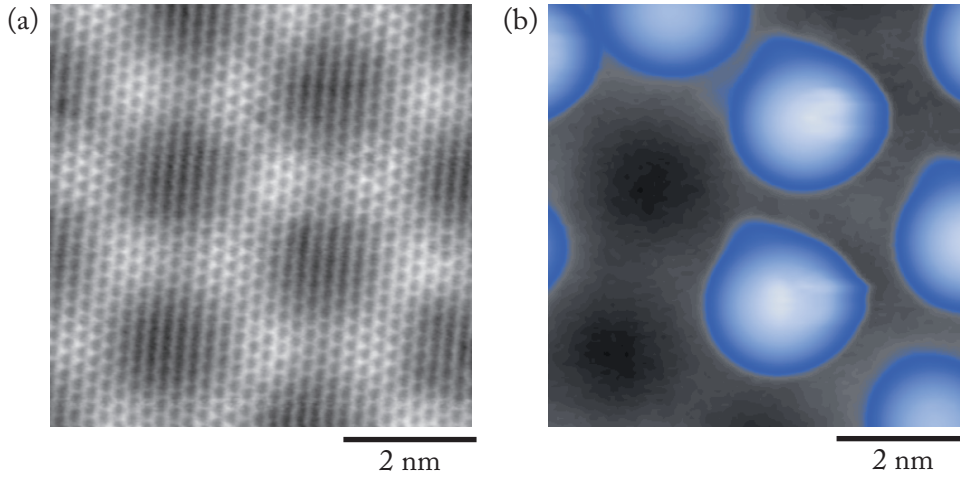


Figure 3.4 – (a) Atomically resolved STM image of the graphene moiré structure; the *atop* regions appear as dark areas ($V_t = -0.02$ V, $I_t = 50$ pA; $T = 5$ K). (b) Detail of the Dy superlattice shown in Figure 3.3 with Dy atoms adsorbed in the *atop* regions of the moiré structure ($V_t = -0.4$ V, $I_t = 20$ pA; $T = 5$ K).

The long range order of the Dy atom superlattice can be illustrated by the autocorrelation function of the STM image [73]. In Figure 3.5(a) the autocorrelation function of Figure 3.3 is shown. It consists of a global maximum in the center of the image, surrounded with satellite maxima lying along the high symmetry directions of the superlattice, the positions of which determine the periodicity of the superlattice. The intensity of the satellite maxima reflects the degree of order of the superlattice [71]. The line cut along one of the high symmetry directions is shown in Figure 3.5(b), and its intensity shows a very shallow decay with distance.

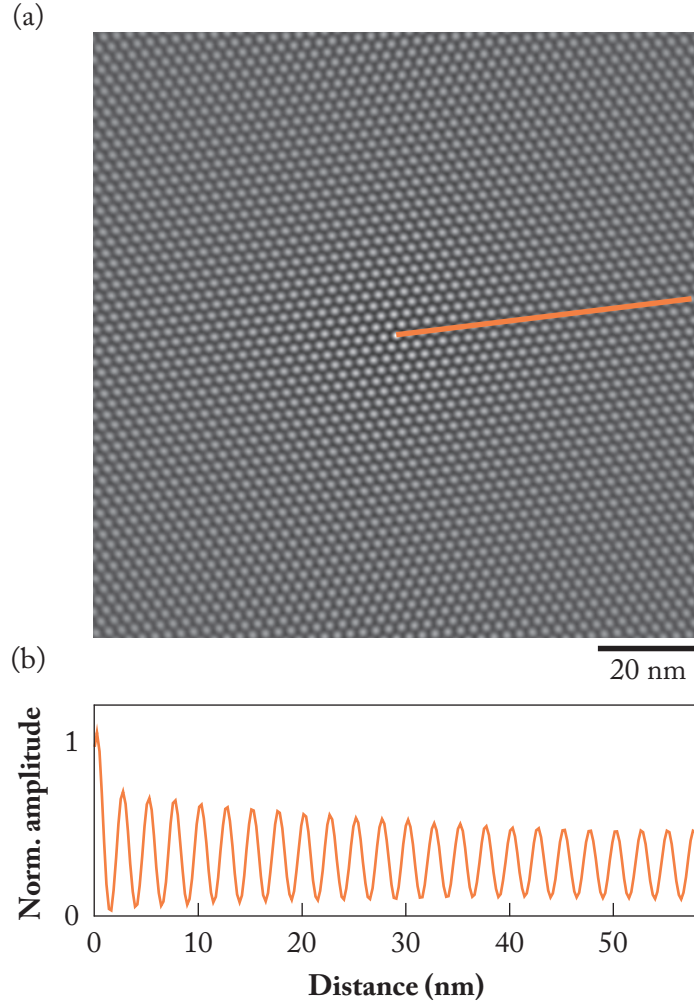


Figure 3.5 – (a) Autocorrelation function of the STM image shown in Figure 3.3. (b) Line cut along the orange line shown in (a).

Dy superlattice forms for a range of sample temperatures during deposition, $30 \text{ K} \leq T_{\text{dep}} \leq 50 \text{ K}$. For $T_{\text{dep}} < 30 \text{ K}$ the inter-moiré cell diffusion is suppressed, resulting in disordered arrangement of adatoms, as demonstrated in Section 3.2.1. These atoms can be found adsorbed in all three stracking areas of the graphene moiré. For $T_{\text{dep}} > 50 \text{ K}$ the diffusing adatoms can overcome the repulsive Coulomb barrier and dimers or bigger clusters form.

3.2.3 Adsorption site of Dy on graphene/Ir(111)

As we have seen in the previous sections, the adsorption of Dy atoms with respect to the graphene moiré can vary depending on the deposition temperature. It is interesting to determine the adsorption site of these atoms with respect to the graphene itself as this adsorption site determines the symmetry and strength of the crystal field acting on them and ultimately

their magnetic properties. For Dy atoms on freestanding graphene, DFT calculations have found a hollow adsorption site [70]. To experimentally determine the adsorption site of Dy on graphene/Ir(111), we performed atomically resolved STM measurements.

Figure 3.6 shows an atomically resolved STM image of graphene with adsorbed Dy atom after deposition at $T_{\text{dep}} = 10$ K. Minor asymmetry of Dy atom originates from the small asymmetry of the STM tip. Hence, to find the adsorption site of this Dy atom, one has to look for the position of its apex. Black lines in Figure 3.6 outline the sixfold graphene hollow sites, *i.e.*, the centers of the hexagonal carbon rings, in the vicinity of the adsorbed Dy atom. Their intersection occurs at the summit of the Dy atom, thus identifying the hollow site as the adsorption site of this atom. The same adsorption site has been determined for Dy atoms in the superlattice. Hence, the same six-fold symmetric crystal field generated by this adsorption site is experienced by both Dy atoms in disordered ensembles and superlattice on graphene/Ir(111).

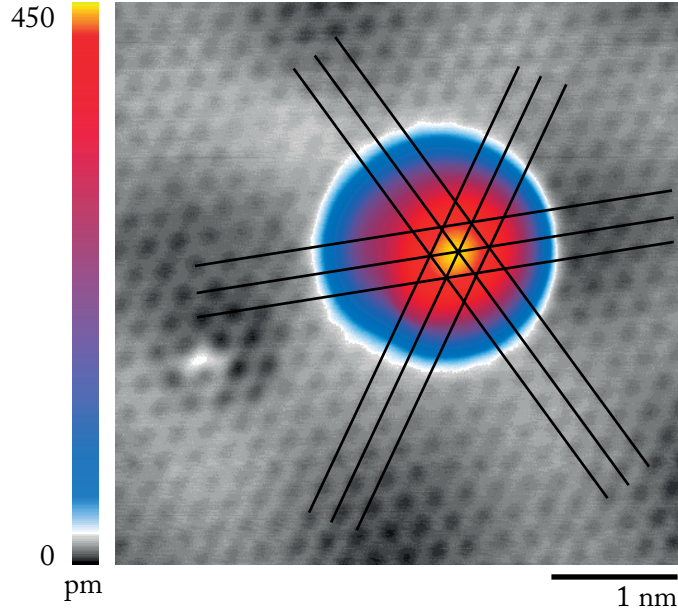


Figure 3.6 – Atomically resolved STM image of graphene/Ir(111) with an adsorbed Dy atom. Black lines mark the hollow sites of the graphene lattice ($V_t = -0.05$ V, $I_t = 500$ pA; $T_{\text{dep}} = 10$ K, $T = 5$ K).

3.2.4 Dy monomers and dimers

A detailed analysis of both ordered and disordered Dy samples reveals presence of two kinds of protrusions at the surface characterized by two different apparent heights. In Figure 3.7(a), a bigger and rounder object is marked with A and a smaller, slightly elongated object with B. From their line profiles, shown in Figure 3.7(b), we measure 0.50 ± 0.02 nm for species A and 0.41 ± 0.02 nm for species B. These absolute heights depend on the bias V_t ; however, for all values employed, species A always appeared significantly higher.

To identify the nature of these two species, we performed manipulations by centering the STM tip on top of them and applying a tunnel voltage ramp. Being subjected to such manipulation, species A was found to be displaced laterally for tunnel voltages exceeding $V_t = \pm 2.5$ V. Species B, on the other hand was split into two objects of type A for tunnel voltages exceeding $V_t = \pm 1.5$ V. The arrow in Figure 3.7(a) points to the object of type B before the manipulation, and arrows in Figure 3.7(b) point to the two objects of type A emerging after the splitting. We therefore identify species A as Dy monomers and species B as Dy dimers. Figure 3.7(d) shows the difference between Figures 3.7(a) and (b), with the split dimer appearing in black, and the two newly emerged monomers in white. The statistical analysis performed over hundreds of protrusions for a Dy coverage of $\Theta = 0.01$ ML reveals that 83 ± 3 % of them are monomers and 17 ± 3 % are dimers both for $T_{\text{dep}} = 10$ K and $T_{\text{dep}} = 40$ K.

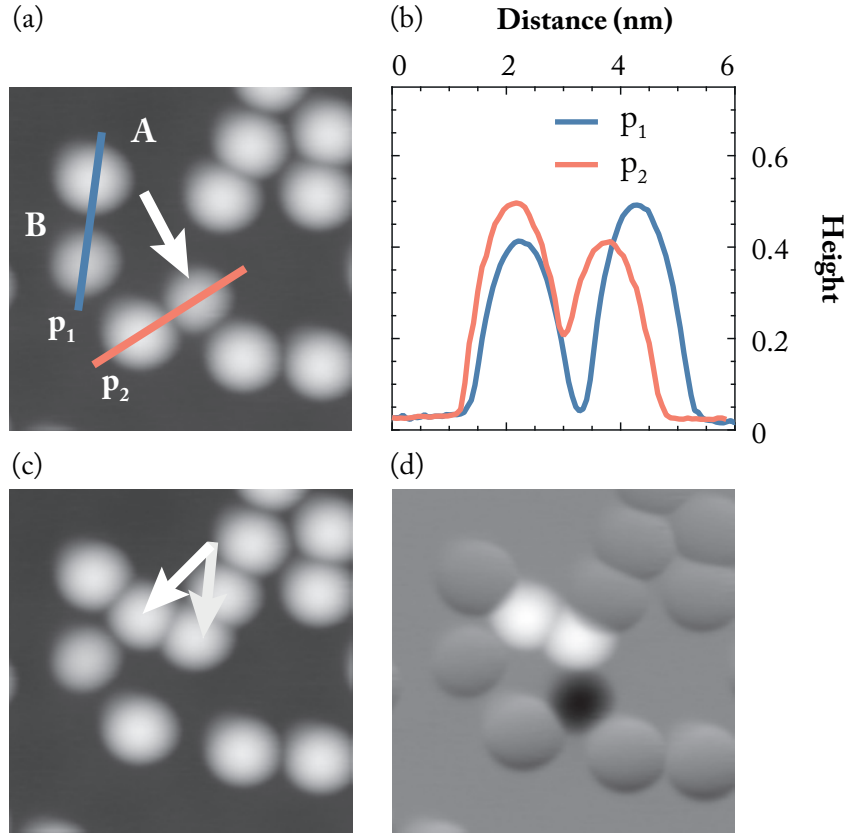


Figure 3.7 – (a,b) Sequence of STM images showing the splitting of a dimer into two monomers by manipulations with the STM tip. The arrow on image (a) points at the dimer before the splitting, and arrows on image (b) point at the two monomers resulting from the split dimer ($V_t = -0.5$ V, $I_t = 20$ pA; 8.3×8.3 nm², $T_{\text{dep}} = 10$ K, $T = 5$ K). (c) Two STM profiles, indicated by dashed lines on image (a), show apparent heights of monomers (A) and dimers (B). Both profiles start at the bottom left of the image and have following sequences: dimer-monomer in red, monomer-dimer in blue. (d) The difference between images (a) and (b), showing the splitting of dimer (black) into two monomers (white).

In addition to these two species, we observed the existence of another type of Dy objects. These objects have a round shape and much smaller apparent height than the other two described before. Upon manipulation with STM, a single such object transforms into a single Dy atom. Hence, we attributed them to the Dy atoms contaminated with hydrogen present in the UHV chamber.

3.3 XMCD measurements for Dy atoms on graphene/Ir(111)

3.3.1 Magnetism of Dy atoms on graphene/Ir(111)

To determine the magnetic properties of Dy atoms on graphene/Ir(111), we performed extensive XAS and XMCD studies of both ordered and disordered Dy ensembles. We studied their properties by probing the $3d \rightarrow 4f$ transitions, *i.e.*, transitions at the Dy $M_{4,5}$ adsorption edges.

The x-ray absorption and magnetic circular dichroism spectra acquired for a disordered ensemble of Dy atoms for $\theta = 0^\circ$ (normal) and $\theta = 60^\circ$ (grazing) incidence angle of x-rays and at $T = 2.5$ K are shown in Figure 3.8(a,b). By comparing these experimentally acquired spectra to the spectra simulated for free Dy atoms, *i.e.*, Dy atoms not subjected to any crystal field, we can anticipate a divalent, $4f^n$, electronic configuration of these atoms. This electronic configuration corresponds to $n = 10$ electrons in Dy $4f$ orbitals and it is the same as the configuration of free Dy atoms.

The large XMCD signal of Dy atoms (Figure 3.8(b)) reveals a presence of large magnetic moments localized in their $4f$ orbitals. Larger intensity of the XMCD signal in normal with respect to the grazing incidence indicates an out-of-plane easy magnetization axis for these atoms. In addition, the same sign of both M_5 and M_4 XMCD features reveals large orbital angular momenta of Dy atoms on graphene/Ir(111).

Figures 3.8(c,d) show XAS and XMCD spectra acquired for the Dy superlattice at $T = 2.5$ K. The features of these spectra are comparable to the ones obtained for the disordered Dy system. Just as in the disordered case, Dy atoms are in their divalent electronic configuration and show an out-of-plane easy magnetization axis. The main difference in the XAS, as well as in the XMCD spectra between ordered and disordered Dy systems is the intensity of the peaks at 1291.8 eV. In case of Dy superlattice, these peaks are more pronounced for both normal and grazing incidence of x-rays.

The XAS and XMCD signal at 1291.8 eV does not originate from divalent Dy atoms. In fact, it originates from trivalent Dy species with $4f^9$ configuration, such as contaminated atoms, dimers and bigger objects, present on the graphene/Ir(111) surface. Due to the larger coverage employed in the preparation of the Dy superlattice, it is likely that this sample contains more dimers than the disordered Dy system whose data is presented here. The Dy superlattice has a coverage of $\Theta = 0.01$ ML, whereas the disordered Dy system has a coverage of $\Theta = 0.004$ ML. In

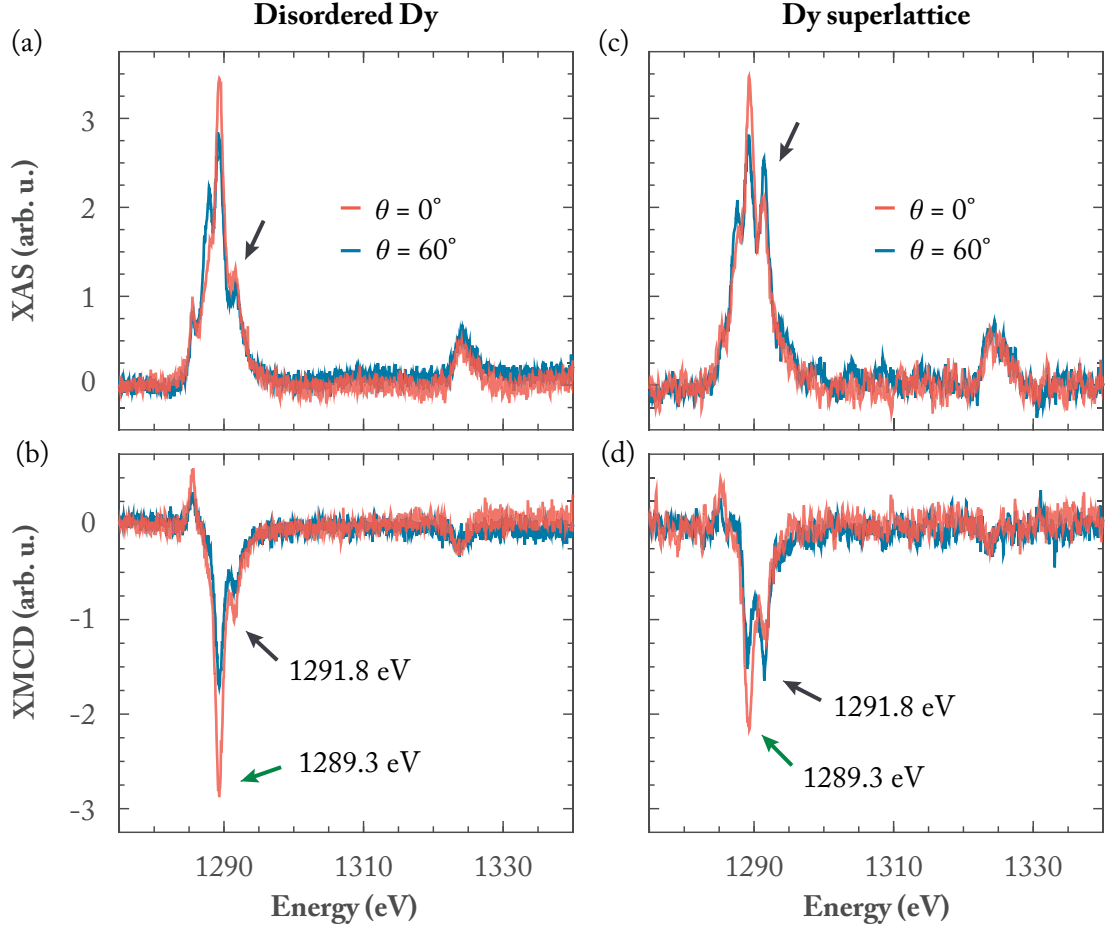


Figure 3.8 – XAS and XMCD spectra of (a,b) disordered Dy system with a coverage of $\Theta = 0.004$ ML ($T_{\text{dep}} = 2.5$ K; $T = 2.5$ K, $B = 6.8$ T) and (c,d) Dy superlattice with a coverage of $\Theta = 0.01$ ML ($T_{\text{dep}} = 40$ K; $T = 2.5$ K, $B = 5$ T) acquired for both $\theta = 0^\circ$ and $\theta = 60^\circ$. The green arrows point to the peaks at 1289.3 eV, while black ones point to the peaks at 1291.8 eV.

addition, unlike the spectra of disordered system which were acquired right after the sample preparation, the spectra of the superlattice were acquired about half an hour later, as this was the time needed to cool down the sample from $T = 40$ K to $T = 2.5$ K. During this additional time, the residual gas of the UHV environment increased the contamination of the superlattice. Thus, both increased amount of trivalent dimers and contaminated atoms resulted in a larger intensity of the spectral feature at 1291.8 eV in the case of the superlattice. The influence of dimers and bigger objects on the XAS spectra and magnetism of Dy atoms will be addressed in detail in Section 3.7, whereas the effects of contamination will be discussed in Section 3.8.

Generally, in case of the single magnetic species on the surface, the maximum of its XMCD intensity is proportional to its total magnetic moment along the beam direction. Hence, by recording this maximum as a function of the external magnetic field, it is possible to acquire the magnetization curve of a given system. In case of multiple species on the surface, it is

possible to acquire magnetization curves of a species of interest by selecting the appropriate energy value for which its spectral features appear.

We acquired the magnetization curves of both ordered and disordered Dy system by recording the intensity of the XMCD peak at 1289.3 eV, with respect to the intensity of the pre-edge at 1282.2 eV, as a function of the magnetic field. This peak is indicated with a green arrow in Figures 3.8(b,d). The resulting magnetization curves for the out-of plane direction are shown in Figure 3.9. Both magnetization curves show clear hysteresis extending up to $B = \pm 5.6$ T. Since we measure in total electron yield (TEY) mode, the data points are highly scattered for small fields ($-0.2 \text{ T} \leq B \leq 0.2 \text{ T}$). Assuming that the magnetization $M(B)$ is linear in that region, we estimate a magnetic remanence of approximately 30% of the saturation magnetization M_{sat} . These hysteresis loops also show several steps which are characteristic of quantum tunneling of the magnetization (QTM) due to the crossing of quantum levels [24]. These steps will be discussed in Section 3.5 in more detail. The magnetization curves acquired on the superlattice and on the randomly distributed atoms are identical within our resolution. This demonstrates that the magnetic properties of Dy atoms are not influenced by their position within the moiré pattern. In addition, since the two systems have different Dy-Dy distance distributions, mutual interactions, either dipolar or substrate-mediated Ruderman-Kittel-Kasuya-Yosida (RKKY), are not significant and in particular not responsible for the observed magnetic stability.

The equality of their magnetization curves shows that, despite some dissimilarities in their XAS and XMCD spectra, Dy atoms in both disordered and ordered systems have identical magnetic properties.

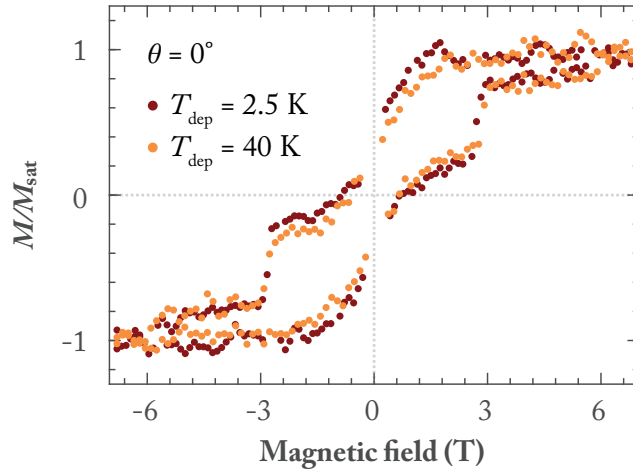


Figure 3.9 – Magnetization curves of the Dy superlattice in orange and randomly distributed Dy atoms in red ($T = 2.5 \text{ K}$, $\theta = 0^\circ$, photon flux $\phi = 5\phi_0$, with $\phi_0 = 0.003 \text{ photons nm}^{-2} \text{ s}^{-1}$, $\dot{B} = 33 \text{ mT s}^{-1}$).

To unambiguously demonstrate the existence of a remanent magnetization, and remove any doubt due to the scattered points around $B = 0 \text{ T}$, we have measured the decay of the Dy XMCD signal at a negative magnetic field value after saturating the sample at a positive field,

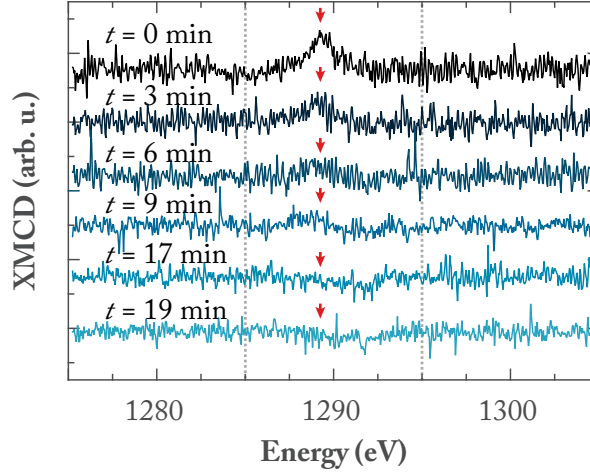


Figure 3.10 – Evolution of Dy XMCD spectra at $B = -0.1$ T and $\theta = 0^\circ$. After saturation of Dy magnetization at $B = 6.8$ T, magnetic field was set to $B = -0.1$ T. Subsequently, an evolution of Dy XMCD spectra was recorded.

i.e., we have measured the decay after crossing $B = 0$ T. We have saturated the magnetization of Dy atoms at $B = 6.8$ T and subsequently ramped down the magnetic field to $B = -0.1$ T. Figure 3.10 shows the evolution of the Dy XMCD spectra during the following 19 minutes. Initially, at $t = 0$ s, Dy shows clear XMCD at 1289.3 eV. This signal is reversed with respect to the ones shown in Figure 3.8(b,d) due to the opposite direction of the magnetic field with respect to the incident x-rays in these two cases. As time passes, the XMCD signal decreases, and it completely vanishes after $t = 17$ min.

Figure 3.11 shows the magnetization curve of Dy atoms acquired at grazing incidence ($\theta = 60^\circ$) at $T = 2.5$ K. This curve also exhibits magnetic remanence and hysteresis up to about $B = 6$ T.

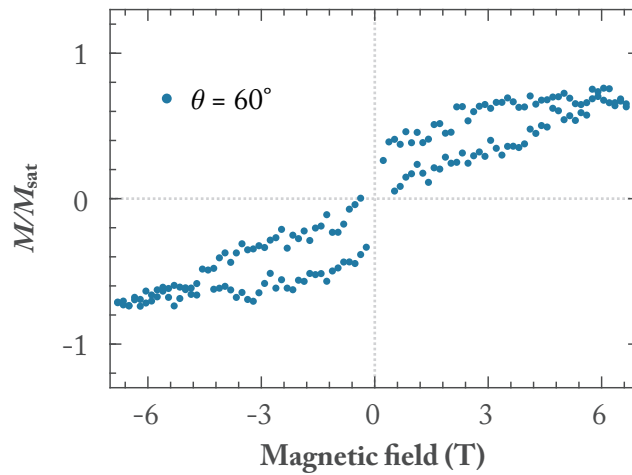


Figure 3.11 – Magnetization curves of the Dy superlattice for $\Theta = 60^\circ$ ($T = 2.5$ K, $\phi = 5\phi_0$, $\dot{B} = 33$ mT s $^{-1}$).

The angular dependence of the out-of-plane component of the magnetic field is given by $\cos\theta$, and at $\theta = 60^\circ$ it is reduced by a factor of two in comparison with $\theta = 0^\circ$. Therefore, simply by considering the geometrical projections, the values at which QTM steps occur should be shifted to twice the field values found for $\theta = 0^\circ$ (Figure 3.9). The QTM step found at $B = 2.7$ T in normal incidence should shift to $B = 5.4$ T when measured at this grazing angle. Instead, we observe a broad step at around $B = 4.5$ T in the hysteresis loop at grazing incidence. We ascribe this discrepancy to the presence of a strong transverse field that enhances the electron and/or phonon mediated relaxation processes and broadens the magnetic field region where QTM occurs [25].

3.3.2 Magnetic lifetime of Dy atoms on graphene/Ir(111)

The magnetic lifetime of the Dy atoms can be investigated by acquiring the decay time of the maximum XMCD intensity after saturating the sample magnetization in an external field and subsequently reducing it to a desired value close to zero, where decay measurements are performed. Figure 3.12(a) shows the magnetic lifetime measurements we performed for Dy atoms on graphene/Ir(111). After saturating their magnetization at $B = 6.8$ T, we measured the decay of the Dy atoms' XMCD signal at $B = 0.01$ T for two different values of the x-ray flux ϕ . For $\phi = 5\phi_0$, which corresponds to the x-ray flux used to acquire the magnetization curves in Figure 3.9, we obtained a magnetic lifetime of $\tau = 284 \pm 12$ s. By reducing the x-ray flux, the magnetic lifetime of Dy atoms increases. Measurements performed with $\phi = \phi_0$ give a magnetic lifetime of $\tau = 971 \pm 71$ s. A similar flux dependence of the magnetic lifetime was observed for Ho/MgO [10] and for molecular magnets [2, 74]. It was ascribed to x-ray induced secondary electrons in the supporting substrate, which through scattering with adsorbed atoms destabilize their magnetic quantum states. Hence, the larger of the two values reported above represents only the lower bound for the intrinsic lifetime of Dy atoms.

When the magnetic lifetime becomes comparable to the acquisition time of each point in the magnetisation curve, narrowing of the hysteresis loop is observed [10]. Figure 3.12(b) shows two magnetization curves of Dy on graphene/Ir(111) acquired with two sets of x-ray flux and acquisition speed values. The curve acquired with $\phi = 5\phi_0$ and $\dot{B} = 33$ mT s⁻¹ shows prominent remanence, while the one acquired with nearly twice the flux and one third of the speed is essentially closed at $B = 0$ T. Overall, the entire hysteresis has become narrower. This confirms that, at the employed flux and field sweep speed, the magnetic lifetime of Dy atoms on graphene/Ir(111) are comparable to the one between successive points in the magnetization curve. Evidently, for very fast or very slow magnetic relaxation with respect to the acquisition time, the magnetization curves are much less sensitive to the measurement parameters. Hence, the flux and field sweep can be optimized for the best signal-to-noise ratio.

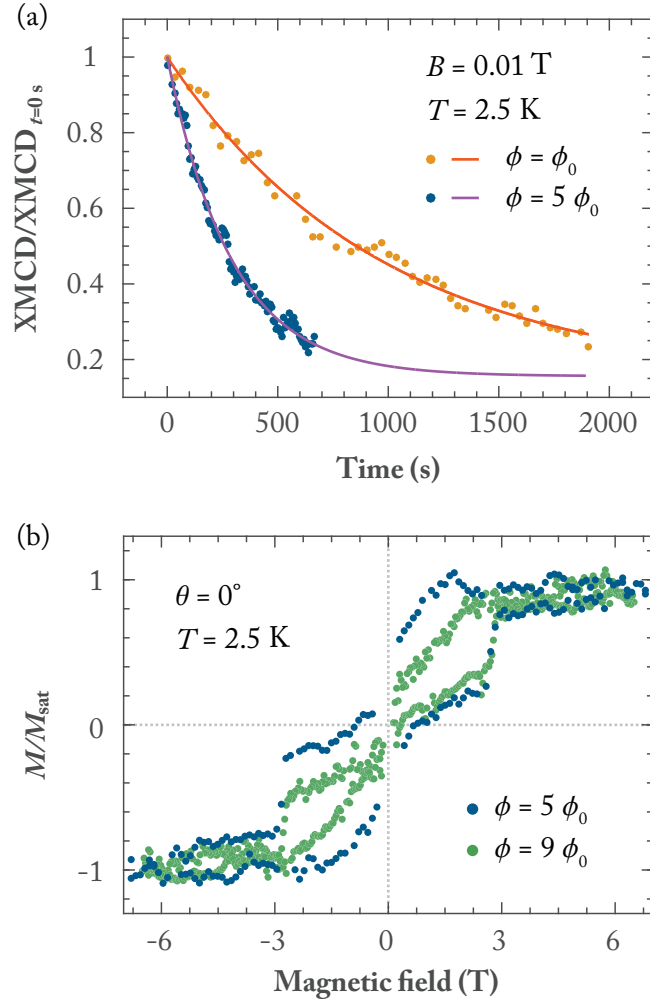


Figure 3.12 – (a) Time evolution of the maximum XMCD intensity at $B = 0.01\text{ T}$ of Dy on graphene/Ir(111) acquired with ϕ_0 (yellow dots), and $5\phi_0$ (blue dots) after saturation of the sample magnetization at $B = 6.8\text{ T}$. Exponential fits (red and purple solid lines, respectively) give the magnetic relaxation time τ . (b) Magnetization curves acquired with two combinations of x-ray flux and acquisition speed values; blue, $\phi = 5\phi_0$ and $\dot{B} = 33\text{ mT s}^{-1}$; green, $\phi = 9\phi_0$ and $\dot{B} = 12\text{ mT s}^{-1}$ ($T = 2.5\text{ K}$, $\theta = 0^\circ$).

3.4 Multiplet calculations for Dy atoms on graphene/Ir(111)

The observation of long magnetic lifetimes for Dy atoms on graphene/Ir(111) indicates that their quantum states are well protected against QTM and direct scattering with electrons and phonons of the surface. To unravel the origin of this remarkable stability, *i.e.*, the ground state, the symmetry and the splitting of the Dy magnetic levels, we carried out multiplet calculations using the multiX code [63]. These calculations were performed with the aim of reproducing the experimentally acquired XAS, XMCD and XMLD spectra. An additional restriction for the simulations was given by the field-dependent crossings of magnetic levels which result in steps in the Dy magnetization curves shown in Figure 3.9. These crossings unambiguously determine the energy splitting of the magnetic levels.

The multiplet calculations include the effect of external magnetic field, finite temperature, incidence angle of x-rays, and crystal field environment on the magnetic atom. Since the Dy atoms adsorb in the six-fold symmetrical (C_{6v}) hollow sites of the hexagonal carbon rings, as demonstrated by the atomically resolved STM image in Section 3.2.3, we simulated the effect of the graphene crystal field with a C_{6v} arrangement of point charges around the Dy atom.

The geometry and the sign of the point charges used in multiplet calculations were inspired by DFT calculations for Dy on freestanding graphene [69, 70]. However, to accurately simulate the experimental spectra, the coordinates and the strength of these charges needed to be finely adjusted. The employed crystal field consists of positive and negative point charges placed at the positions of carbon atoms of the graphene surface, with the addition of a positive charge in the center of the graphene hexagonal ring, just below the adsorbed Dy atom. The exact geometry and strength of employed point charges are given in Appendix A, and their planar representation is shown in Figure 3.13.

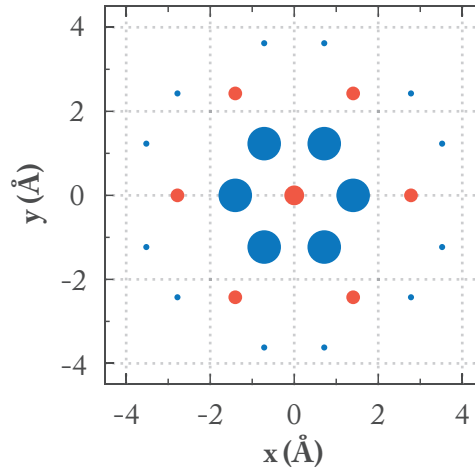


Figure 3.13 – Planar representation of the point charge crystal field employed in the multiplet calculations for Dy on graphene/Ir(111). Positive charges are marked with red, and negative with blue. The size of each circle reflects the charge value. The exact geometry and strength of depicted charges are given in Table A.1.

3.4. Multiplet calculations for Dy atoms on graphene/Ir(111)

The XAS, XMCD and XMLD spectra resulting from multiplet calculations are shown in Figure 3.14(a-c), along with their experimental counterparts (Figure 3.14(d-e)) for easier comparison. The simulated spectra show overall good agreement with the experimental ones. They only differ in the peak at 1291.8 eV observed in the experimental XAS and XMCD spectra and absent in the simulated ones. The origin of this peak are Dy dimers and contaminated monomers present on the surface. These objects are not taken into account by the multiplet calculations as reproducing them would require the knowledge of the crystal field acting upon them. More details on the influence of Dy dimers and contamination on the XAS spectra will be given in Section 3.7 and Section 3.8, respectively.

Multiplet calculations reveal divalent $4f^{10}$ occupation for Dy atoms on graphene/Ir(111), just as was anticipated from the comparison with the simulated spectra for the freestanding Dy atoms. Further, they show that the high spin-orbit coupling characteristic of lanthanides the lowest multiplet with a total angular momentum $J = 8$. The zero field splitting of this multiplet resulting from multiplet calculations is shown in Figure 3.15. The crystal field of graphene splits its levels and promotes a strong uniaxial anisotropy resulting in a ground state with out-of-plane projected moment $J_z = \pm 7$.

In the absence of an external magnetic field, the Dy magnetic quantum states form degenerate doublets. Further, the C_{6v} symmetric crystal field mixes the states that differ by $\Delta J_z = \pm 6$ and forms six classes of eigenstates. These eigenstates are depicted with six different colors in Figure 3.15. Notably, the crystal field strongly mixes states with $J_z = \pm 6$ and $J_z = \pm 3$, resulting in tunnel-split doublets with quenched J_z (this is illustrated with dashed lines in Figure 3.15). In this way, at $B = 0$ T the barrier for thermally assisted magnetization reversal is reduced from 21.4 meV, corresponding to the reversal over the entire total zero field splitting barrier, to only 5.6 meV since the $J_z = \pm 6$ levels offer a thermally activated shortcut for magnetization relaxation.

The remarkable magnetic stability stems from the combination of the Dy ground state and adsorption site symmetry. At $B = 0$ T, the C_{6v} crystal field does not mix $J_z = \pm 7$ states. This results in the degenerate ground doublet for which QTM does not occur. Further, in C_{6v} symmetry the first-order scattering ($\Delta J_z = \pm 1$) with conduction electrons and phonons cannot induce direct transition between these two ground states [23, 75]. Even considering coupling with nuclear spins, *i.e.*, hyperfine interactions, the Dy atoms are protected from QTM in their ground state. In fact, more than half of the isotopes of Dy (56.2 % natural abundance) have no nuclear spin ($I = 0$) and in this case the total moment remains unchanged, and the above considerations are valid. The remaining isotopes have a nuclear spin $I = 5/2$ and its coupling to the integer total electron moment leads to a half integer spin, for which QTM is forbidden due to Kramers' theorem [26]. Thus, the magnetization can reverse only via thermal excitations to the first tunnel-split doublet with $J_z = \pm 6$ at $B = 0$ T, and to the top of the energy barrier in finite fields. This explains the opening of the magnetization curve up to large fields. Additional relaxation can occur due to QTM induced by the hyperfine coupling for finite fields below 20 mT [76].

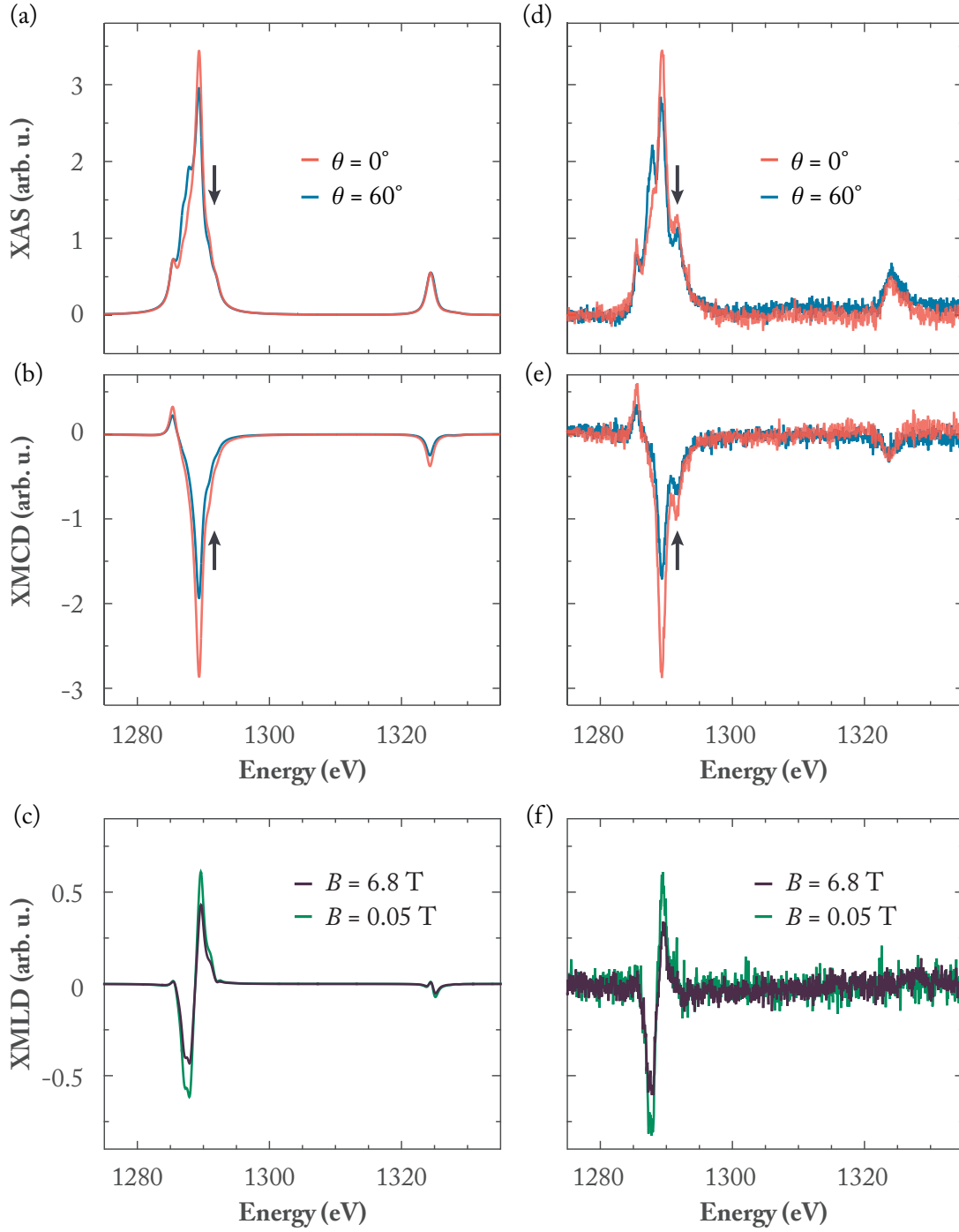


Figure 3.14 – (a-c) XAS, XMCD and XMLD spectra at the $M_{4,5}$ Dy edges resulting from multiplet calculations for single Dy atoms in the C_{6v} CF of graphene. (d-e) Experimentally acquired XAS, XMCD and XMLD spectra for Dy atoms on graphene/Ir(111) ((a,b): $B = 5$ T; $T = 2.5$ K). The arrows point to the peaks at 1291.8 eV in the experimental XAS and XMCD spectra, and their absence in simulated ones.

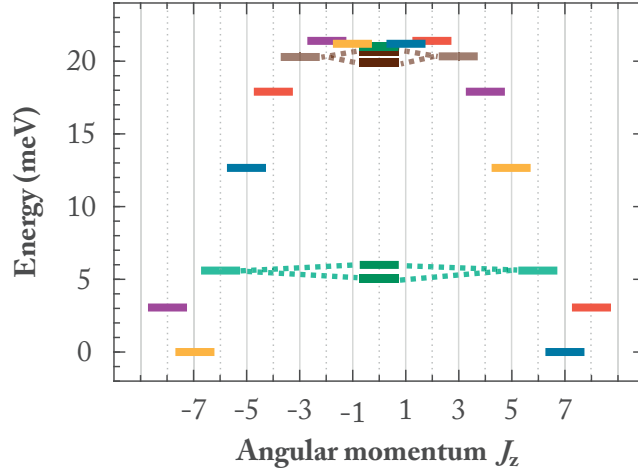


Figure 3.15 – The zero field splitting of the Dy lowest multiplet ($J = 8$) resulting from multiplet calculations. The splitting around $J_z = 0$ is emphasized for better clarity. Each color identifies magnetic quantum states belonging to one of the six classes of eigenstates defined by the C_{6v} group symmetry. Dashed lines connect doublets with quenched J_z .

The observed magnetic bistability of Dy atoms up to $B = \pm 5.6$ T is the consequence of their electronic state but also of the peculiar properties of graphene/Ir(111) which efficiently protects the Dy spin from destabilizing interactions. These interactions are specified in the following paragraphs.

First, from a general point of view, the higher the crystal field symmetry, the lower the number of channels available for QTM [75]. In the limit of perpendicular anisotropy and $C_{\infty v}$ symmetry, QTM is forbidden and the magnetization of an atom has to overcome the entire total zero field splitting barrier to reverse its direction. In this respect, graphene, with its C_{6v} symmetry, represents a superior substrate for minimizing the possibility of direct QTM.

Second, only few vibrational modes exist for an atom adsorbed on a surface [10] which strongly limits the energy and momentum exchange with the substrate phonon bath. The reduced coupling is in particular true for graphene which is the material with the highest stiffness, implying a very small phonon density of states in the few meV energy range of interest [77]. In addition, the vibrational modes of iridium are likely filtered by the graphene layer due to its weak van der Waals coupling to the metallic substrate and by the gap of about 6 – 7 meV in the graphene acoustic out-of-plane phonon modes [77, 78]. Thus, at low temperature, spin-phonon coupling is strongly suppressed.

Third, for graphene/Ir(111) the Dirac point is close to the Fermi level, E_F , and there is evidence for the opening of an energy gap around E_F [79]. This suggests very small, if not zero, electron density at E_F . Moreover, the weak interaction with the iridium substrate pushes the graphene to a mean distance of 3.4 Å from the Ir(111) surface [80], and limits the transmission of the conduction electrons from the iridium substrate through the graphene layer. These three

factors altogether lead to strongly reduced spin-flip events in Dy and enable long magnetic lifetime on graphene/Ir(111).

3.5 Steps in Dy hysteresis

As mentioned in the previous section, additional constraints in multiplet calculations were the magnetic field positions (*i.e.* energy positions) of the steps in the Dy magnetization curves. They appear for $B = 0, \pm 2.7$ and ± 5.6 T, and originate from crossings of magnetic levels and the consequential QTM. To further resolve the origin of these steps and associate them with specific magnetic levels, in Figure 3.16 we plot the Zeeman diagram of the lowest lying Dy states, $J_z = \pm 7, \pm 8, \pm 6$, for the range of magnetic fields used in the experiments. Multiple level crossings occur for this range of magnetic fields; however, only those involving $J_z = \pm 7$ levels influence the magnetization curve, as only these levels are significantly populated at $T = 2.5$ K. In the following we will address each of these crossings individually.

As discussed in the previous section, at $B = 0$ T, the direct transition between the two ground states $J_z = -7$ and $J_z = 7$ is forbidden, and it can occur only via thermal excitation to the $J_z = \pm 6$ states. At $B = 0$ T, the $J_z = \pm 6$ states are strongly mixed in the C_{6v} crystal field symmetry and support QTM, and hence provide a path for magnetization relaxation. This relaxation mechanism is depicted in Figure 3.16(c).

At $B = 2.7$ T, the levels $J_z = 7$ and $J_z = -8$ cross. These states are not mixed in the C_{6v} symmetry of the crystal field, nor can a transition between them occur with the first order scattering in this crystal field symmetry, hence QTM should not occur. The only way to justify the observed sharp step in the magnetization curve is to assume a small C_{3v} term in the crystal field. This term could be arising from, for example, the non-equivalence of the A-B carbon sublattices which affects the electron scattering processes in graphene [81, 82]. This term provides an additional mixing between levels separated by multiples of $\Delta J_z = \pm 3$ and hence grants transition between the levels $J_z = 7$ and $J_z = -8$. This opens a path for a QTM and results in the sharp step in the magnetization curve. The strength of this perturbation can be evaluated from the tunnel splitting $\Delta_{7,-8}$, obtained by applying the Landau-Zener model [83, 84] to the observed magnetization jump. The Landau-Zener model gives the tunneling probability P between two levels J_z and J_z' in constant sweep rate of the longitudinal magnetic field B_z over their crossing [83, 84]: Note that the Landau-Zener model is valid in the regime of high sweeping rates where Δ is independent of the applied sweeping rate [83]. The tunneling probability between the levels $J_z = 7$ and $J_z = -8$ can be estimated from the height of the corresponding step in the hysteresis, *i.e.*, from the ratio of the spins that have tunneled during this crossing and the total amount of spins that have entered the crossing.

This probability equals to $P = 0.71$ and we find $\Delta_{7,-8} = 1.4 \times 10^{-7}$ meV, which is three orders of magnitude smaller than the $\Delta_{-6,6} = 3.2 \times 10^{-4}$ meV splitting at $B = 0$ T due to the C_{6v} CF, obtained by multiplet calculations. A detailed calculation of the tunnel splitting $\Delta_{7,-8}$ is given in the Appendix B. This relaxation mechanism is depicted in Figure 3.16(d).

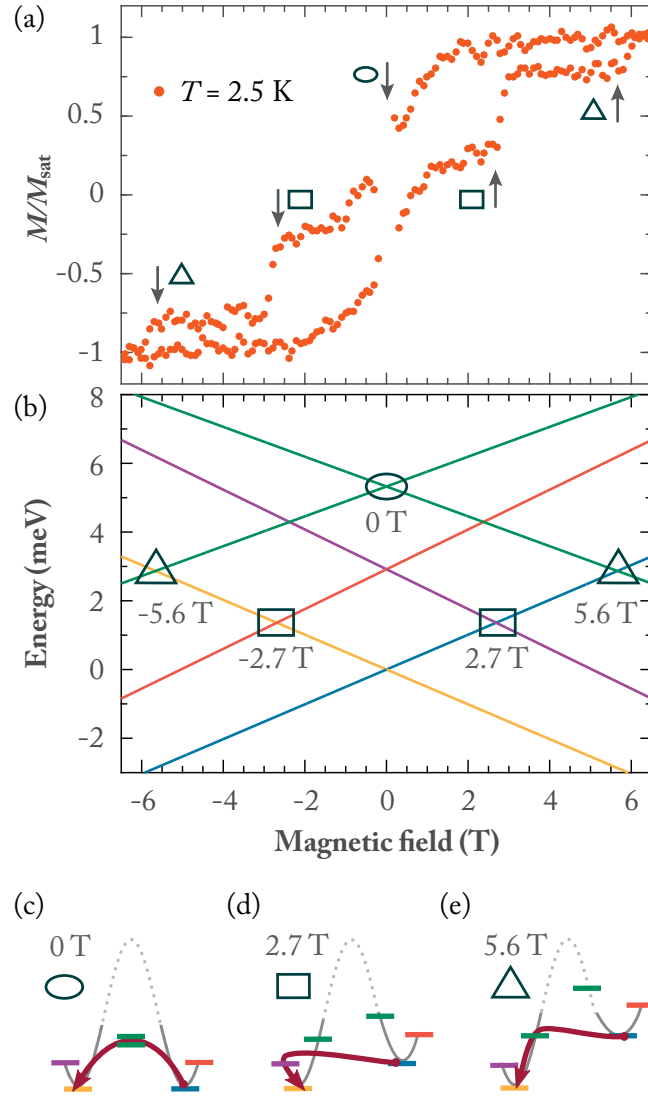


Figure 3.16 – (a) Magnetization curve of Dy on graphene/Ir(111) ($\phi = 5 \phi_0$, $\dot{B} = 33 \text{ mT s}^{-1}$, $T = 2.5 \text{ K}$). (b) Zeeman diagram of the lowest lying Dy magnetic levels between -6.8 T and 6.8 T . The colors follow the color code of Figure 3.15, yellow: $J_z = -7$, blue: $J_z = 7$, purple: $J_z = -8$, red: $J_z = 8$, and green: $J_z = \pm 6$. The triangles mark crossings of ± 7 and ∓ 6 levels at $\pm 5.6 \text{ T}$, rectangles mark crossings of ± 7 and ∓ 8 levels at $\pm 2.7 \text{ T}$, and ellipse marks crossing of ± 6 levels at 0 T . Schematic representation of the relaxation mechanisms: (c) thermal excitation to the $J_z = \pm 6$ mixed doublet in the C_{6v} CF, (d) QTM between the $J_z = \pm 7$ and the $J_z = \mp 8$ crossing states induced by the C_{3v} CF perturbation, (e) QTM mediated by spin-electron or spin phonon scattering.

Finally, the small jump in the magnetization at $B = 5.6 \text{ T}$ corresponds to the crossing between the $J_z = +7$ and $J_z = -6$ states. This crossing is allowed in the C_{6v} crystal field symmetry and grants QTM mediated by first-order electron or phonon scattering [75]. This relaxation mechanism is depicted in Figure 3.16(e).

3.6 Temperature dependence of Dy magnetic lifetime

Given the single atomic layer thickness of graphene, its screening against electron and phonon scattering is effective only at very low temperatures. Figure 3.17 shows the experimentally acquired magnetization curve of Dy atoms at $T = 12$ K and its simulated counterpart. At this temperature, Dy atoms show perfectly paramagnetic behavior. This indicates that their magnetic lifetime is of order of seconds or less, which is the time resolution set by our experimental setup and acquisition parameters. Due to the inability to stabilize the sample temperatures between $T = 3$ K and $T = 12$ K for a substantially long period of time, further investigation of temperature dependence of magnetic lifetime was not possible in that temperature range. As demonstrated for Ho atoms on MgO(111) [10], stronger screening and hence stability at higher temperatures could be achieved by increasing the number of decoupling layers. This could be achieved by growing graphene on insulating substrates.

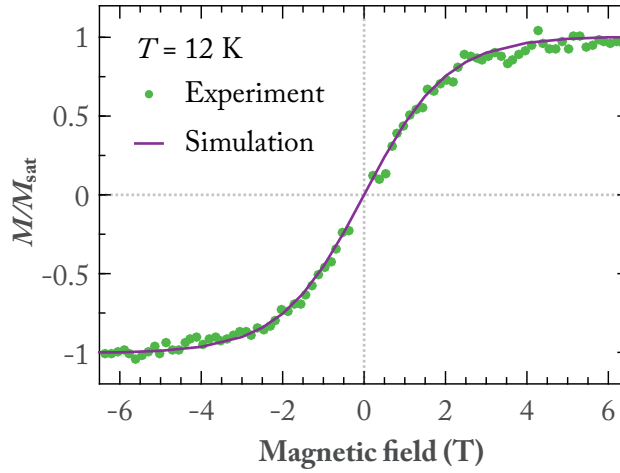


Figure 3.17 – Experimentally acquired and simulated magnetization curve for Dy on graphene/Ir(111) at $T = 12$ K ($\Theta = 0^\circ$, $\phi = 5\phi_0$, $\dot{B} = 33$ mT s $^{-1}$).

3.7 Coverage dependent measurements

3.7.1 Coverage dependence of Dy XAS spectra

The XAS and XMCD spectra of Dy monomers on graphene/Ir(111) are characterized by the pronounced peak at 1289.3 eV (Figure 3.8). However, in the experimental spectra there is an additional peak at 1291.8 eV which is not reproduced in the simulations (Figure 3.14(a,b)). This peak indicates the presence of Dy $4f^9$ occupancy [85] and was associated with Dy dimers. Similar has been observed for Dy atoms on metal substrates, as well as for other lanthanide atoms [85]. To verify this, and to further investigate influence of dimers and bigger clusters on the magnetic properties of an ensemble of Dy monomers on graphene/Ir(111), we performed combined coverage dependent XAS and STM measurements.

Figure 3.18 shows the Dy M_5 edge as a function of coverages between $\Theta = 0.004$ ML and $\Theta = 0.032$ ML for ensembles of disordered Dy atoms. The peak at 1291.8 eV is present in the XAS spectra for coverages as low as $\Theta = 0.004$ ML, and its intensity increases with increasing Dy coverage. At $\Theta = 0.032$ ML this peak has similar intensity to the peak at 1289.3 eV. The increasing intensity of the 1291.3 eV peak and its tail also result in the shift of the 1289.3 eV peak towards higher energy values with increasing Dy coverage. Hence, the increase in the intensity of the peak at 1291.3 eV with increasing coverage can be attributed to the formation of Dy dimers and bigger clusters. It also demonstrates the presence of Dy dimers on the graphene/Ir(111) surface for coverages as low as $\Theta = 0.004$ ML. The observed difference in the valency between Dy monomers and Dy dimers stems from the increased coordination of the Dy atoms [85].

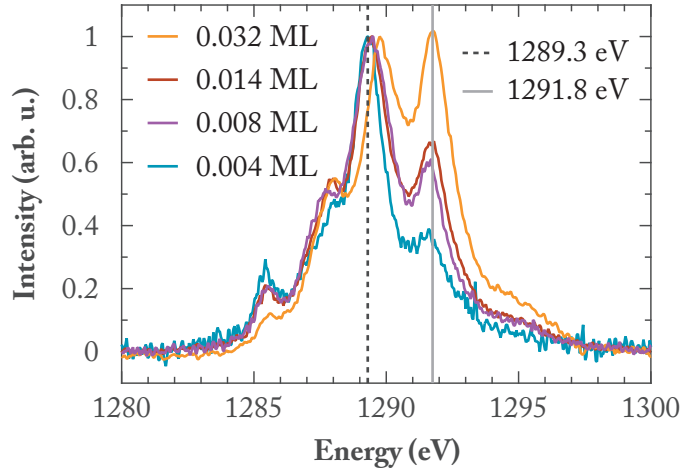


Figure 3.18 – Coverage dependence of Dy XAS spectra at the M_5 edge acquired at $\theta = 0^\circ$. All spectra were normalized to the intensity of the peak at or near 1289.3 eV. Lines mark the position of peaks associated with divalent Dy atoms at 1289.3 eV (black dashed line) and trivalent Dy clusters at 1291.8 eV (grey solid line).

To verify that the source of the additional multiplet features in Dy XAS are indeed dimers, we performed coverage dependent STM measurements. Figure 3.19(a-e) show STM images for Dy coverages comparable to the ones employed in the XAS measurements. In these images, Dy monomers appear as protrusions with larger apparent height and circular shape, while dimers have smaller apparent height with oblate shape, as already shown in Section 3.2.4. Figure 3.19(f) shows the coverage dependence of the average size of Dy objects on graphene/Ir(111). The average size $\langle s \rangle$ increases with increasing coverage from 1.02 atoms for $\Theta = 0.002$ ML, to 1.32 for $\Theta = 0.019$ ML. This size dependence, and hence the dimer abundance, at employed temperatures and coverages is inconsistent with statistical growth [86]. However, similarly to what has been observed for Er on Cu(111) [87], it can be explained by the large direct impingement area for the deposited Dy atoms. Only by considering 37 graphene sites as a direct impingement area can account for such a large dimer abundance at such low Dy coverages [71].

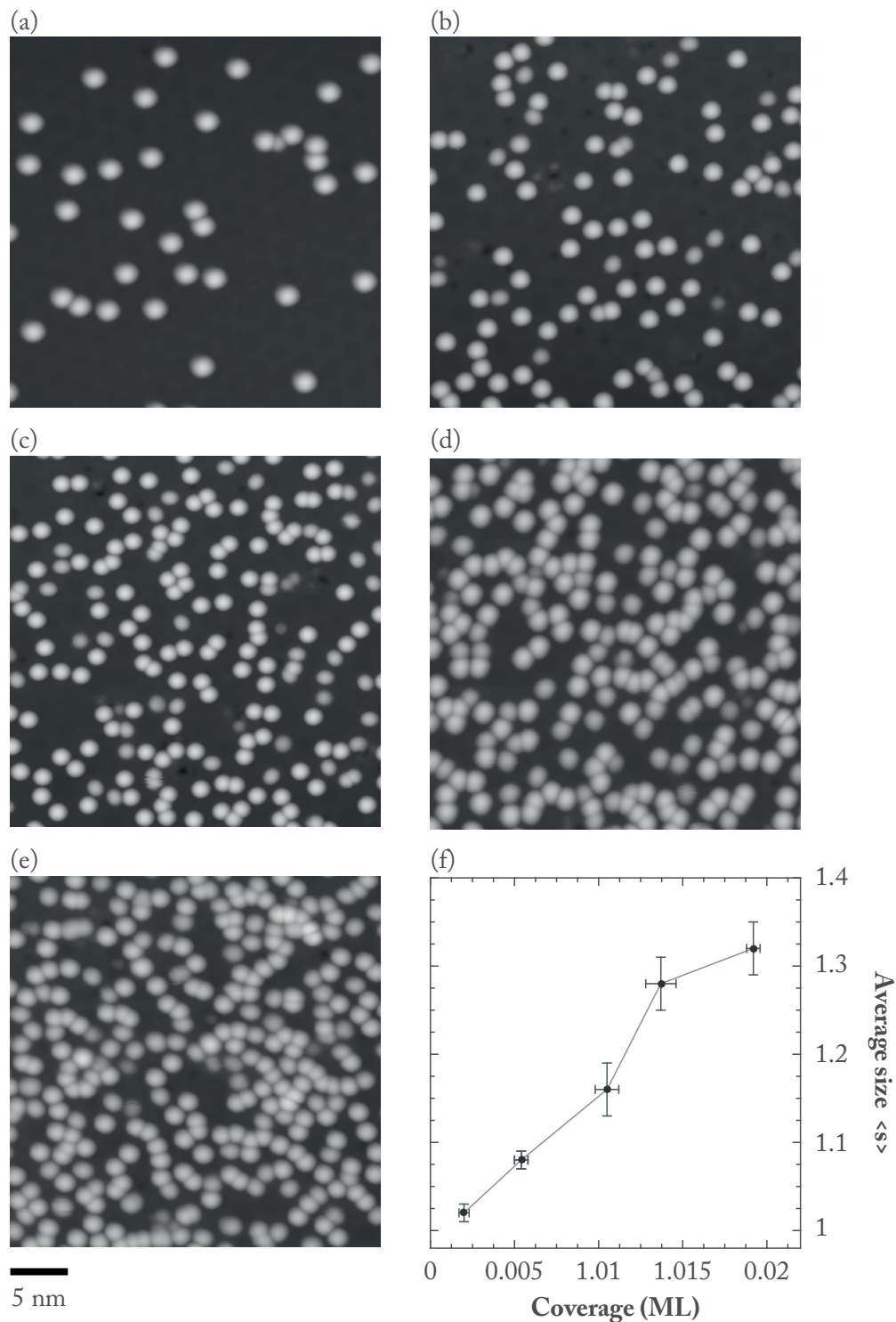


Figure 3.19 – STM images for (a) $\Theta = 0.002$ ML (b) $\Theta = 0.005$ ML, (c) $\Theta = 0.010$ ML, (d) $\Theta = 0.014$ ML and (e) $\Theta = 0.019$ ML of Dy. The indicated scale of 5 nm applies to all images ((a,c-e): $V_t = -0.5$ V, $I_t = 20$ pA, (b): $V_t = -0.2$ V, $I_t = 100$ pA; $T_{\text{dep}} = 10$ K, $T = 5$ K). (f) Coverage dependence of Dy average cluster size deduced from STM measurements. Grey line serves as a guide for the eyes.

3.7.2 Coverage dependence of Dy magnetization curve

Figure 3.20 shows XMCD spectra and magnetization curve for $\Theta = 0.026$ ML of Dy on graphene/Ir(111). The much larger intensity of the XMCD peak at 1291.8 eV with respect to the one at 1289.3 eV reveals the presence of a large amount of trivalent Dy species at the surface. In addition, these two peaks greatly overlap and a large part of the peak at 1289.3 eV originates from the tail of the peak at 1291.8 eV. This means that by recording the magnetization curve at the peak of Dy monomers, a large contribution to the curve comes from trivalent Dy species. Figure 3.20(b) shows magnetization curve acquired for this sample at 1289.3 eV. The resulting magnetization curve still shows hysteresis, but it is much narrower in comparison to those in Figure 3.9 acquired for $\Theta = 0.004$ ML and $\Theta = 0.01$ ML of Dy. In addition, the characteristic QTM steps are barely visible. This indicates that the magnetic interaction of Dy atoms with neighboring atoms/clusters shortens the magnetic lifetime of the measured system. In addition, it suggests that Dy dimers, the primary contributors of the trivalent signal, have a paramagnetic behavior.

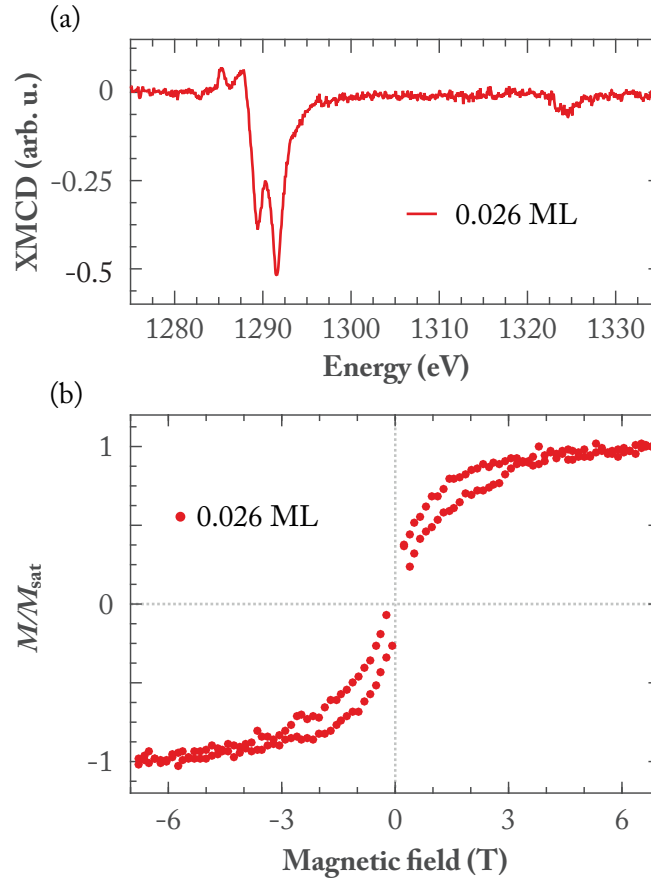


Figure 3.20 – (a) XMCD spectra, and (b) magnetization curve for $\Theta = 0.026$ ML of Dy ($T = 2.5$ K, $\theta = 0^\circ$; (a) $B = 6.8$ T, (b) $\phi = 5\phi_0$, $\dot{B} = 33$ mT s $^{-1}$).

3.8 Exposure time dependence of Dy XAS spectra

In addition to the change in shape of Dy XAS spectra with increasing coverage shown in Section 3.7, we observed similar change in the spectra with exposure time of Dy atoms to the residual gas of the UHV environment. Figure 3.21 shows four XAS spectra at the Dy M_5 edge acquired over the course of five and a half hours of measurements. Initially, right after the deposition the peak at 1291.8 eV is small. However, as the exposure time increases, its intensity increases which, in addition, causes a shift of the peak at 1289.3 eV towards higher energies. The divalent lanthanide atoms on surfaces are known to be highly reactive and sensitive to contamination [88]. Hence, we associate this change in the spectra to the contamination of Dy monomers with the residual gases in the cryostat, most likely hydrogen, and resulting change in their $4f$ occupation.

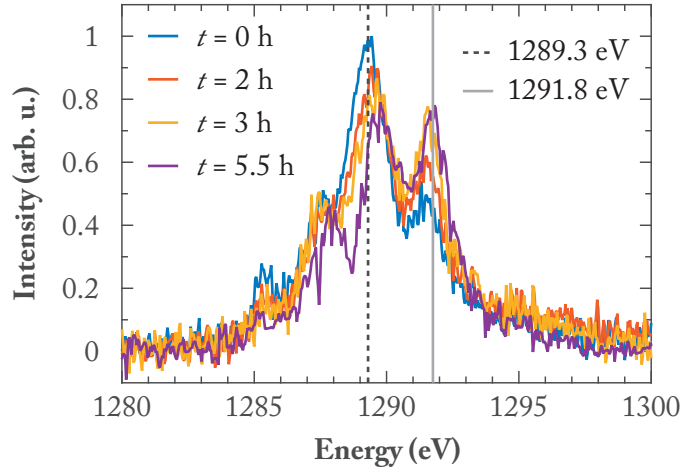


Figure 3.21 – Exposure time dependence of XAS spectra for $\Theta = 0.01$ ML Dy on graphene/Ir(111) at the M_5 edge ($T = 2.5$ K, $\theta = 0^\circ$, $B = 6.8$ T). Dashed lines mark the positions of peaks associated with divalent Dy atoms at 1289.3 eV (black dashed line) and trivalent Dy objects at 1291.8 eV (grey solid line).

3.9 Coverage calibration

The most straightforward and accurate way of determining the coverage of atoms on surfaces is doing it by the means of STM. However, in most cases such calibration is not possible due to the time limitations at the synchrotron facility. In addition, transferring sample from XAS to the STM chamber requires warming it up to the room temperature. This can, in addition to the formation of clusters, lead to the intercalation of surface atoms to the underlying substrate which will obstruct the accurate determination of the coverage.

For samples whose coverage cannot be determined directly by STM, it can be determined indirectly, with the help of a reference sample. The reference sample can be any sample whose coverage was previously determined by STM, and it was related to its integrated area of the

total XAS spectra, t . We used Er atoms on Pt(111) as a reference sample, for which the area of total XAS $t = 1.03$ was associated with the STM determined coverage of $\Theta = 0.09$ ML. Here $\Theta = 1$ ML corresponds to one Er atom per each atom of the Pt(111) substrate, and it includes the difference in the covalent radii of Er and lanthanide atoms in general, with respect to the one of Pt atoms. This difference implies that lanthanide atoms cannot be packed with the same density as the TM substrate atoms [87]. An unknown coverage of a sample can then be calculated with the following formula:

$$\Theta(s) = \Theta(r) \frac{t(s) b(s) h(r)}{t(r) b(r) h(s)}, \quad (3.1)$$

where b is the value of the background at the pre-edge of the corresponding lanthanide atom, h is the number of holes in its $4f$ orbitals, s denotes sample whose coverage is unknown and r the reference sample. In case of decoupling layers grown on metallic substrate, further scaling can be applied to express the coverage with respect to these layers. For instance, in case of graphene grown on Ir(111), a factor 0.8 arising from the difference in areas of their unit cells can be applied to the coverage obtained from Equation 3.1 to express the coverage with respect to the graphene unit cell.

Determining the coverage of Dy atoms on graphene/Ir(111) solely by using the total area of their XAS spectra would, however, lead to vastly inaccurate estimations of their coverages. For these samples, there are both divalent Dy atoms with 4 holes and trivalent ones with 5 holes in their $4f$ orbitals present on the surface, and, before applying Equation 3.1, their contributions to the total XAS area have to be separated. Fitting the spectra with multiple peaks and assuming that only additional peaks in the M_5 edge, with respect to simulated spectra in Figure 3.14(a), belong to the trivalent species has proven to give faulty results. This is due to the fact that the contribution of trivalent species to the M_4 edge is not included in these considerations. Hence, we have taken a different approach. After scaling all the experimental spectra to 1 and shifting them to the same energy, we fitted their features with multiple Lorentzians. In Figure 3.22(a), a fit for the lowest Dy coverage is shown. We attributed the area of the rightmost peak of its M_5 edge to trivalent Dy objects and the remaining features of both M_5 and M_4 edges to divalent Dy atoms. The cumulative fits for all coverages, that outline the experimental spectra, are shown in Figure 3.22(b). To obtain the area of each of these fits that belongs to trivalent Dy, we simply subtracted the area of monomers obtained for the lowest Dy coverage, as shown in Figure 3.22(b). This way, the contribution of trivalent species to both M_5 and M_4 edge is taken into account. Subsequently, to obtain a percentage of trivalent Dy for each spectra, a share of trivalent area in total XAS area was calculated. The values for both divalent and trivalent Dy species for each coverage are given in Table 3.1.

Now that the contributions of divalent and trivalent species have been separated, Equation 3.1 can be applied to both of these species separately. The total coverage of Dy atoms for each sample is the sum of these two contributions. The values for each of these coverages, as well as the total coverages for each of these samples are given in Table 3.1.

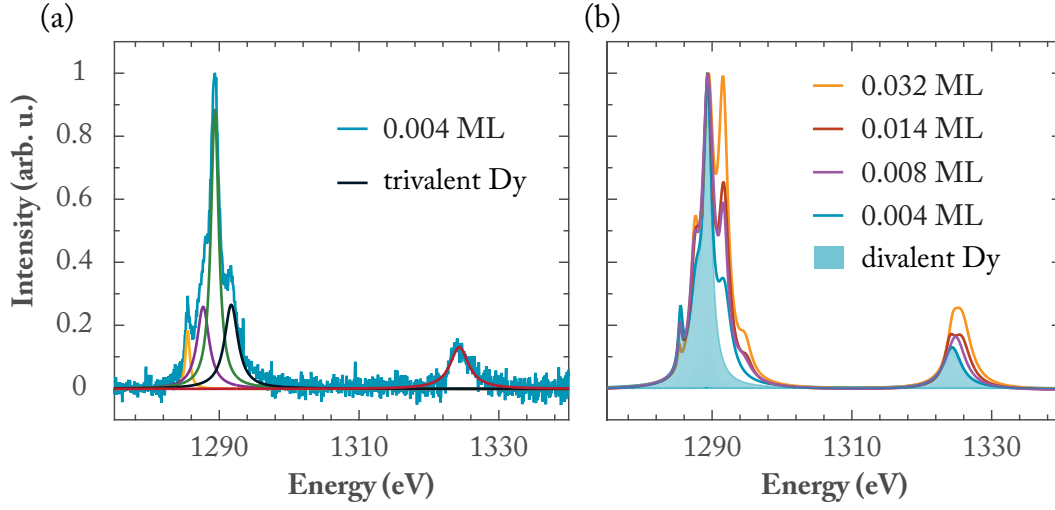


Figure 3.22 – (a) Multiple peak fit of the XAS spectra for Dy sample with coverage of $\Theta = 0.004$ ML using multiple Lorentzian lineshapes. (b) Outlines of four different Dy XAS spectra resulting from their fitting with multiple Lorentzian lineshapes. Blue area marks the share of divalent Dy in each of these spectra. The remaining area belongs to the trivalent Dy species.

Table 3.1 – Share of divalent and trivalent Dy species and their coverages for four different samples of Dy on graphene/Ir(111). $\Theta_{\text{Dy } 2+}$ and $\Theta_{\text{Dy } 3+}$ are, respectively, coverages of divalent and trivalent Dy species for each sample, while Θ_{Dy} is the total Dy coverage.

sample	divalent Dy (%)	trivalent Dy (%)	$\Theta_{\text{Dy } 2+}$ (ML)	$\Theta_{\text{Dy } 3+}$ (ML)	Θ_{Dy} (ML)
A	78	22	0.003	0.001	0.004
B	63	37	0.005	0.004	0.008
C	61	39	0.009	0.005	0.014
D	50	50	0.018	0.014	0.032

The above described method provides a crude estimate of the coverage of Dy. However, it once more emphasizes the sensitivity of divalent Dy atoms to their environment and contamination. The STM measurements presented in Section 3.2.4 and XAS measurements were performed in two different UHV chambers, the walls of which are kept at two different temperatures. Cold walls of the chamber surrounding the sample trap the molecules of the residual gas of the UHV environment. The walls of the XAS UHV chamber are kept at the liquid nitrogen temperature, whereas the ones in the STM chamber are kept at the liquid helium temperature. Hence, STM chamber provides a better vacuum environment for the sample as it also traps the hydrogen molecules. During several days of STM measurements Dy monomers have shown practically no increase in contamination, whereas we have observed a substantial increase in trivalent Dy species over the course of several hours of XAS measurements (see Section 3.8 for more details). Therefore, an increased amount of trivalent species for XAS samples as compared to the STM samples with similar Dy coverage is expected.

4 Dy on Ir(111) and several decoupling substrates

Dysprosium atoms on graphene/Ir(111) show a long magnetic lifetime at $T = 2.5$ K. At the heart of this sizable magnetic stability lies the extraordinary decoupling power of a single graphene layer. To demonstrate this further, in Section 4.1 we probe the magnetic properties of Dy atoms on bare iridium surface. The hybridization of graphene with an underlying metal substrate can greatly influence the magnetic properties of adsorbed atoms. To investigate the possibility of adjusting magnetic properties of Dy atoms through this substrate hybridization, in Sections 4.2, 4.3 and 4.4 we investigate their properties on graphene/Cu, graphene/Ru(0001) and on highly oriented pyrolytic graphite (HOPG), respectively. Finally, in Section 4.5 we investigate whether it is possible to achieve magnetic stability of Dy atoms in a lower, three-fold crystal field symmetry, but with a larger electronic screening from the metallic substrate, by studying their magnetic properties on hexagonal boron nitride (*h*-BN).

The results for Dy on graphene/Ru(0001) and Dy on *h*-BN/Ir(111) are published in R. Baltic, *et al.* Superlattice of Single Atom Magnets on Graphene, Nano Lett. **16**, 7610-7615 (2016). For this thesis, additional multiplet calculations were performed for Dy on *h*-BN/Ir(111) to obtain a better match between the simulated and experimental XMLD spectra and magnetization curves. These simulations, together with the resulting energy level diagram are presented in Section 4.5.

Work contribution. *As part of a team led by Dr. Stefano Rusponi, I contributed to all XMCD measurements presented in this Chapter. Further, I carried out the data analysis and multiplet calculations. The multiplet calculation presented in Section 4.5 represent the continuation of the work started by Dr. Stefano Rusponi. The STM image in Section 4.3 was acquired by Dr. Marina Pivetta.*

4.1 Dy atoms on Ir(111)

After depositing minute amounts of Dy atoms on a bare Ir(111) surface, we recorded their XAS, XMCD and XMLD spectra. The resulting spectra of Dy atoms in C_{3v} crystal field symmetry of

Ir(111) are shown in Figure 4.1(a-c). The XAS spectra of Dy atoms on Ir(111) have a lineshape characteristic of Dy $4f^9$ occupation [32], containing a multiplet feature with the highest intensity in both XAS and XMCD spectra at 1291.8 eV. The shape and intensity of the XMCD spectra are independent of the incidence angle of x-rays, indicating a negligible magnetic anisotropy of this system.

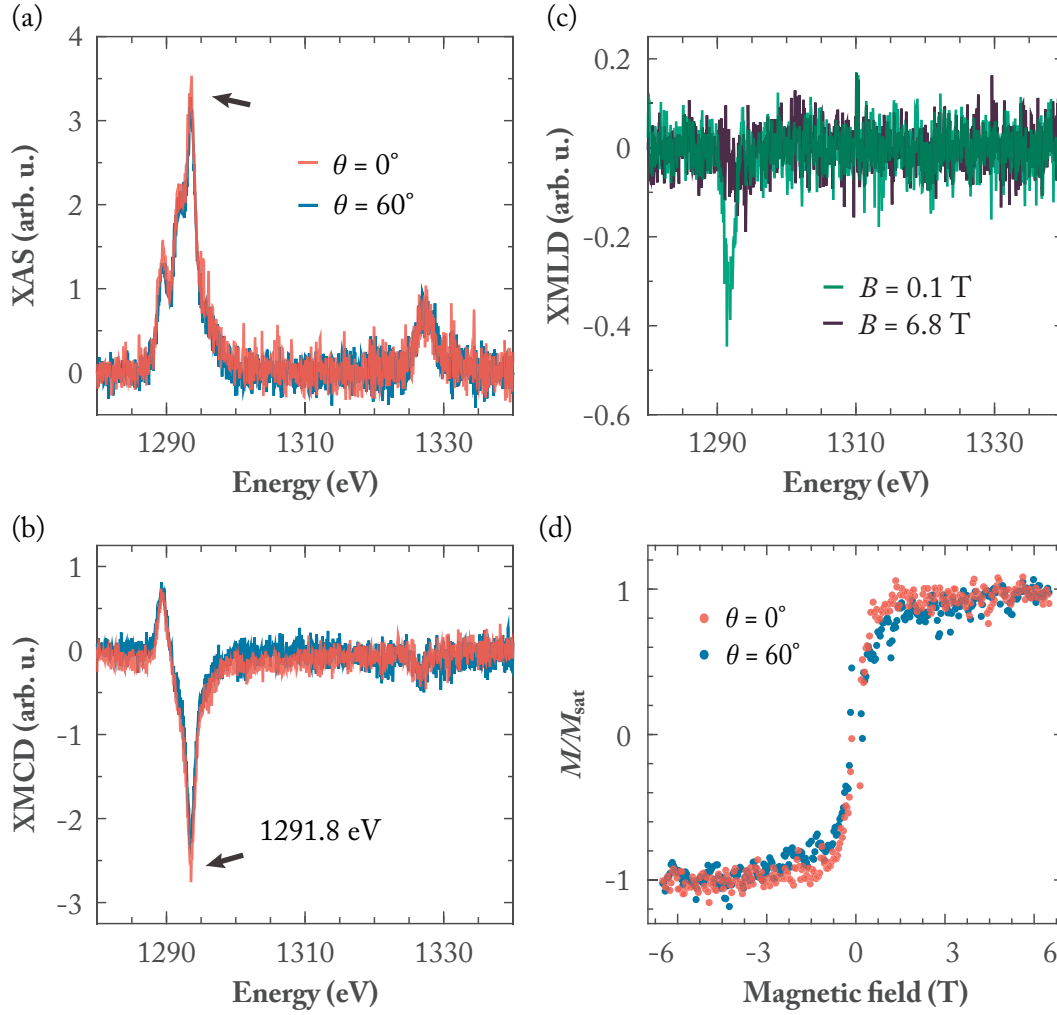


Figure 4.1 – Experimentally acquired (a) XAS, (b) XMCD and (c) XMLD spectra at Dy $M_{4,5}$ edges for $\Theta = 0.002$ ML Dy on Ir(111). The arrows point to the peak at 1291.8 eV. (d) Magnetization curve acquired by measuring the XMCD signal at 1291.8 eV as a function of the magnetic field ($T_{\text{dep}} = 4$ K, $T = 2.5$ K, $\phi = 9\phi_0$, with $\phi_0 = 0.003$ photons $\text{nm}^{-2} \text{s}^{-1}$; (a,b) $B = 6.8$ T, (c) $\dot{B} = 12$ mT s^{-1}).

We acquired the magnetization curves of Dy atoms on Ir(111) by recording the intensity of their XMCD peak at 1291.8 eV in both normal and grazing incidence, in the range of magnetic fields between $B = 6.8$ T and $B = -6.8$ T. The acquired curves are shown in Figure 4.1(d). Dy atoms on Ir(111) show a clear lack of magnetic hysteresis, and a perfectly paramagnetic magnetization curve. This indicates magnetization lifetime shorter than a few seconds at

$T = 2.5\text{ K}$, which can be ascribed to the strong interaction of Dy atoms with the electrons and phonons of the Ir(111) substrate. A similar effect has been observed for lanthanide atoms on other metal substrates [11, 85, 87].

By comparing the spectra acquired for Dy on Ir(111) with those of Dy on graphene/Ir(111) shown in Figures 1.8 and 1.14, it can be seen that clear differences exist. These differences cannot simply be ascribed to the difference in the crystal field symmetry as Dy atoms have different electronic configurations on these two substrates. The interaction of Dy atoms with graphene/Ir(111) results in a divalent $4f^{10}$ configuration, whereas the interaction with bare Ir(111) surface results in a trivalent $4f^9$ configuration. Further, Dy atoms on graphene/Ir(111) show sizable magnetic stability, which is completely absent for those on Ir(111). The contrasting properties of Dy atoms on these two substrates further highlight the remarkable decoupling properties of a single graphene layer. A single graphene layer is sufficient to decouple Dy atoms from the electrons and phonons of the Ir(111) substrate and enable their long magnetic lifetime.

4.2 Dy on graphene/Cu foil

Similar to graphene on Ir(111), graphene on copper is weakly bound to its substrate through van der Waals forces, resulting in similar graphene-metal distances in these two cases. In the case of graphene on Cu(111), their mean distance is $d_{g-Cu} = 3.26\text{ Å}$ [89], whereas for graphene on Ir(111) it is $d_{g-Ir} = 3.4\text{ Å}$ [68]. Assuming a similar interaction between graphene and polycrystalline copper foil as in the case of graphene/Cu(111), a similar mean separation can also be expected between graphene and Cu foil.

Since Dy atoms on graphene/Ir(111) show considerable magnetic stability, we studied their magnetic properties on graphene/Cu foil to see whether the same is valid in the latter case. Further, by comparing these two cases, we intended to investigate the influence of small variations of graphene-substrate interaction on the magnetic properties of adsorbed atoms.

4.2.1 Preparation of graphene/Cu substrate

Rather than preparing the graphene/Cu substrates ourselves, we used commercially available monolayer graphene films grown on copper foils¹. In this way we could also explore whether such commercial substrates, which have been exposed to the contamination from air, are suitable for experiments that require high quality surfaces with low contamination.

The thin graphene/Cu foils were $50 \times 100\text{ mm}^2$ in size, and in order to be used in experiments, they needed to be cut into smaller pieces and fixed onto a sample holder. Figure 4.2(a) shows an example of one of the samples used in our experiments. The graphene/Cu foil was placed on a tantalum sample holder and it was fixed by a molybdenum mask and stainless steel

¹Monolayer graphene films grown on copper foils were bought from www.6carbon.com.

screws. To clean it before the deposition of atoms, we annealed this substrate for five minutes at about $T = 870$ K. Both warming up to the annealing temperature and cooling down were performed slowly, to avoid damaging the graphene layer due to the thermal shock. The entire procedure lasted for about 20-25 minutes. Before the deposition of atoms, the substrate was further cooled down to $T = 2.5$ K.

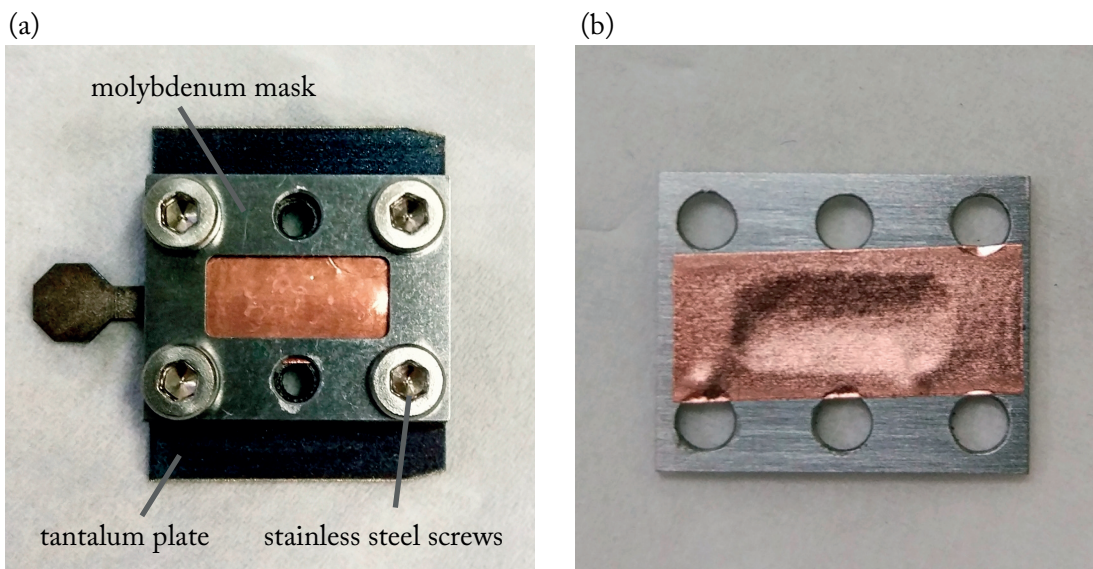


Figure 4.2 – (a) Sample holder with the graphene/Cu foil. It consists of a tantalum plate and molybdenum mask, in between which is the graphene/Cu foil. The mask is fixed to a plate with stainless steel screws. (b) Back side of the molybdenum mask with graphene/Cu(111) foil after performing the experiments.

Figure 4.2(b) shows the back side of the molybdenum mask with the copper foil stuck on it, after the measurements were performed and the sample was taken out of the UHV chamber. It can be seen that the copper foil became severely bent in the process of annealing and cooling down. To reduce the risk of having any side effect from the sample deformation, we performed measurements on the edge of the sample.

4.2.2 Magnetism of Dy atoms on graphene/Cu foil

After the deposition of Dy atoms on graphene/Cu foil, we performed x-ray measurements. The resulting XAS, XMCD and XMLD spectra are shown in Figure 4.3. They look comparable to the ones of Dy on graphene/Ir(111) shown in Figures 1.8 and 1.14, indicating a similar magnetic state of Dy atoms in these two cases. The higher intensity of XMCD spectra in normal with respect to the grazing incidence of x-rays (Figure 4.3(b)), indicates an out-of-plane easy magnetization axis of this system. In addition, both XAS and XMCD spectra have their highest intensity at the peak at 1289.3 eV which is associated with divalent Dy monomers. The peak at 1291.3 eV indicates the presence of trivalent Dy dimers and contaminated monomers on this surface.

The XMLD spectra in Figure 4.3(c) seemingly have different shape with respect to the ones shown in Section 3.4 for Dy on graphene/Ir(111). However, their multiplet features appear at the same energy in both cases, only their relative intensities differ. In addition, the XMLD

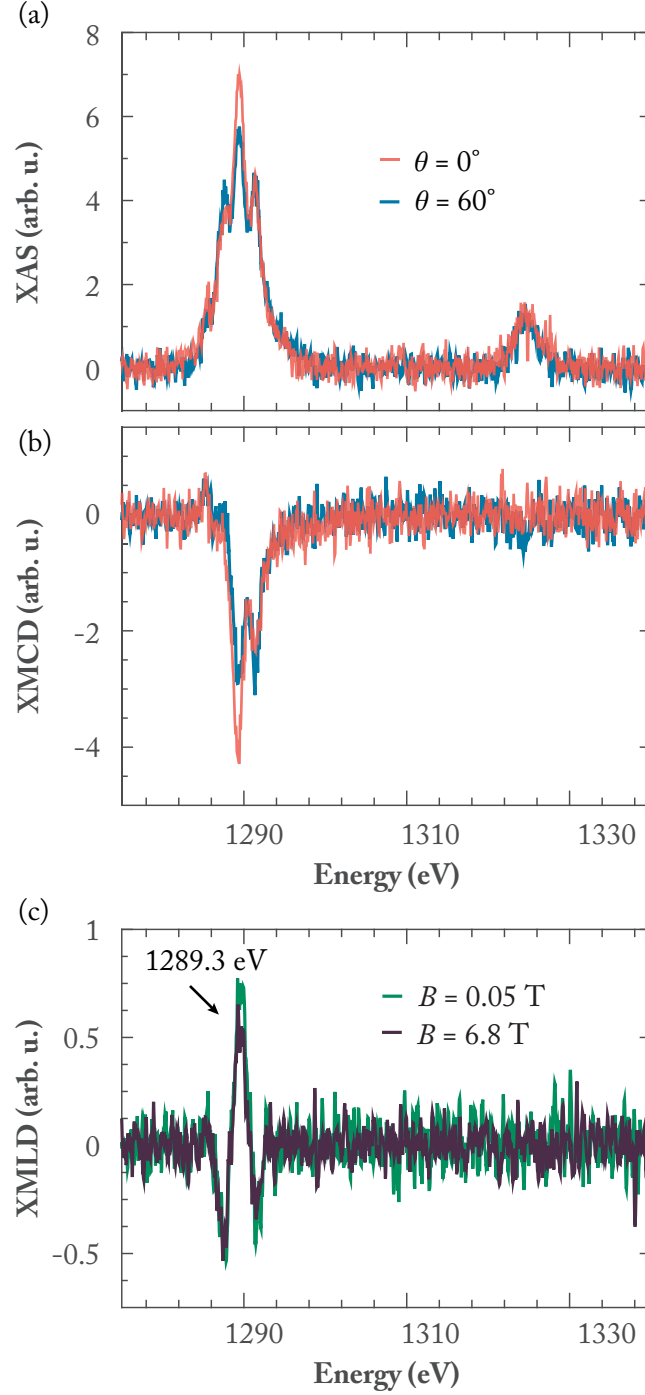


Figure 4.3 – (a) XAS, (b) XMCD and (c) XMLD spectra of $\Theta = 0.005$ ML Dy on graphene/Cu foil at Dy $M_{4,5}$ edges ($T_{\text{dep}} = 2.5$ K, $T = 2.5$ K, (a,b) $B = 6.8$ T).

spectra of Dy atoms on graphene/Cu have, for the same height of the XAS spectra, 40% lower XMLD intensity at the peak at 1289.3 eV.

The magnetization curves acquired for two different coverages of Dy atoms on graphene/Cu, $\Theta = 0.005$ ML and $\Theta = 0.01$ ML, are shown in Figure 4.4. Both magnetization curves show clear hysteresis. In case of a lower coverage, the characteristic steps at $B = 2.7$ T are barely visible due to the increased level of noise; however, in case of higher coverage they are clearly visible. For magnetic fields larger than $B \approx \pm 3$ T, these magnetization curves seem to be closed, and Dy atoms no longer show bistability.

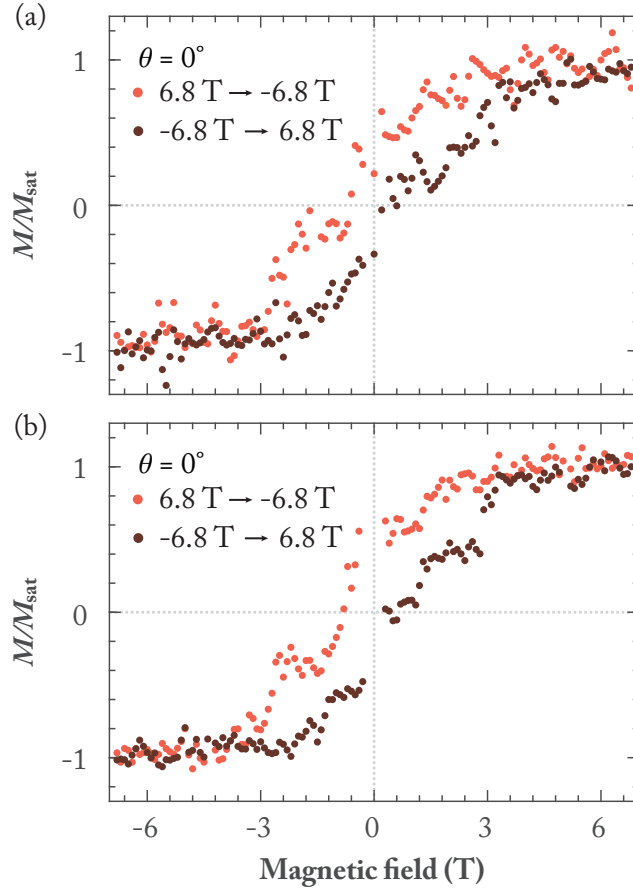


Figure 4.4 – Experimentally acquired magnetization curve for (a) $\Theta = 0.005$ ML and (b) $\Theta = 0.01$ ML Dy on graphene/Cu foil at 1289.3 eV ($T_{\text{dep}} = 2.5$ K; $\theta = 0^\circ$, $T = 2.5$ K; $\phi = 5\phi_0$, $\dot{B} = 33$ mT s $^{-1}$).

Due to the noise and a lack of points at fields around $B = 0$ T, it is difficult to unambiguously judge the behavior of magnetization curves in this region. In both magnetization curves, the branch acquired for $B = 6.8 \rightarrow -6.8$ T hints towards the presence of magnetic remanence at $B = 0$ T, and the branch acquired for $B = -6.8 \rightarrow 6.8$ T seems to indicate its absence. To unequivocally show whether Dy atoms on graphene/Cu have magnetic remanence at $B = 0$ T further experiments are needed.

In comparison with Dy atoms on graphene/Ir(111), Dy atoms on graphene/Cu have a smaller area of hysteresis for the same acquisition conditions, *i.e.*, the same x-ray flux and acquisition speed. The lifetime over the full range of hysteresis is therefore shorter in case of Dy atoms on graphene/Cu. This can be rationalized by comparing the positions of Fermi levels, E_F , for these two substrates. In the case of graphene/Ir(111), there is evidence for the opening of an energy band gap around E_F [79], whereas in the case of graphene on Cu(111) E_F is above the Dirac point, making it *n*-doped [90]. Adsorption of adatoms and consequential charge transfer to the graphene surface causes the upward shift of E_F with respect to the Dirac point [91]. This makes graphene on Ir(111) *n*-doped and results in larger *n*-doping for graphene on Cu(111). As a consequence, for comparable charge transfers from Dy atoms to these two surfaces, Dy atoms on graphene/Cu(111) will be subjected to more scattering events with electrons which will ultimately results in their reduced magnetic stability on this surface.

4.3 Dy on graphene/Ru(0001)

4.3.1 Properties of graphene/Ru(0001)

Unlike the other two systems of graphene/metal substrates studied, graphene/Ir(111) and graphene/Cu, graphene grown on Ru(0001) is strongly bound to its substrate by localized covalent bonds [92]. This results in a strong buckling of graphene on this substrate. In the regions where graphene is strongly hybridized with ruthenium, the carbon atoms are 2.2 Å above the Ru(0001) surface, whereas in the regions where there is only weak interaction between them, their distance is 3.7 Å [92, 93]. The lattice mismatch between graphene and Ru(0001), with their lattice constants being $a_{0,g} = 2.46$ Å [65] and $a_{0,Ru} = 2.706$ Å [94], results in a moiré structure with periodicity of about 3 nm [92]. Due to the varying hybridization between graphene and ruthenium, this moiré has highly inhomogeneous electronic structure with a weakly metallic or semimetallic character [95, 96].

4.3.2 Magnetism of Dy atoms on graphene/Ru(0001)

Experimentally acquired XAS, XMCD and XMLD spectra of single Dy atoms on graphene/Ru(0001) are shown in Figure 4.5. The XAS and XMCD line shapes, with their characteristic peaks at 1289.3 eV and 1291.8 eV reveal presence of Dy species with different $4f$ occupations on the surface. The large intensity of the peak at 1291.8 eV indicates a large amount of trivalent Dy species, which at the investigated coverage of $\Theta = 0.004$ ML cannot be ascribed only to Dy dimers or contaminated monomers. We ascribe it to Dy atoms in their trivalent $4f^9$ configuration.

Figure 4.6 shows an STM image of $\Theta = 0.002$ ML Dy on graphene/Ru(0001). In this image, Dy atoms appear as protrusions with different apparent heights depending on the adsorption site in the moiré cell. Our analysis reveals that 55% of Dy atoms are adsorbed in the atop region of the moiré, and the remaining 45% are adsorbed in other regions. Depending on their

absorption site with respect to the graphene moiré, the interaction between Dy atoms and supporting substrate can result in different electronic configurations and magnetic properties. In the case of adsorption sites where graphene is strongly hybridized with ruthenium, $4f^9$

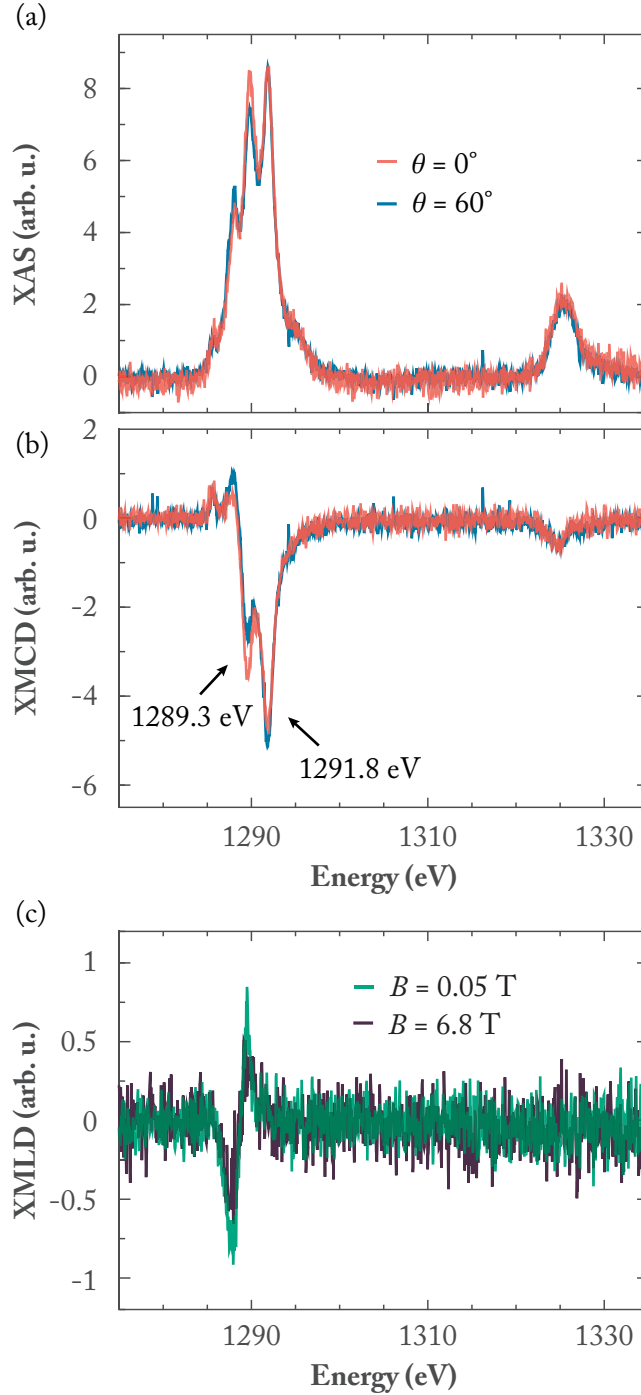


Figure 4.5 – Experimentally acquired XAS, XMCD and XMLD spectra at Dy $M_{4,5}$ edges of $\Theta = 0.004$ ML Dy on Ru(0001) ($T_{\text{dep}} = 4$ K, $T = 2.5$ K, (a,b) $B = 6.8$ T).

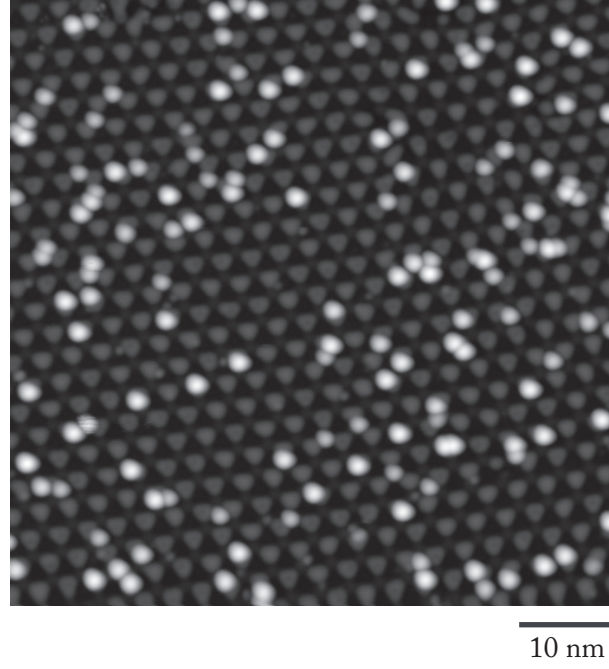


Figure 4.6 – STM image of $\Theta = 0.002$ ML Dy on graphene/Ru(0001) ($V_t = -0.2$ V, $I_t = 50$ pA; $T_{\text{dep}} = 10$ K, $T = 5$ K). Dy atoms appear as protrusions with different apparent heights depending on their adsorption site in the moiré cell.

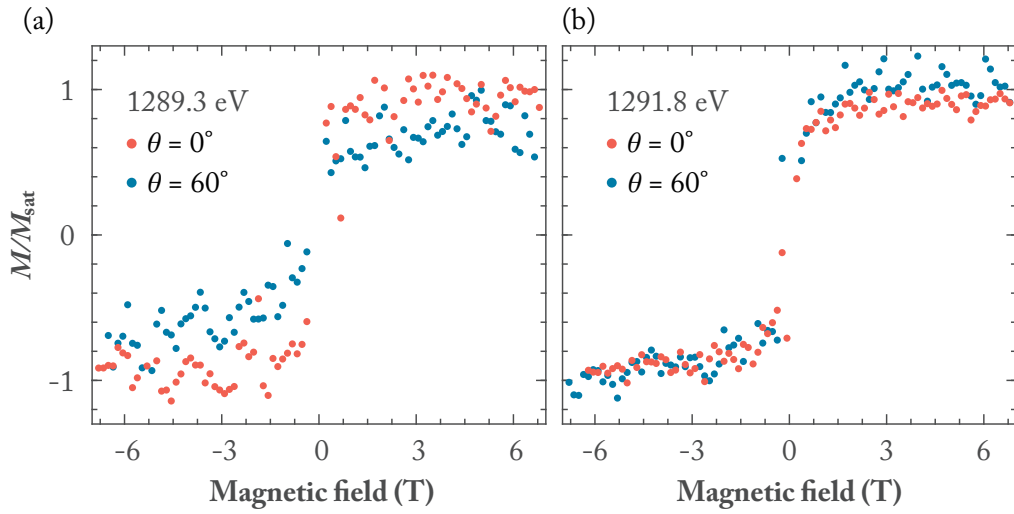


Figure 4.7 – Experimentally acquired magnetization curve for $\Theta = 0.004$ ML Dy on graphene/Ru(0001) at (a) 1289.3 eV and (b) 1291.8 eV ($T_{\text{dep}} = 4$ K, $T = 2.5$ K; $\phi = 9\phi_0$, $\dot{B} = 12$ mT s $^{-1}$). The magnetization curves were scaled with their respective ratios of XMCD intensities in the normal and grazing incidence of x-rays shown in Figure 4.5(b).

configuration is expected, just as for Dy atoms on bare metallic surfaces. Adsorption in weakly bound sites results in $4f^{10}$ configuration, just as for Dy atoms on graphene/Ir(111) and graphene/Cu. Since XAS and XMCD probe the average properties of an ensemble, we cannot distinguish between these two species and can only give the average of their magnetic properties.

Magnetization curves for both characteristic XMCD peaks of Dy atoms on graphene/Ru(0001) are shown in Figure 4.7. Due to the low intensity of the XMCD peaks at 1289.3 eV (Figure 4.5(b)), the resulting magnetization curves at this energy are very noisy (Figure 4.7(a)); however, it can be seen that both magnetization curve acquired in normal and in grazing incidence show a clear paramagnetic behavior. It must be noted that most of the signal at 1289.3 eV in fact originates from the tail of the peak at 1291.8 eV, hence the acquired magnetization curves do not entirely reflect the magnetic properties of divalent Dy atoms. Figure 4.7(b) shows magnetization curves acquired at 1291.8 eV. These curves also show paramagnetic behavior and short magnetization lifetime of trivalent Dy atoms on graphene/Ru(0001).

4.4 Dy on HOPG

4.4.1 Properties of HOPG

Highly oriented pyrolytic graphite (HOPG) is a form of synthetic graphite characterized by high purity and long range crystallographic order. It consists of stacked parallel graphene layers which are only weakly bound to each other by van der Waals forces. This results in their interplane distance of $d = 0.335$ nm [97]. The most stable and hence the most common stacking arrangement is ABA stacking [97] shown in Figure 4.8. Here, carbon atoms of A sublattice of the upper graphene layer are located directly above the carbon atoms B of layer below, whereas B atoms of the upper layer are placed above hollow sites of the lower layer.

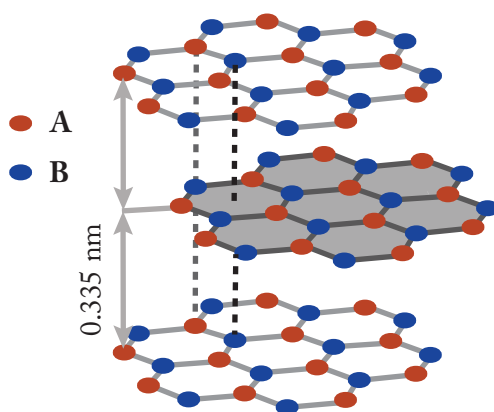


Figure 4.8 – ABA stacking of graphene layers in HOPG. Red balls mark carbon atoms of sublattice A and blue ones mark carbon atoms of sublattice B. Atoms A of the first layer are positioned above atoms B of the second layer, whereas atoms B of the first layer are positioned above hollow sites of second layer.

The cleaning of the HOPG surface can be done simply by exfoliation. This results in atomically flat surface which provides ideal, featureless background for deposited atoms. In addition to cleaving, which has been done in air, prior to deposition of Dy atoms on this surface, we annealed it to about $T = 870$ K, just as we did for the graphene/Cu substrates described in Section 4.2.1. The mounting of thin HOPG foils was the same as the one for graphene/Cu shown in Figure 4.2.

4.4.2 Magnetism of Dy atoms on HOPG

Experimentally acquired XAS, XMCD and XMLD spectra of single Dy atoms on HOPG are shown in Figure 4.9. Similar to all other spectra of Dy atoms on decoupling layers, these XAS and XMCD spectra are characterized by a prominent peak at 1289.3 eV showing a large amount of divalent Dy atoms on the HOPG surface. The low intensity peak at 1291.8 eV indicates the presence of a small abundance of trivalent Dy objects as well. Larger intensity of XMCD in normal with respect to grazing incidence (Figure 4.9(b)) reflects an out-of-plane easy axis of these atoms. Overall, all the acquired spectra resemble those for Dy atoms on Ir(111) shown in Figures 1.8 and 1.14, indicating a similar magnetic state of Dy atoms on HOPG and those on graphene/Ir(111).

To further characterize the magnetic properties of Dy atoms on HOPG, we acquired their magnetization curve. The magnetization curve acquired at 1289.3 eV in normal incidence of x-rays is shown in Figure 4.10(a). Similar to graphene/Ir(111), Dy atoms on HOPG show hysteresis with several characteristic steps associated with QTM. The magnetization curve is, however, closed at $B = 0$ T, *i.e.*, there is no magnetic remanence. Upon closer inspection of the positions of steps, it can be seen that three of them occur at the same magnetic field values as in the case of graphene/Ir(111). These are the steps at $B = 0$ T and $B = \pm 2.7$ T. The remaining two steps occur at lower field values, $B = \pm 4.4$ T, as compared to $B = \pm 5.6$ T in the case of graphene/Ir(111). Hence, we can conclude that the ground state of Dy atoms on HOPG is the same as in the case of graphene/Ir(111), $J_z = \pm 7$. However, the separation between its magnetic levels is not the same, which is caused by a small difference in the crystal fields generated by these two surfaces.

The levels which, along with $J_z = \pm 7$, participate in the crossings at $B = \pm 2.7$ T, are $J_z = \mp 8$. Since their crossings occur at the same magnetic field value for both Dy atoms on HOPG and graphene/Ir(111), the energy position of $J_z = \pm 8$ levels at $B = 0$ T is the same in these two cases, 3.1 meV. At $B = \pm 5.6$ T in the case of graphene/Ir(111) and $B = \pm 4.4$ T in the case of HOPG, levels $J_z = \pm 6$ and $J_z = \mp 7$ cross. Since these crossings occur at smaller fields for Dy atoms on HOPG, this implies that $J_z = \pm 6$ levels are at a lower energy in this case. Their energy is reduced from 5.6 meV in the case of graphene/Ir(111) to 4.1 meV in the case of HOPG. Figure 4.10(b) shows Zeeman diagram of these lowest lying Dy levels for the range of magnetic fields used in experiments. The lower position in energy of $J_z = \pm 6$ levels is also responsible for the lack of the magnetic remanence of Dy atoms on HOPG. The processes causing each

observed step in the hysteresis are addressed in detail in Section 3.5.

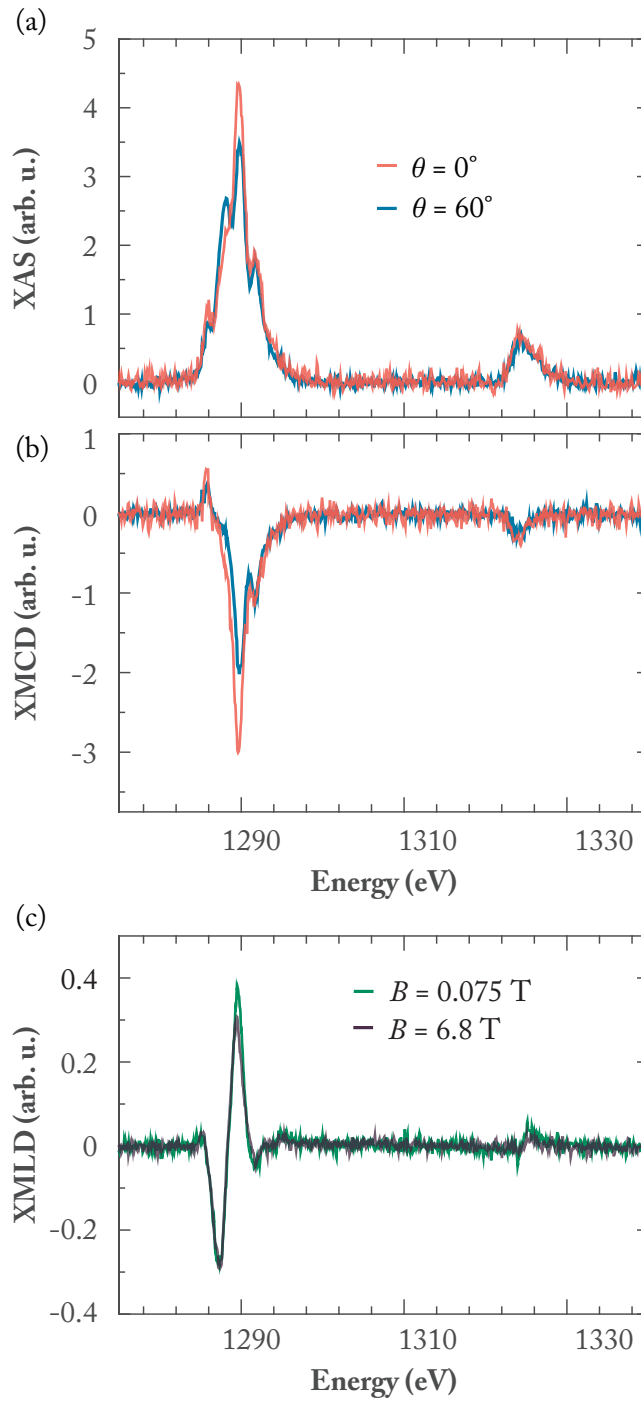


Figure 4.9 – Experimentally acquired XAS, XMCD and XMLD spectra at Dy $M_{4,5}$ edges of $\Theta = 0.005$ ML Dy on HOPG ($T_{\text{dep}} = 2.5$ K, $T = 2.5$ K, (a,b) $B = 6.8$ T).

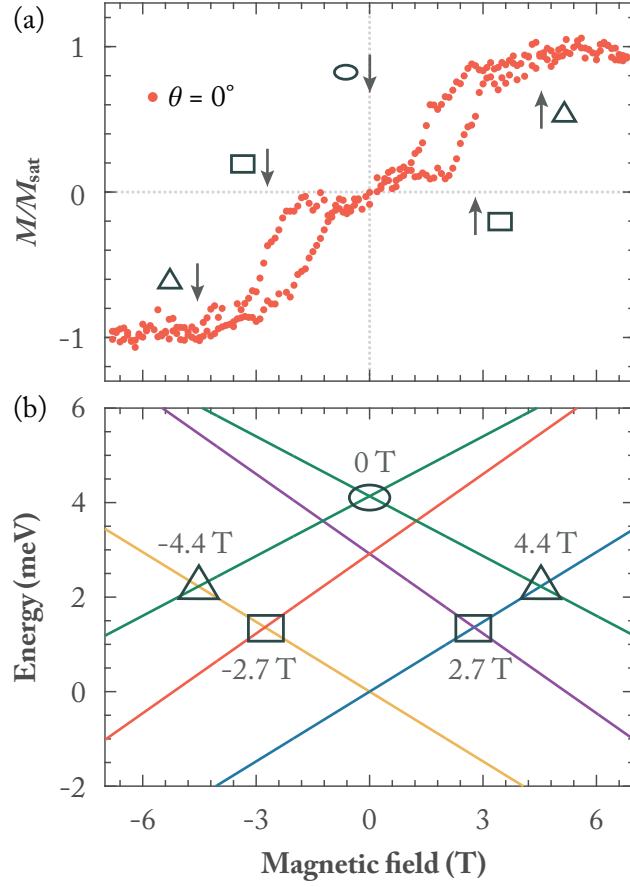


Figure 4.10 – (a) Experimentally acquired magnetization curve for $\Theta = 0.005$ ML Dy on HOPG at 1289.3 eV ($T_{\text{dep}} = 2.5$ K; $T = 2.5$ K; $\phi = 5\phi_0$, $\dot{B} = 33$ mT s $^{-1}$). (b) Zeeman diagram of the lowest lying Dy magnetic levels between -6.8 T and 6.8 T; yellow: $J_z = -7$, blue: $J_z = 7$, purple: $J_z = -8$, red: $J_z = 8$, and green: $J_z = \pm 6$. The triangles mark crossings of ± 7 and ∓ 6 levels at ± 4.4 T, rectangles mark crossings of ± 7 and ∓ 8 levels at ± 2.7 T, and ellipse marks crossing of ± 6 levels at 0 T.

4.4.3 Magnetic lifetime of Dy atoms on HOPG

Magnetic lifetime of Dy atoms on HOPG can be estimated by Arrhenius law describing the magnetization reversal:

$$\tau = \tau_0 \exp\left(\frac{U_{\text{rev}}}{k_B T}\right), \quad (4.1)$$

where τ is the magnetic lifetime of a system at temperature T , τ_0 is the characteristic time between two consecutive reversal attempts, k_B is the Boltzmann constant, and U_{rev} is the barrier for the magnetization reversal. Using the measured magnetic lifetime of Dy atoms on graphene/Ir(111) at 2.5 K, 971 s, and its barrier for magnetization reversal of 5.6 meV, we obtained $\tau_{0,\text{eff}} = 4.5 \times 10^{-9}$ s. Since the measured magnetic lifetime τ depends on the

experimental conditions, notably on the x-ray flux employed in measurements, the obtained value of $\tau_{0,\text{eff}}$ represents a lower bound for the intrinsic τ_0 . This value is comparable to the ones obtained for the Fe_4 molecular magnets adsorbed on a metal surface [29] and on graphene [82]. Assuming that τ_0 is primarily dependent on the properties of the substrate and particularly of its phonons, we can use the value obtained for Dy on graphene/Ir(111) to estimate the magnetic lifetime of these atoms on HOPG. The obtained value is $\tau = 1$ s. This lifetime is shorter than the time needed for the acquisition of a single point in our magnetization curves and hence we do not observe any remanence in the acquired magnetization curve (Figure 4.10(a)).

4.5 Dy on *h*-BN/Ir(111)

4.5.1 Properties of *h*-BN

Hexagonal boron nitride (*h*-BN) is a two-dimensional material consisting of boron and nitrogen atoms arranged in a honeycomb structure. It is isostructural to graphene, with a lattice constant of $a_{0,h\text{-BN}} = 2.48 \text{ \AA}$ [53]. However, unlike graphene, *h*-BN is a wide bandgap insulator, with gap of about 6 eV [98].

When *h*-BN is grown on metallic substrates, due to their lattice mismatch, a moiré superstructure is formed [53, 99, 100]. It consists of two distinct regions, *pores* where *h*-BN is strongly bound, and *wires* where it is only weakly bound to its substrate. Strong bonds form in regions where centers of the *h*-BN's rings are situated on top of the fcc hollow sites of the surface. Weak bonds occur for these centers being on top of atoms of the metallic substrate [101].

The exact properties of the moiré superstructure depend on the substrate upon which *h*-BN is grown. For *h*-BN grown on Ir(111), the resulting moiré superstructure has periodicity of about 2.9 nm [101]. Its pores are at $d_p = 2.95 \text{ \AA}$, and wires are at $d_w = 3.30 \text{ \AA}$ above the iridium surface, resulting in a weak corrugation of only 0.35 Å [101]. A stronger interaction of *h*-BN with the substrate results in a larger corrugation. For instance, in the case of *h*-BN grown on Ru(0001), their minimal separation is much smaller, only 2.0 nm, and the corrugation of the *h*-BN layer is much larger, and its amounts to approximately 1.5 Å [100].

4.5.2 Magnetism of Dy atoms on *h*-BN/Ir(111)

To investigate whether it is possible to stabilize magnetic moments of Dy atoms in a lower crystal field symmetry with respect to graphene, but with large screening from the electrons of the substrate, we investigated their magnetic properties on *h*-BN. Adsorption of Dy atoms on this substrate imposes C_{3v} crystal field symmetry to their magnetic levels, and offers strong decoupling from the metallic substrate with the wide band gap of *h*-BN.

The experimentally acquired XAS, XMCD and XMLD spectra for $\Theta = 0.007$ ML of Dy on *h*-BN/Ir(111) are shown in Figure 4.11(a-c). The XAS and XMCD spectra reveal predominantly

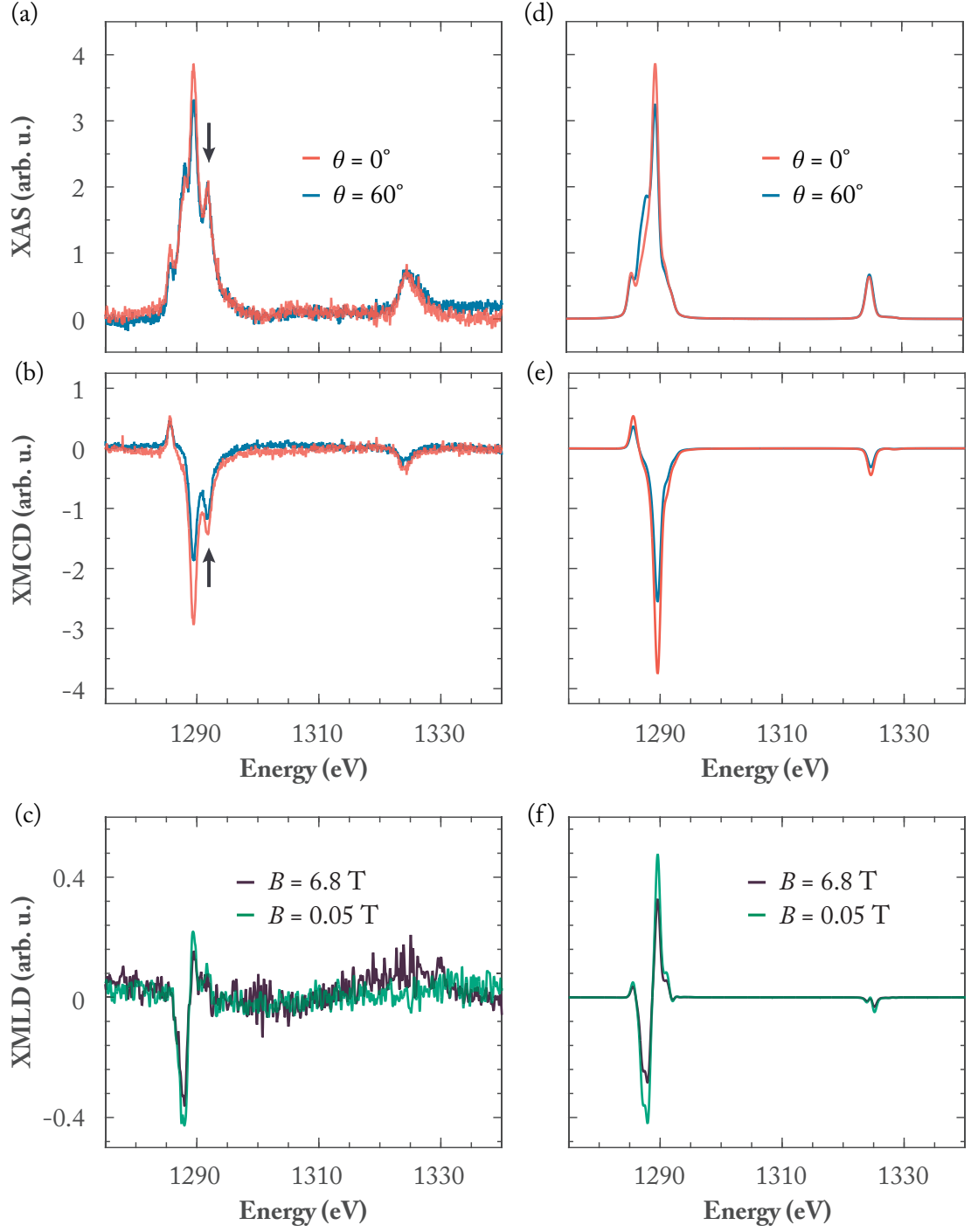


Figure 4.11 – (a-c) Experimentally acquired XAS, XMCD and XMLD spectra of $\Theta = 0.007$ ML Dy on *h*-BN ($T_{\text{dep}} = 4$ K, $T = 2.5$ K, (a,b) $B = 6.8$ T). The arrows point to the peaks at 1291.8 eV. (d-e) XAS, XMCD and XMLD spectra at the $M_{4,5}$ Dy edges resulting from multiplet calculations for Dy atoms in the C_{3v} CF of *h*-BN.

Dy atoms with $4f^{10}$ electronic occupation on the surface. A small number of objects with $4f^9$ occupation is also present, as can be deduced from the presence of the peak at 1291.8 eV in the acquired spectra. The larger intensity of the XMCD in normal with respect to the grazing incidence of x-rays indicates an out-of-plane easy magnetization axis for these atoms. Figure 4.12 shows magnetization curves acquired for Dy atoms on *h*-BN/Ir(111). On this surface, Dy atoms show paramagnetic behavior.

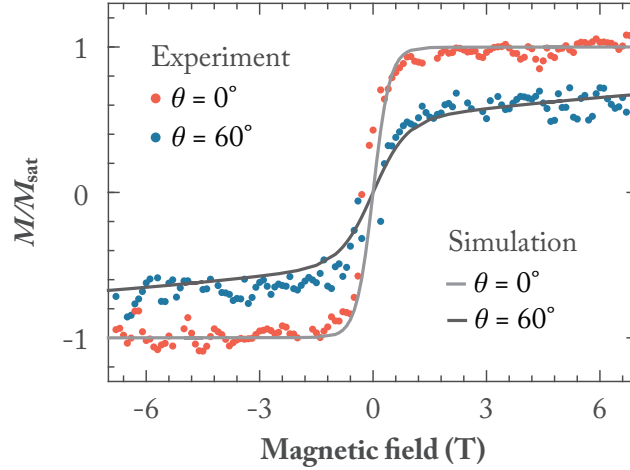


Figure 4.12 – Experimentally acquired magnetization curves of $\Theta = 0.007$ ML Dy on *h*-BN/Ir(111) at 1289.3 eV ($T_{\text{dep}} = 4$ K, $T = 2.5$ K; $\phi = 9\phi_0$, $\dot{B} = 12$ mT s $^{-1}$) shown together with their simulated counterparts.

We performed multiplet calculations to determine the ground state and energy diagram of Dy atoms on *h*-BN/Ir(111). The C_{3v} point charge crystal field used to reproduce the experimental spectra and magnetization curves is shown in Figure 4.13. It consists of alternating positive and negative charges on the positions of boron and nitrogen of the *h*-BN/Ir(111) hexagonal ring, respectively, surrounding the Dy atom adsorbed in the hollow site. Below Dy, there is an additional positive charge. The exact geometry of this crystal field is given in the Appendix A. The resulting simulations are shown together with their experimental counterparts in Figure 4.11 and 4.12.

The simulated spectra show good agreement with the experimental ones. The main difference in the XAS and XMCD spectra are peaks at 1291.8 eV, observed in the experimental and absent in the simulated spectra. As mentioned before, the source of these peaks are contaminated or bigger Dy objects present at the surface, which are not included in our simulations. In the case of XMLD, we focused on reproducing the larger intensity of the spectrum at $B = 0.05$ T, as compared to the one at $B = 6.8$ T. The experimental magnetization curves are also well reproduced by our simulations.

As anticipated from the experimental spectra, the multiplet calculations reveal $4f^{10}$ occupation of Dy atoms on *h*-BN/Ir(111), with a lowest $J = 8$ multiplet and a ground state doublet $\langle J_z \rangle = \pm 6.8$. The resulting energy diagram is shown in Figure 4.14. Three different colors in

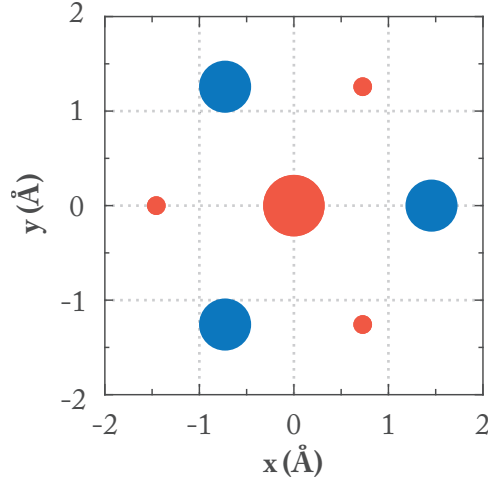


Figure 4.13 – Point charge crystal field employed in the multiplet calculations for Dy on *h*-BN/Ir(111). Positive charges are marked with red, and negative with blue. The size of each circle reflects the charge value. The exact geometry and strength of depicted charges are given in Appendix A.

this diagram depict three classes of eigenstates created by the three-fold symmetric crystal field of *h*-BN/Ir(111) surface.

The lack of the magnetic stability in Dy atoms at $B = 0$ T can be ascribed to the presence of a tunnel split doublet with $J_z = \pm 6$ at 4 meV above the ground state. The tunnel splitting

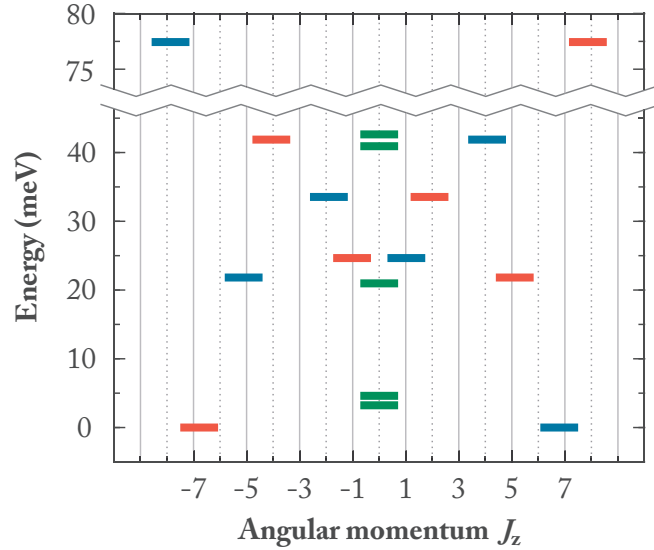


Figure 4.14 – The zero field splitting of the Dy lowest multiplet ($J = 8$) resulting from multiplet calculations. Each color identifies magnetic quantum states belonging to one of the three classes of eigenstates defined by the C_{3v} group symmetry. $J_z = \pm 6$ form a tunnel split doublet at 4 meV, and $J_z = \pm 3$ form the one at 41 meV.

between these two levels amounts to $\Delta_{-6,6} = 0.42$ meV. Thermal excitation to this state leads to the QTM and results in magnetization relaxation on a time scale of seconds, just as in the case of Dy atoms on HOPG. The coupling of levels in C_{3v} symmetry is also responsible for the lack of a magnetic bistability in the presence of magnetic field. Since this symmetry couples J_z levels that differ by $\Delta J_z = \pm 3$, only a single scattering event is necessary for transition between the $J_z = \pm 6.8$ states and a consequential relaxation of magnetization.

5 Magnetism of Nd, Ho, Er and Tb on graphene/Ir(111)

In this chapter we extend the study of the magnetic properties and electronic configuration of lanthanide atoms on graphene/Ir(111) to four more elements: Nd, Tb, Ho and Er. The results of our combined XMCD and multiplet calculations studies for Nd atoms are given in Section 5.1, for Ho atoms in Section 5.2, for Er atoms in Section 5.3 and for Tb atoms in Section 5.4. In section 5.5, the underlying interactions that lead to the predominantly divalent electronic configuration of lanthanide atoms on graphene/Ir(111) are discussed. In Sections 5.6 and 5.7 we evaluate the magnetic stability of lanthanide atoms based on their ground state and energy level diagram. In addition, we give an estimate of their magnetic lifetimes. The sensitivity of divalent lanthanide atoms to contamination is presented in detail in Section 5.8. Finally, in Section 5.9 a discussion on the validity of sum rules in the case of lanthanide atoms is given, as well as their comparison with multiplet calculations.

For the results presented in this chapter, a manuscript is in preparation: R. Baltic, *et al.*, Magnetic properties of single rare earth atoms on graphene/Ir(111).

Work contribution. *As part of a team led by Dr. Stefano Rusponi, I contributed to all XMCD measurements presented in this Chapter. I carried out the data analysis and multiplet calculations. The multiplet calculations were performed under the supervision of Dr. Fabio Donati.*

5.1 Nd on graphene/Ir(111)

In their divalent configurations, neodymium (Nd) atoms have 10 holes, whereas Dy atoms have 10 electrons in their $4f$ orbitals. This results in the same S and L values in these two cases; however due to the opposite spin-orbit coupling in early and late lanthanides, the resulting J values are different. To investigate magnetic properties of Nd atoms on graphene/Ir(111), we deposited minute amounts of Nd on freshly prepared graphene/Ir(111) surface and acquired their XAS, XMCD and XMLD spectra at Nd $M_{4,5}$ edges. The acquired spectra are shown in Figure 5.1(a-c).

In all acquired spectra, there are pronounced spectral features at both Nd M_4 and M_5 edges.

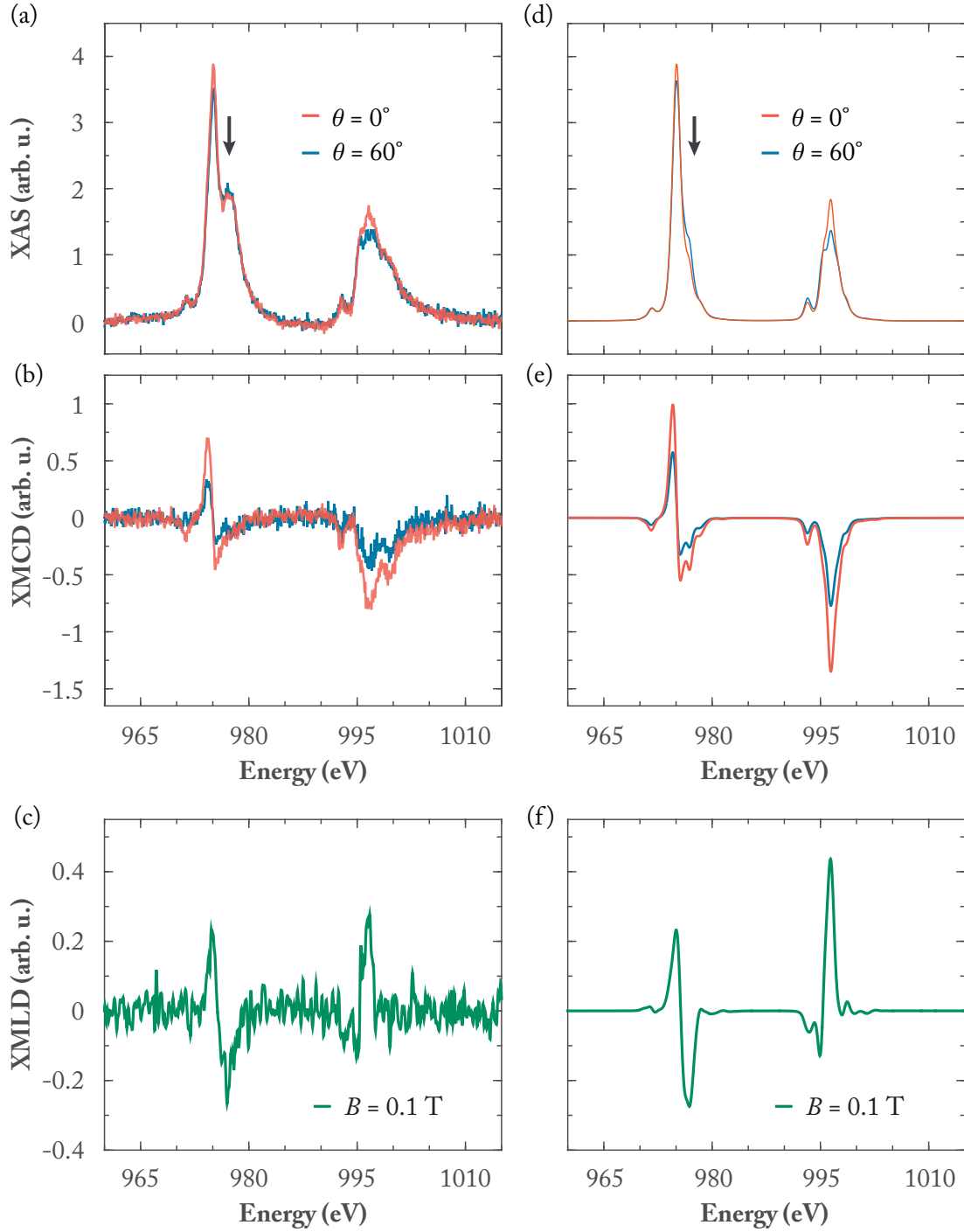


Figure 5.1 – (a-c) Experimentally acquired XAS, XMCD and XMLD spectra of $\Theta = 0.002$ ML Nd on graphene/Ir(111) ($T_{\text{dep}} = 4$ K, $T = 2.5$ K, (a,b) $B = 6.8$ T). The arrows point to the peaks at 977.3 eV. (d-f) XAS, XMCD and XMLD spectra at the $M_{4,5}$ Nd edges resulting from multiplet calculations for Nd atoms in the C_{6v} CF of graphene/Ir(111) surface.

In XMCD spectra, these features have opposite sign, with the M_5 edge being positive and the M_4 edge negative (Figure 5.1(b)). The higher intensity of the XMCD signal in normal with respect to grazing incidence of x-rays indicates an out-of-plane easy magnetization axis of this system.

Since spectral features of the M_4 edge have higher intensity than those of the M_5 edge, we acquired magnetization curves of Nd atoms at the M_4 edge. We recorded the magnetic field dependence of the peak at 996.7 eV for both normal and grazing incidence and the resulting magnetization curves are shown in Figure 5.2. Both curves show paramagnetic behavior at the acquisition temperature of $T = 2.5$ K. The magnetization curve recorded in normal incidence is much steeper for magnetic field values around $B = 0$ T and saturates for $B \geq |4|$ T, whereas magnetization curve in grazing incidence saturates only for the highest available fields. This is a clear evidence of an out-of-plane anisotropy of Nd atoms on graphene/Ir(111).

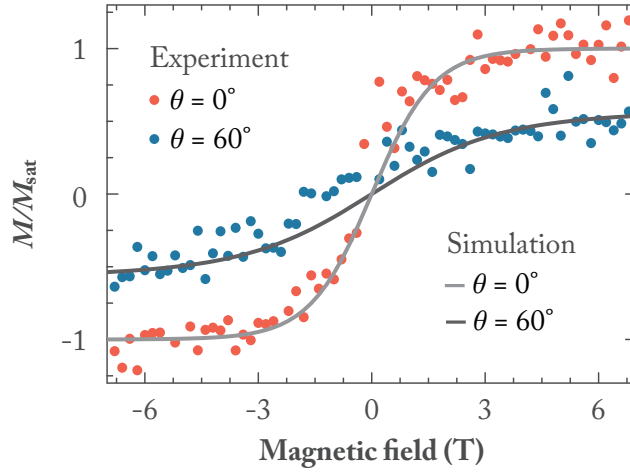


Figure 5.2 – Experimentally acquired magnetization curves for $\Theta = 0.002$ ML Nd on graphene/Ir(111) ($T = 2.5$ K, $\phi = 9\phi_0$, with $\phi_0 = 0.003$ photons $\text{nm}^{-2} \text{s}^{-1}$, and $\dot{B} = 12$ mT s^{-1}), shown together with magnetization curves resulting from multiplet calculations for Nd atoms in the C_{6v} CF of graphene/Ir(111) surface. Experimental magnetization curves were acquired by measuring the XMCD signal at 996.7 eV as a function of the magnetic field.

To gain further insight into the electronic structure and magnetic ground state of Nd atoms on graphene/Ir(111), we performed multiplet calculations for this system. The main focus in multiplet calculations was on reproducing three key features that characterize the energy diagram of this system. These are the spectral features of the XAS, XMCD and XMLD spectra, the overall shape of the magnetization curves (Figure 5.2), and the ratio of intensities of the XMCD peaks in normal and grazing incidence at $B = 6.8$ T (Figure 5.1(b)). This ratio sets the relative amplitude of the corresponding magnetization curves at the same field and it amounts to approximately $1/2$. This means that the XMCD intensity rescales as the cosine of the x-ray incidence angle θ , indicating a maximal J_z as a magnetic ground state and a large splitting of the magnetic levels.

Multiplet calculations were performed using the point charge crystal field scheme shown in Figure 5.3. It consists of six negative charges placed at the positions of the carbon atoms of a hexagonal ring, with the Nd atom adsorbed in their center. The exact geometry and strength of employed point charges are given in Appendix A. The resulting XAS, XMCD and XMLD spectra, as well as magnetization curves are shown with their experimental counterparts in Figures 5.1 and 5.2.

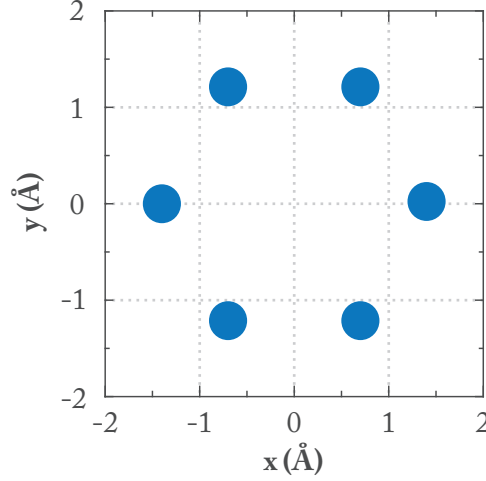


Figure 5.3 – Point charge crystal field employed in the multiplet calculations for Nd atoms on graphene/Ir(111). Blue color represents the negative charge. The exact geometry and strength of depicted charges are given in Appendix A.

The simulated spectra reproduce well all the spectral features observed in the experiments, apart from the peak at 977.3 eV. Similarly to what was observed for Dy atoms on graphene/Ir(111), this disagreement can be attributed to clusters and/or contaminated Nd atoms. Since these objects provide only a minor contribution to the average properties of an ensemble consisting primarily of Nd atoms, they will not be considered in the further discussion. The sensitivity of Nd atoms to contamination will be addressed in detail in Section 5.8.

Multiplet calculations reveal a divalent $4f^4$ occupation for Nd atoms on graphene/Ir(111), and a lowest multiplet with $J = 4$. Similar occupation of nearly 4 electrons in their $4f$ orbitals has been calculated by DFT for Nd atoms on freestanding graphene [102]. The energy diagram for Nd atoms at $B = 0$ T, resulting from multiplet calculations, is shown in Figure 5.4.

The adsorption of Nd atoms in the hollow site of graphene results in a strong uniaxial anisotropy with nearly maximal magnetic ground state of $J_z = \pm 3.8$, as anticipated from the ratio of XMCD intensities at $B = 6.8$ T. The total zero field splitting of this system is approximately 16 meV; nevertheless, it is greatly reduced by the $J_z = \pm 3$ levels that provide a shortcut for the thermally activated magnetization relaxation. These levels are strongly mixed and tunnel-split in the C_{6v} crystal field symmetry of graphene, forming a doublet of quenched $\langle J_z \rangle$. The separation between two levels in this doublet is $\Delta_{-3,3} = 5.9$ meV, and the lower of the two is at the energy of 3.2 meV. This large separation provides a substantially larger QTM rate in

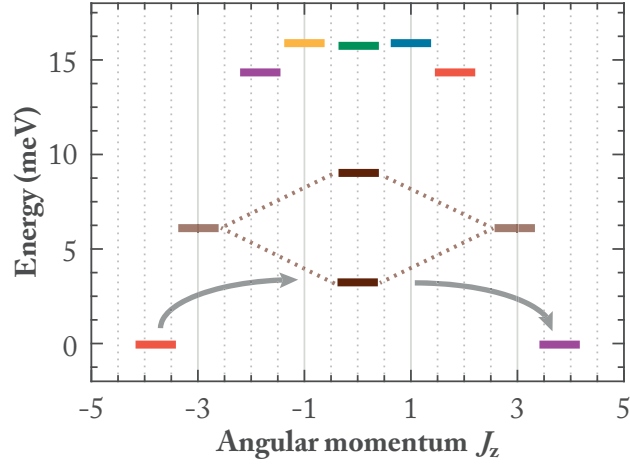


Figure 5.4 – The zero field splitting of the Nd lowest multiplet ($J = 4$) resulting from multiplet calculations. Each color identifies magnetic quantum states belonging to one of the six classes of eigenstates defined by the C_{6v} symmetry. The dashed lines illustrate the formation of a tunnel split doublet by $J_z = \pm 3$ states. Grey arrows indicate the relaxation mechanism at $B = 0$ T via thermal excitation to $J_z = \pm 3$ doublet.

the case of Nd with respect to the Dy case, where the separation between the tunnel split $J_z = \pm 6$ levels is more than four orders of magnitude smaller [103]. Hence, this tunnel-split doublet strongly reduces the barrier for magnetization reversal and is responsible for the lack of magnetic remanence at $B = 0$ T in Nd atoms (Figure 5.2). The thermally activated shortcut for magnetization reversal provided by this tunnel-split levels is indicated with grey arrows in Figure 5.4.

5.2 Ho on graphene/Ir(111)

Holmium (Ho) atoms are the following lanthanide atoms whose magnetic properties we investigated on graphene/Ir(111). We deposited $\Theta = 0.003$ ML of Ho on a newly prepared substrate, ensuring predominantly single Ho atoms on the surface. Subsequently, we acquired their XAS, XMCD and XMLD spectra at Ho $M_{4,5}$ edges. The resulting spectra are shown in Figure 5.5(a-c).

The acquired spectra is characterized by pronounced features of the M_5 edge and low intensity features of the M_4 edge, which are, in the case of XMLD spectra, hidden in the noise (Figure 5.5(c)). Holmium atoms on graphene/Ir(111) show slight in-plane anisotropy, as can be inferred from the slightly larger intensity of the XMCD signal acquired for grazing, as compared to normal incidence of x-rays (Figure 5.5(b)).

To further characterize the magnetic properties of Ho atoms, we acquired their magnetization curves at the M_5 edge, at its peak with the highest intensity occurring at 1346.6 eV. The resulting magnetization curves are shown in Figure 5.6. Both normal and grazing magnetization curves

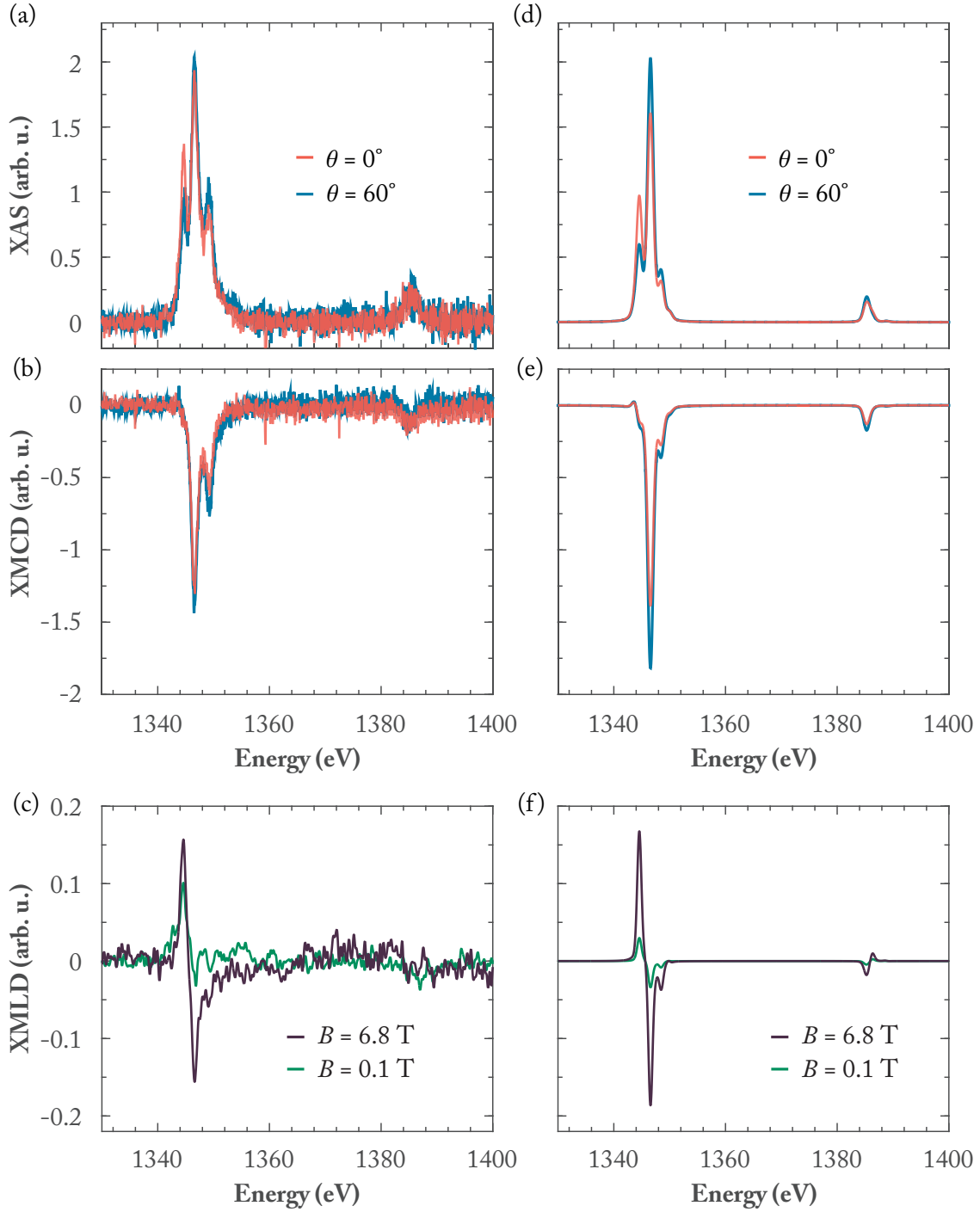


Figure 5.5 – (a-c) Experimentally acquired XAS, XMCD and XMLD spectra of $\Theta = 0.003$ ML Ho on graphene/Ir(111) ($T_{\text{dep}} = 4$ K, $T = 2.5$ K, (a,b) $B = 6.8$ T). (d-f) XAS, XMCD and XMLD spectra at the $M_{4,5}$ Ho edges resulting from multiplet calculations for Ho atoms in the C_{6v} CF of graphene/Ir(111) surface.

show paramagnetic behavior. The normal magnetization curve is steeper for magnetic fields around $B = 0$ T and saturates already at about $B = 2$ T. However, the grazing curve crosses it at $B = 3$ T, and it does not saturate even for the highest available magnetic field of $B = 6.8$ T. This indicates a larger magnetic moment of Ho atoms in in-plane with respect to out-of-plane direction at fields larger than $B = 3$ T and demonstrates an in-plane anisotropy of this system. Further, it suggests a ground state with an intermediate J_z value which can produce large projected magnetic moments along both incidence directions.

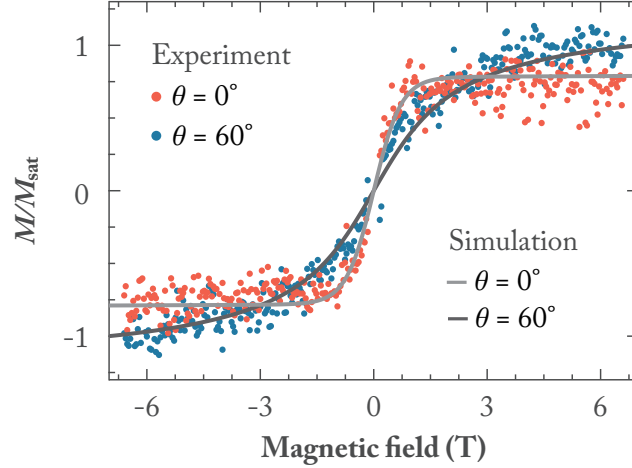


Figure 5.6 – Experimentally acquired magnetization curves for $\Theta = 0.003$ ML Ho on graphene/Ir(111) ($T = 2.5$ K, $\phi = 9\phi_0$ and $\dot{B} = 12$ mT s $^{-1}$), shown together with magnetization curves resulting from multiplet calculations for these atoms in the C_{6v} CF of graphene/Ir(111) surface. Experimental magnetization curves were acquired by measuring the XMCD signal at 1346.6 eV as a function of the magnetic field.

To determine the electronic structure and magnetic ground state of Ho atoms on graphene/Ir(111), we performed multiplet calculations. We focused on reproducing the Ho spectral features shown in Figure 5.5(a-c), with an emphasis on reproducing the distinctive behavior of its XMLD spectra. Unlike for the other studied lanthanide atoms, the intensity of XMLD in the case of Ho atoms increases with increasing magnetic field. An additional feature that unambiguously determines the ground state of these atoms is the crossing of its normal and grazing magnetization curve at $B = 3$ T. Reproducing these features required the use of a more complex point charge crystal field scheme, whose planar representation is shown in Figure 5.7. It consists of alternating positive and negative charges placed at the vertices of two hexagons rotationally displaced by 30° . In addition, there is a small positive charge in the middle of these hexagonal rings, below the adsorbed Ho atom. The exact geometry and strength of employed point charges are given in Appendix A.

The XAS, XMCD and XMLD spectra, as well as the magnetization curves resulting from multiplet calculations are shown together with their experimental counterparts in Figures 5.5 and 5.6. They reproduce experimental spectra well. In particular, we reproduced the increase in the XMLD intensity with the magnetic field, and the crossing of normal and grazing

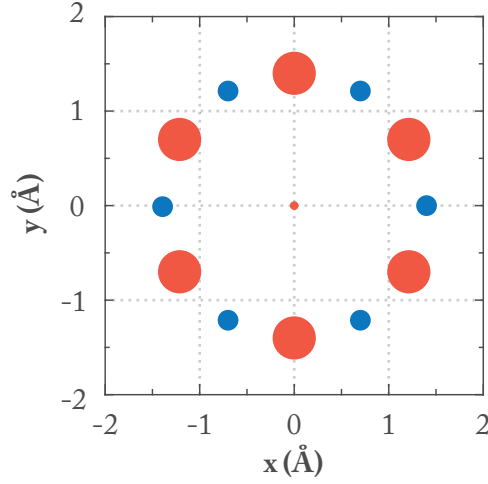


Figure 5.7 – Planar representation of the point charge crystal field employed in the multiplet calculations for Ho on graphene/Ir(111). Positive charges are marked with red, and negative with blue. The size of each circle reflects the charge value. The exact geometry and strength of depicted charges are given in Appendix A.

magnetization curve at $B = 3$ T.

Our simulations reveal 11 electrons in Ho $4f$ orbitals, a lowest multiplet with $J = 15/2$ and a total zero field splitting of 23 meV. The resulting energy diagram is shown in Figure 5.8. The ground state doublet of this system has $\langle J_z \rangle = \pm 4.3$, which is very close to the pure $J_z = \pm 9/2$ levels. The distinctive behavior of XMLD spectra is unique to it, and it could not be reproduced with any other J_z level as a potential ground state in our calculations. This ground state

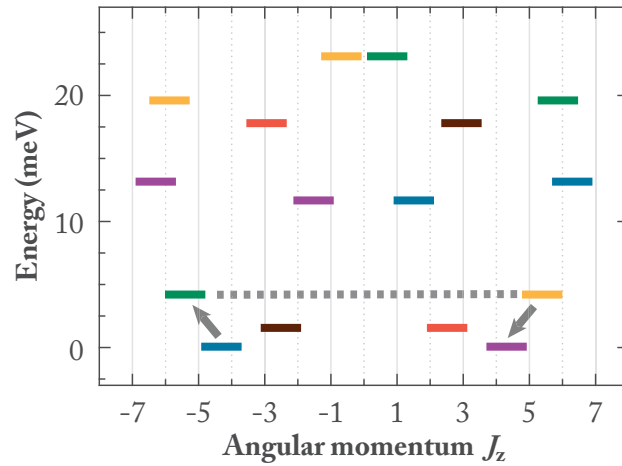


Figure 5.8 – The zero field splitting of the Ho lowest multiplet ($J = 15/2$) resulting from multiplet calculations. Each color identifies magnetic quantum states belonging to one of the six classes of eigenstates defined by the C_{6v} symmetry. Grey arrows indicate magnetization relaxation mechanism at $B = 0$ T via thermal excitation to $\langle J_z \rangle = \pm 5.4$.

should, in principle, result in a stable magnetization of this system; nevertheless, the absence of hysteresis in magnetization curves (see Figure 5.6) indicates magnetic lifetime in order of seconds or less at 2.5 K.

Given the large total zero field splitting of 23 meV, thermally activated processes overcoming the full barrier to reverse the magnetization must be excluded. Therefore, this relaxation has to occur via assisted QTM involving nearest excited states. At $B = 0$ T, the lowest lying excited states are $J_z = \pm 5/2$ at 1.6 meV, which cannot be reached by first order transitions. Hence, the lowest lying levels that participate in scattering processes with $\Delta J_z = \pm 1$ are $\langle J_z \rangle = \pm 5.4$ (close to pure $J_z = \pm 11/2$) at 4.2 meV. The transition from ground to these excited states and vice versa is marked by solid-line arrows in Figure 5.8. This excited doublet is non-axial in the C_{6v} symmetry [27] and offers a path for assisted QTM, as indicated by dashed lines in Figure 5.8.

5.3 Er on graphene/Ir(111)

We deposited minute amount of erbium (Er) on newly prepared graphene/Ir(111). Subsequently, we acquired their XAS, XMCD and XMLD spectra and the resulting spectra are shown in Figure 5.9(a-c). The spectra of Er atoms are characterized by the pronounced multiplet features at the M_5 edge, whereas the features of its M_4 edge are hidden in the noise. Considerably larger intensity of XMCD spectra in grazing with respect to the normal incidence of x-rays (Figure 5.9(b)) indicates strong in-plane anisotropy of Er atoms on this substrate, and implies a low J_z ground state of the system.

In the case of Er atoms on graphene/Ir(111), their high sensitivity to contamination has hindered the acquisition of the magnetization curves. The magnetization curves we acquired do not accurately reflect the magnetic state of Er atoms, as it will be discussed in more detail in Section 5.8. The lack of magnetization curves in the full data set prevents the fine data adjustments in simulations and therefore limits the precision of the inferred energy level splitting from the multiplet calculations. Nevertheless, we performed calculations focusing on reproducing the overall spectral shape of XAS, XMCD and XMLD. In particular, we aimed to reproduce the in-plane anisotropy of this system with the adequate ratio of XMCD peaks in normal and grazing incidence at 6.8 T (Figure 5.9(b)), and higher intensity of XMLD spectra at $B = 0.1$ T, compared to $B = 6.8$ T. To reproduce these features, we employed the point charge crystal field scheme, whose planar representation is shown in Figure 5.10. Similarly to the scheme employed in the case of Ho, it consists of alternating positive and negative charges placed at the vertices of two hexagons rotationally displaced by 30° . However, in this case, there is a large negative charge in the center of the hexagonal rings, below the adsorbed Er atom. The exact geometry and strength of employed point charges are given in Appendix A.

The spectra resulting from multiplet calculations are shown in Figure 5.9(d-f). They reproduce well all the spectral features observed in experiments, apart from the peaks at 1405.6 eV in both XAS and XMCD spectra (see Figure 5.9(a,b)). These peaks have much higher intensity in experimental spectra and can be attributed to Er dimers and contaminated atoms on the

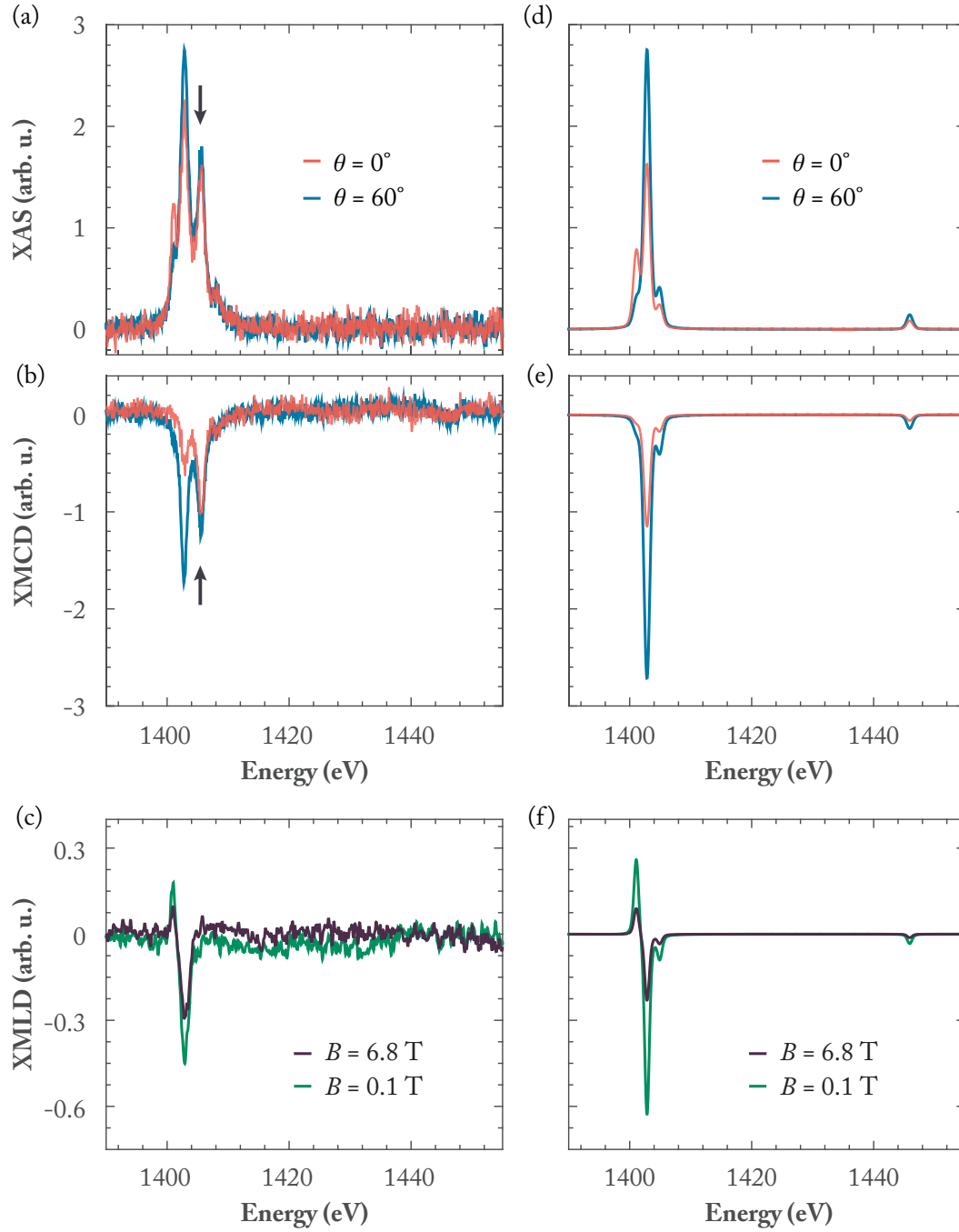


Figure 5.9 – (a-c) Experimentally acquired XAS, XMCD and XMLD spectra of $\Theta = 0.004$ ML Er on graphene/Ir(111) ($T_{\text{dep}} = 4$ K, $T = 2.5$ K, (a,b) $B = 6.8$ T). The arrows point to the peaks at 977.3 eV. (d-f) XAS, XMCD and XMLD spectra at the $M_{4,5}$ Er edges resulting from multiplet calculations for Er atoms in the C_{6v} CF of graphene/Ir(111) surface. The arrows in (a,b) point to the peak at 1405.6 eV, whose large intensity originates from contaminated Er atoms and bigger Er objects.

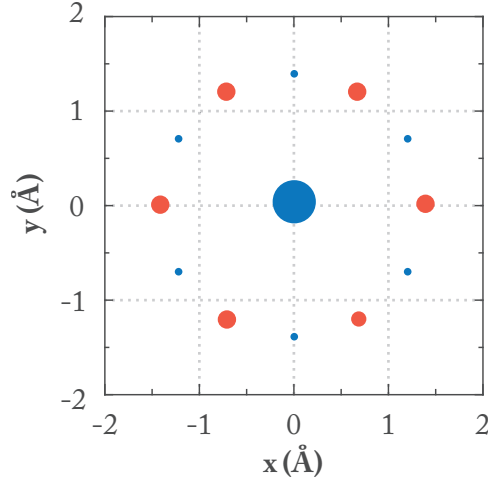


Figure 5.10 – Planar representation of the point charge crystal field employed in the multiplet calculations for Er on graphene/Ir(111). Positive charges are marked with red, and negative with blue. The size of each circle reflects the charge value. The exact geometry and strength of depicted charges are given in Appendix A.

graphene/Ir(111) surface. Our simulations do not take into account these objects and hence their features are not reproduced.

Our calculations reveal divalent $4f^{12}$ occupation of Er atoms on graphene/Ir(111) and a lowest multiplet with $J = 6$. The resulting energy diagram is shown in Figure 5.11. The total zero field splitting of this system is 15 meV and its ground state doublet is $J_z = \pm 2$. In addition, there are several levels with $J_z \leq 3$ within less than 1 meV, with the tunnel-split $J_z = \pm 3$ levels lying at

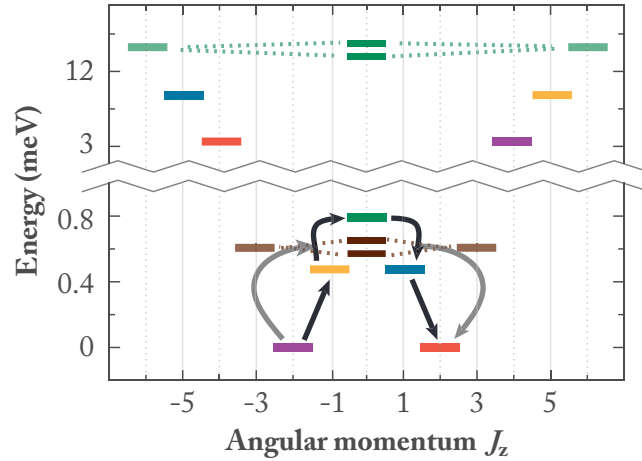


Figure 5.11 – The zero field splitting of the Er lowest multiplet ($J = 6$) resulting from multiplet calculations. Each color identifies magnetic quantum states belonging to one of the six classes of eigenstates defined by the C_{6v} symmetry. Dashed lines connect doublets with quenched $\langle J_z \rangle$. Grey and black arrows indicate two magnetization relaxation mechanisms at $B = 0$ T.

0.6 meV above the ground state doublet.

The very small separation between lowest lying levels facilitates magnetization reversal through scattering with electrons and phonons of the substrate and no stable magnetization is expected for this system. At $B = 0$ T, there are two main magnetization reversal paths. For one, the relaxation occurs via thermal excitation to the tunnel-split $J_z = \pm 3$ states at 0.6 meV, as indicated by the grey arrows in Figure 5.11. For the other, the relaxation path consists of thermal excitation to $J_z = 0$ via the $J_z = \pm 1$ states, as it is indicated by the black arrows in Figure 5.11.

5.4 Tb on graphene/Ir(111)

The final lanthanide atom whose magnetic properties on graphene/Ir(111) we studied is terbium (Tb). We deposited $\theta = 0.003$ ML of Tb on a freshly prepared graphene/Ir(111) surface, thus ensuring an ensemble of predominantly single and non interacting atoms on this surface. Their experimentally acquired XAS, XMCD and XMLD spectra are shown in Figure 5.12.

Unlike for the other lanthanide atoms, the XAS spectral features of Tb atoms indicate their trivalent configuration on the graphene/Ir(111) surface. This $4f^8$ configuration is characterized by a double-peak structure in the Tb M_5 edge [32, 35]. The XMCD spectra of Tb atoms are characterized by the pronounced features at the M_5 edge. The higher intensity of the XMCD signal acquired in grazing with respect to normal incidence of x-rays (Figure 5.12(b)) indicates an in-plane anisotropy for this system.

To further characterize the magnetic properties of Tb atoms on graphene/Ir(111), we acquired their magnetization curves. The resulting curves for both normal and grazing incidence of x-rays are shown in Figure 5.13. Both acquired curves show paramagnetic behavior at $T = 2.5$ K. The magnetization curve acquired in grazing incidence shows steeper behavior for magnetic fields around $B = 0$ T, and a larger intensity throughout the entire range of employed magnetic field values. This indicates larger magnetic moment of Tb atoms in the in-plane direction and hence an in-plane anisotropy of this system.

We performed multiplet calculations to determine the electronic and quantum level structure of Tb atoms on graphene/Ir(111). The main objective in these calculations was to reproduce the in-plane anisotropy of this system with an appropriate ratio of XMCD intensities for two incidences of x-rays at $B = 6.8$ T (Figure 5.12(b)). In addition, we focused on reproducing the shape of XAS spectra for $\theta = 0^\circ$. All these features characterize the ground state and the energy diagram of this system.

Multiplet calculations were performed using the point charge crystal field scheme, whose planar representation is shown in Figure 5.14. This scheme consists of six positive charges placed at positions of carbon atoms in a hexagonal ring of graphene, and a smaller negative charge in its center. Just as with other lanthanides on graphene/Ir(111), we performed simula-

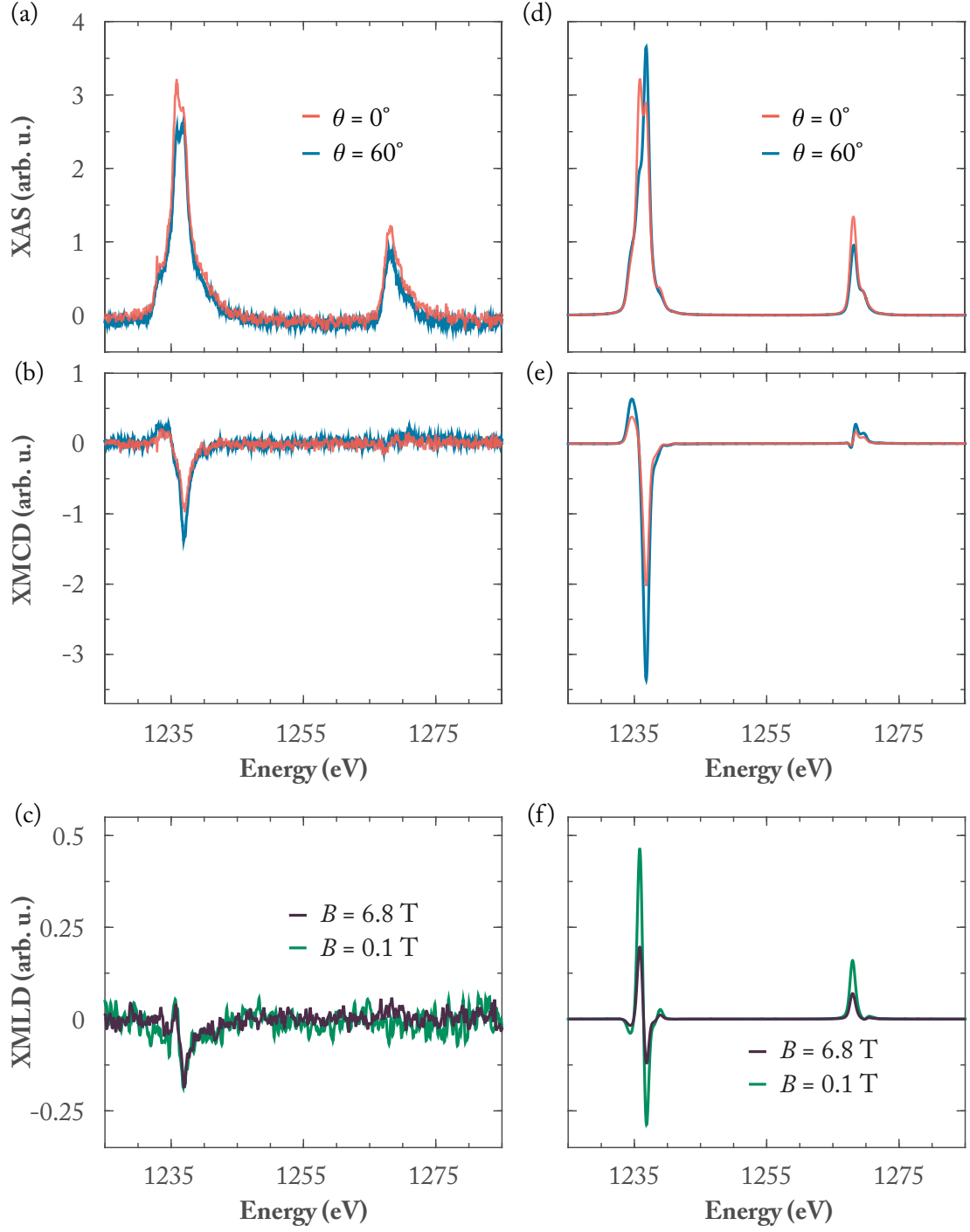


Figure 5.12 – (a-c) Experimentally acquired XAS, XMCD and XMLD spectra of $\Theta = 0.003$ ML Tb on graphene/Ir(111) ($T_{\text{dep}} = 4$ K, $T = 2.5$ K, (a,b) $B = 6.8$ T). (d-f) XAS, XMCD and XMLD spectra at the $M_{4,5}$ Tb edges resulting from multiplet calculations for Tb atoms in the C_{6v} CF of graphene/Ir(111) surface.

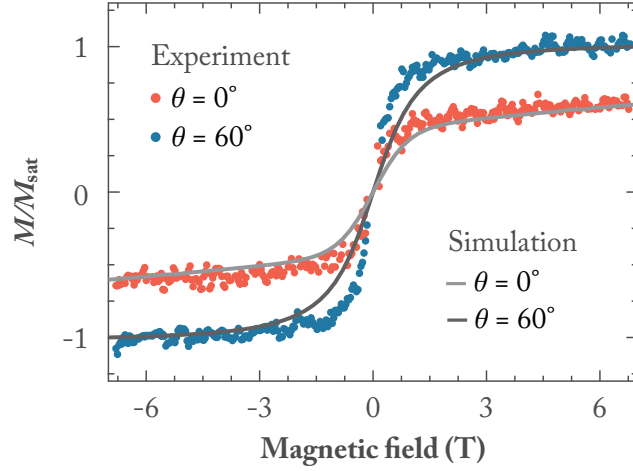


Figure 5.13 – Experimentally acquired magnetization curves for $\Theta = 0.003$ ML Tb on graphene/Ir(111) ($T = 2.5$ K, $\phi = 9\phi_0$ and $\dot{B} = 12$ mT s $^{-1}$), shown together with magnetization curves resulting from multiplet calculations for these atoms in the C_{6v} CF of graphene/Ir(111) surface. Experimental magnetization curves were acquired by measuring the XMCD signal at 1236.9 eV as a function of magnetic field.

tions assuming the adsorption of Tb atom in the hollow site of graphene, *i.e.*, center of the hexagonal carbon ring. The exact geometry and strength of employed point charges are given in Appendix A.

Our best fits of experimental spectra are shown with their experimental counterparts in Figure 5.12. They reproduce the in-plane anisotropy of the system and shape of XAS spectrum

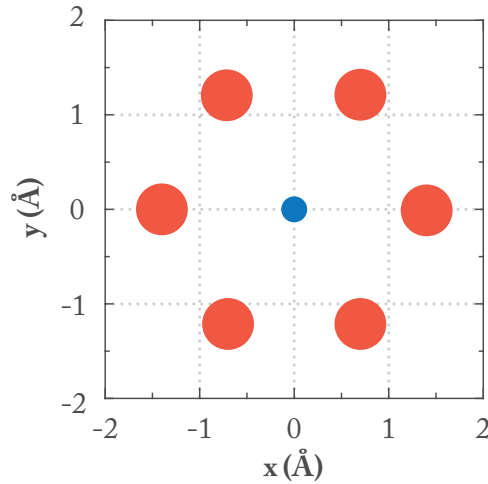


Figure 5.14 – Planar representation of the point charge crystal field employed in the multiplet calculations for Tb on graphene/Ir(111). Positive charges are marked with red, and negative with blue. The size of each circle reflects the charge value. The exact geometry and strength of depicted charges are given in Appendix A.

for $\theta = 0^\circ$ well. However, the intensities of XAS spectrum for $\theta = 60^\circ$, as well as the absolute intensities of XMCD spectra for both incidences of x-rays are not well reproduced. Better matching of these intensities with the employed crystal field configuration lead to poor matching in the shape and the ratio of the magnetization curves. Further fine tuning of the crystal field parameters could possibly lead to the better fit of the experimental features; however, due to the long calculation times, we refrained from such fine tuning. Simulating a full set of XAS, XMCD and XMLD spectra took over seven hours, and simulation of a meaningful pair of normal and grazing magnetization curves took approximately two days. Nevertheless, throughout our analysis, we established that it is unlikely that any fine tuning would result in different ground state of the system and it would only modify the energy separations between levels in the Tb energy diagram. Since, as it will be demonstrated later on, the ground state of this system is crucial for the lack of its magnetic stability, further adjustments to the crystal field parameters would not give any deeper insight into the properties of this system.

As anticipated for the XAS spectra, multiplet calculations reveal trivalent Tb configuration with 8 electrons in its $4f$ orbitals. The ground state multiplet of this system has $J = 6$ and its energy diagram is shown in Figure 5.15. The resulting total zero field splitting is the smallest among all the lanthanide atoms we studied on graphene/Ir(111) and it amounts to only 7 meV. The ground state of this system consists of a tunnel-split doublet with $J_z = \pm 3$, with the splitting of 0.16 meV between these two levels. This ground state is responsible for the lack of magnetic remanence in Tb atoms at $B = 0$ T, whereas for $B \neq 0$ T the small energy separation between other magnetic levels enables efficient magnetization reversal by scattering with electrons and phonons of the substrate.

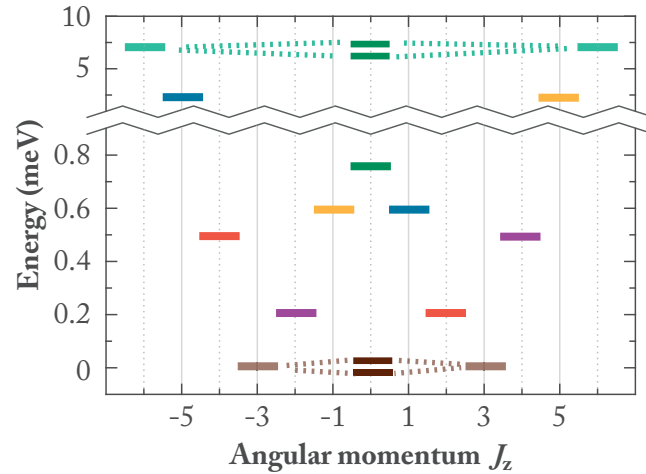


Figure 5.15 – The zero field splitting of the Tb lowest multiplet ($J = 6$) resulting from multiplet calculations. Each color identifies magnetic quantum states belonging to one of the six classes of eigenstates defined by the C_{6v} symmetry. Dashed lines connect doublets with quenched $\langle J_z \rangle$.

5.5 $4f$ occupation of lanthanides on graphene/Ir(111)

The electronic configuration and $4f$ occupancy of lanthanide atoms on a supporting substrate is ruled by two competing quantities, namely the energy needed to change from a divalent to a trivalent atomic configuration and the difference in their surface binding energies. The former is given as a sum of the $f-d$ promotion energy E_{fd} and the intershell coupling energy ΔE_c , called atomic correction energy. More details on those values can be found in [104, 105]. The binding energy of an atom strongly depends on its environment as it is ruled by the hybridization between its outer spd orbitals with the valence electrons of the substrate. The degree of hybridization, and hence the binding energy, increases with the increasing substrate DOS at E_F [85].

When atoms are placed on substrates with low DOS at E_F , such as graphene, the atomic correction is the leading term. Among the lanthanide atoms studied, this energy is the smallest for Tb, amounting to only 0.49 eV, while for all other investigated lanthanide atoms it is about three times larger [104]. The valency of lanthanide atoms on graphene follows this trend in atomic correction energy. The only lanthanide found in trivalent configuration is Tb, whereas all the other ones are in their divalent configuration. This finding for Tb is also in agreement with its well-known tendency to promote one $4f$ electron to the outer spd shells [26]. In addition, it has been demonstrated that the divalent state of Tb is highly unfavorable even for a free standing dimers, *i.e.*, that a single metallic bond is sufficient to trigger its trivalent configuration [106]. Hence, a Tb atom on graphene assumes a typical trivalent configuration that is also observed for TbPc₂ molecular magnets [2, 107].

The $4f$ occupation of divalent lanthanide atoms is highly sensitive to their coordination. An increase in coordination, either via cluster nucleation or attachment of contaminants leads to the promotion of trivalent configuration, as it has been demonstrated in Sections 3.7 and 3.8, and it will be further discussed in Section 5.8. In the case of cluster formation, valence bands are formed which enables transfer of an electron from $4f$ to spd bands [106]. Trivalent lanthanide atoms, on the other hand, even upon an increase in coordination keep their valency unchanged, as it has been demonstrated for trivalent lanthanide atoms on metal substrates [85, 87] and Tb atoms on graphene/Ir(111).

5.6 Magnetic stability of lanthanides on graphene/Ir(111)

The magnetic stability of lanthanide atoms on supporting substrates is governed by their quantum level structure, in particular by their ground state and height of the energy barrier required for thermally assisted magnetization reversal, U_{rev} . From multiplet calculations, we inferred large total zero field splitting with ground states protected against QTM for Nd, Dy and Ho on graphene/Ir(111). However, only Dy atoms show hysteresis in their magnetization curves, with significant magnetic stability on the timescale of our experiments and at $B = 0$ T and $T = 2.5$ K. This can be rationalized considering the different heights of U_{rev} of each of

5.7. Magnetic lifetime of lanthanides on graphene/Ir(111)

these systems, which are limited by the first excited states enabling thermally assisted QTM. Out of the systems considered, Dy indeed shows the highest value of U_{rev} , 5.6 meV.

The quantum tunneling of magnetization in the case of Dy and Nd is conveyed through their first tunnel-split doublets. However, smaller U_{rev} barrier and substantially larger separation between $J_z = \pm 3$ levels in the case of Nd with respect to Dy $J_z = \pm 6$ levels result in the lack of its magnetic stability at 2.5 K. In the case of Ho, a system with second highest U_{rev} barrier, the relaxation of magnetization is conveyed through the lowest non-axial excited states $\langle J_z \rangle = \pm 5.4$ that offer a path for assisted QTM.

In the case of Er atoms, magnetization reversal between $J_z = \pm 2$ ground states is easily achieved by thermal transitions to the lowest excited states. Within less than 1 meV there are several excited states that provide two paths for magnetization reversal. Hence, in this case the upper bound for U_{rev} can be defined as 1 meV. Finally, in the case of Tb, the lack of its magnetic stability on graphene/Ir(111) is due to its tunnel-split ground state doublet. This ground state supports QTM and hinders any magnetic stability of this system. The corresponding U_{rev} , together with $4f$ occupation, total angular momentum J and the ground state J_z for each system are summarized Table 5.1.

Table 5.1 – Occupation of $4f$ orbitals, total angular momentum J and effective $\langle J_z \rangle$ value of the ground state, together with U_{rev} , for lanthanide atoms on graphene/Ir(111) resulting from multiplet calculations.

Element	$4f$ occupation	J (\hbar)	$\langle J_z \rangle$ (\hbar)	U_{rev} (meV)
Nd	4	4	± 3.8	3.2
Tb	8	6	± 3	0
Dy	10	8	± 7	5.6
Ho	11	$15/2$	± 4.3	4.2
Er	12	6	± 2	<1

5.7 Magnetic lifetime of lanthanides on graphene/Ir(111)

The ground state doublet of Tb atoms on graphene/Ir(111) does not support magnetic stability, hence the magnetic lifetime of this system is zero. For the remaining lanthanide atoms, Nd, Ho and Er, it is possible to estimate their magnetic lifetime, similar to Dy atoms on HOPG in Section 1.4.3, by using the estimated value of $\tau_{0,\text{eff}}$ from the magnetic lifetime measurements for Dy atoms on the same substrate. Taking their U_{rev} values given in Table 5.1 and applying the Arrhenius law describing the magnetization reversal given by Equation 1.1 in Section 1.4.3, we obtain an estimate of a magnetic lifetime for each of these atom. The obtained values are given in Table 5.2. As expected from examination of their U_{rev} values, the only system besides Dy that shows considerable magnetic lifetime at 2.5 K is Ho with $\tau = 1.3$ s. Nevertheless, this lifetime is shorter than the time needed for the acquisition of a single point in our magnetization curves, which explains the lack of magnetic remanence in our measurements.

Table 5.2 – Estimated magnetic lifetime of lanthanide atoms on graphene/Ir(111) at 2.5 K.

	Nd	Ho	Er	Tb
Estimated lifetime (s)	0.01	1.3	$< 5 \times 10^{-7}$	0

Single lanthanide atoms on metal surfaces possess similar barriers for magnetization reversal as those on graphene/Ir(111). In particular, Er atoms on Pt(111) have U_{rev} similar to the one of Dy atoms on graphene/Ir(111), 5.3 meV [11]. However, they do not show remanence in their magnetization curves at $T = 2.5$ K, indicating a lifetime of order of seconds or less. This implies that the characteristic time τ_0 for lanthanide atoms on metal surfaces is at least three orders of magnitude shorter than the one on graphene, possibly due to a stronger coupling of the localized spins to both electrons and phonons of the surface.

5.8 Sensitivity to contamination of lanthanides on graphene/Ir(111)

High sensitivity of divalent lanthanide atoms to contamination has made XAS and XMCD experiments rather challenging in the limited time available at a synchrotron facility. This was especially the case during the acquisition of magnetization curves. Divalent and trivalent species of the same lanthanide atom have different magnetic properties; however, their spectral features appear in the same energy range and overlap. As magnetization curves are acquired by measuring the intensity of a chosen XMCD peak in a certain range of magnetic fields, any unwanted species with the spectral features at the same energy will contribute to the magnetization curves as well. In addition, a constant contamination during the measurements decreases the number of divalent atoms on the surface, which results in the faulty shape of the magnetization curves. Hence, to accurately acquire full set of data for each divalent lanthanide element, it was necessary to prepare several samples with as little contaminants as possible.

The sensitivity of lanthanide atoms to contamination has already been addressed in Section 3.8, where we discussed exposure time dependence of Dy XAS spectra. Here we extend that discussion to the other lanthanide atoms we studied on graphene/Ir(111).

5.8.1 Exposure time dependence of Nd XAS spectra

Figure 5.16(a) shows the XAS and XMCD spectra of two newly prepared samples of Nd on graphene/Ir(111), samples A and B. Both samples were prepared with the same experimental procedure during the same beamtime, and both have the same coverage, $\Theta = 0.002$ ML. However, their spectral features differ. In XAS spectra, the multiplet features appearing at the highest energy of both M_5 and M_4 edge, 977.3 eV and 999.3 eV, respectively, have larger intensity in the case of sample B. The differences in respective XMCD spectra are not so pronounced. The origin of these differences can be understood by comparing the initial XAS and XMCD spectra of sample A and its spectra after 160 minutes of measurements, shown in

5.8. Sensitivity to contamination of lanthanides on graphene/Ir(111)

Figure 5.16(b). The spectra have changed during the exposure time and, similarly to sample B, the highest energy features of each edge have increased intensity. In addition, the lower energy feature of M_5 edge (the peak at 975 eV) has significantly reduced intensity with respect to its initial value. The differences of initial and final XMCD spectra are also more pronounced. The overall intensity of XMCD M_5 edge has reduced, whereas the peaks of M_4 edge reversed their intensity distribution in the course of measurements.

The only way to justify the change in spectra with time at $T = 2.5$ K is to ascribe it to the continuous contamination of divalent Nd atoms on graphene/Ir(111). This reduces the proportion of divalent Nd and increases the proportion of trivalent Nd species on the surface. In the case of sample B, during the sample preparation, Nd atoms were subjected to higher initial contamination than in the case of sample A, possibly due to the small pressure difference in the UHV chamber. Furthermore, sample A was prepared three days after the sample B. During these three days, the Nd rod was additionally degassed, which also helped reducing the contamination of Nd atoms. The difference between samples A and B further demonstrates that special care is needed while preparing samples with lanthanide atoms, as it is easy to contaminate them and measure spurious instead of real magnetic properties of single atoms.

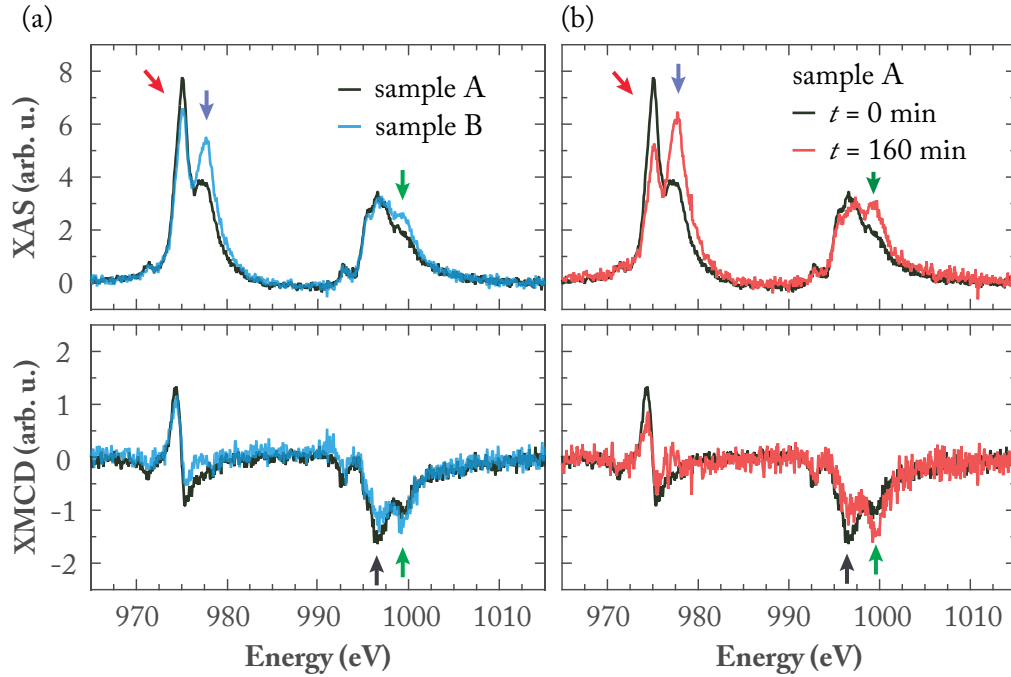


Figure 5.16 – (a) XAS and XMCD spectra of two different Nd samples (sample A and sample B) with the same coverage, $\Theta = 0.002$ ML. (b) XAS and XMCD spectra of the newly prepared sample A and its spectra after the exposure time of 160 minutes ($T_{\text{dep}} = 4$ K, $T = 2.5$ K, $B = 6.8$ T). Red, purple, black and green arrows point to the peaks at 975 eV, 977.3 eV, 996.7 eV and 999.3 eV, respectively.

5.8.2 Exposure time dependence of Ho XAS spectra

The comparison between XAS and XMCD spectra of freshly prepared sample of Ho atoms on graphene/Ir(111) and its spectra after four hours of measurements and exposure to the residual gas of the UHV chamber is shown in Figure 5.17. The continuous contamination of divalent Ho atoms has caused a shift of the spectral weight in Ho's M_5 edge towards higher energies in both XAS and XMCD spectra. The peak at 1349 eV has gained intensity, whereas peaks at lower energies have lost their intensity in this process. This is a clear sign of transformation of divalent Ho atoms into trivalent Ho species on the graphene/Ir(111) surface [85].

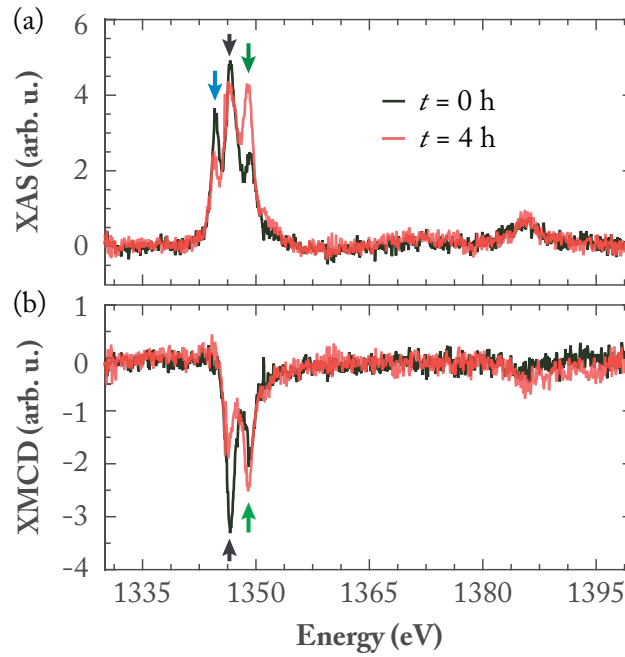


Figure 5.17 – (a) XAS and (b) XMCD spectra of Ho atoms on graphene/Ir(111) acquired on freshly prepared sample (black) and after $t = 4$ h of measurements (red) ($T_{\text{dep}} = 4$ K, $\Theta = 0.003$ ML; $T = 2.5$ K, $B = 6.8$ T). Blue, black and green arrows point to the peaks at 1344.6 eV, 1346.5 eV, and 1349 eV, respectively.

5.8.3 Exposure time dependence of Er XAS spectra

The comparison between XAS and XMCD spectra at M_5 edge of freshly prepared sample of Er atoms on graphene/Ir(111) (sample A, $\Theta = 0.004$ ML) and its spectra after $t = 2.5$ h hours of measurements is shown in Figure 5.18(a). Similarly to other divalent lanthanide atoms, in the course of measurements, Er M_5 edge has changed its appearance. In time, the peak at 1405.6 eV, associated with trivalent Er objects has increased its intensity in both XAS and XMCD spectra. The change in the other peaks of the M_5 edge is very small.

Figure 5.18(b) shows another sample of Er atoms on graphene/Ir(111), with higher coverage, $\Theta = 0.007$ ML (sample B). The distribution of intensities among the peaks of the M_5 edge

resembles those of sample A after prolonged exposure time, indicating a large amount of trivalent Er species at the surface. Note that the spectra of sample B were scaled for graphical purposes and in reality have over 1.5 times higher intensity than those shown in Figure 5.18(a), as a result of a higher coverage.

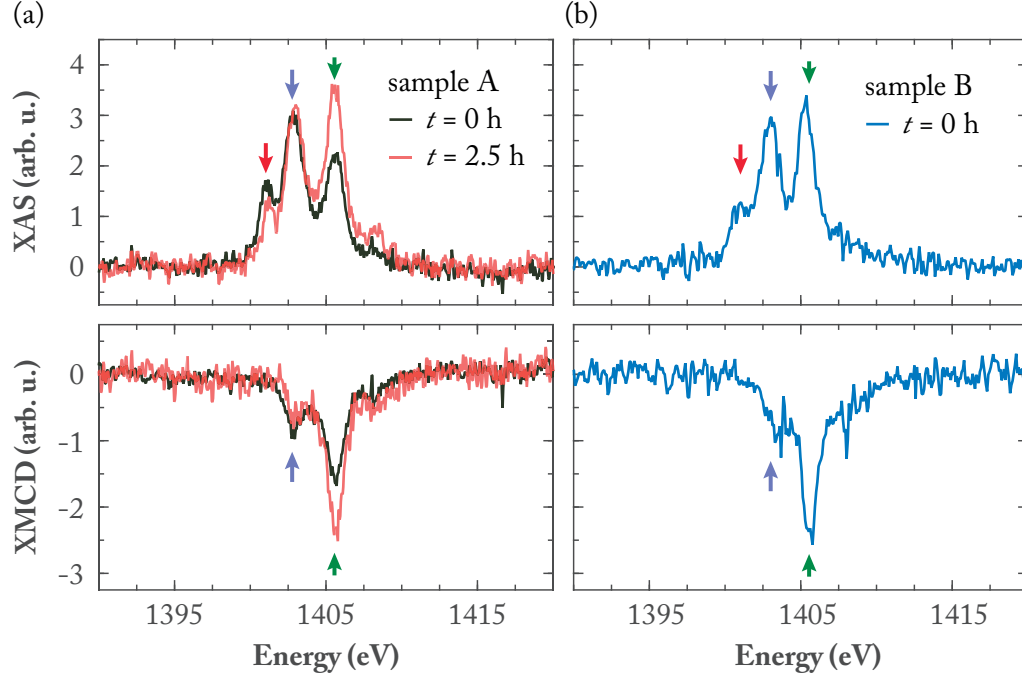


Figure 5.18 – (a) XAS and XMCD spectra of $\Theta = 0.004$ ML Er on graphene/Ir(111) acquired on a freshly prepared sample (black) and after $t = 2.5$ h of measurements (red). (b) XAS and XMCD spectra of $\Theta = 0.007$ ML Er on graphene/Ir(111) acquired on a freshly prepared sample ((a) $T_{\text{dep}} = 4$ K, $T = 2.5$ K; (b) $T_{\text{dep}} = 5$ K, $T = 5$ K; $B = 6.8$ T). Red, purple and green arrows point to the peaks at 1401 eV, 1402.8 eV, and 1405.6 eV, respectively.

An estimate of the share of divalent and trivalent Er objects on graphene/Ir(111) can be done by reproducing their XAS spectra with the superposition of respective spectra of free divalent and trivalent Er atoms. Such superposition will not reproduce all the features of the experimental spectra as it does not consider the effects of the crystal field. The spectra of free atoms were simulated by multiplet calculations, and their areas were subsequently normalized to the number of holes in the $4f$ orbitals, 2 in the case of divalent and 3 in the case of trivalent configuration. These spectra are shown in Figure 5.19(a).

To reproduce experimental spectra, various shares of divalent and trivalent spectra in the superposition were tried until the combination that resembles experimental spectra was found. The area of such superposition was subsequently normalized to match the area of the experimental spectra. Figure 5.19(b) shows the resulting superposition for the sample A. Its XAS features are well reproduced by assuming approximately $(66 \pm 5)\%$ of divalent, and $(34 \pm 5)\%$ trivalent Er objects on the surface. Reproducing the XAS spectra of sample B revealed

only $(53 \pm 3)\%$ of divalent Er atoms on the surface. Such large shares of trivalent Er objects at such low coverages ($\Theta = 0.004$ ML and $\Theta = 0.007$ ML, respectively) indicates high sensitivity of Er atoms to contamination.

The high sensitivity of Er atoms to contamination and low intensity of the divalent XMCD features has prevented us from acquiring magnetization curves that are characteristic of solely divalent Er atoms.

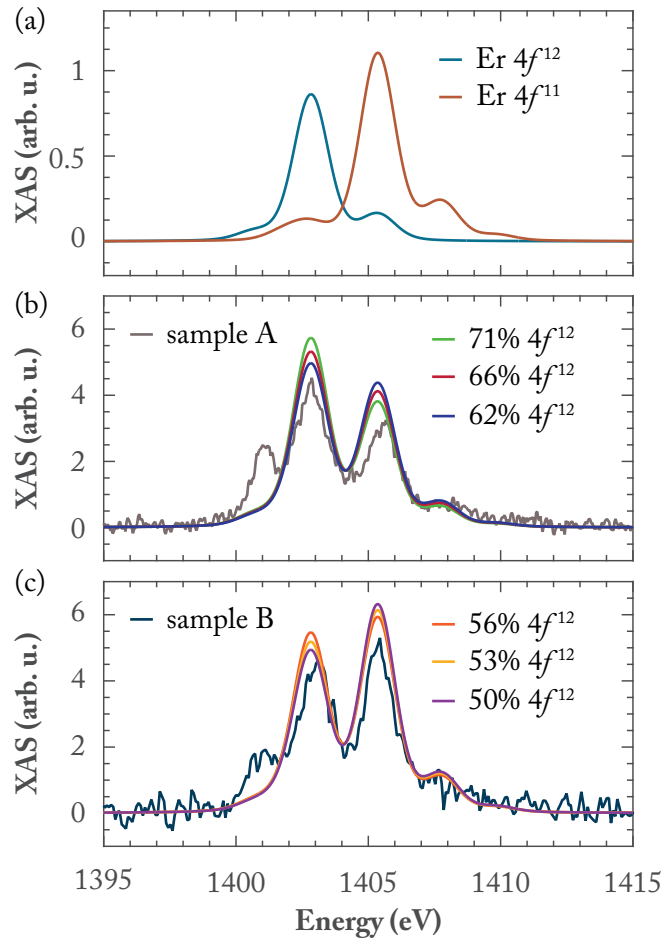


Figure 5.19 – (a) XAS spectra at the M_5 edge of free Er atoms with divalent $4f^{12}$ and trivalent $4f^{11}$ electronic configuration. The area of the entire XAS spectra was normalized to the number of holes in $4f$ orbitals, to 2 in the case of divalent and to 3 in the case of trivalent spectra. (b) Fitting of the $\Theta = 0.004$ ML Er XAS spectrum by superposing divalent and trivalent spectra of free atoms shown in (a). (c) Fitting of the $\Theta = 0.007$ ML Er XAS spectrum by superposing divalent and trivalent spectra of free atoms shown in (a). The number indicated with each spectrum indicates the fraction of divalent atoms contributing to the total spectrum.

5.8.4 Exposure time dependence of Tb XAS spectra

The comparison between XAS and XMCD spectra of a freshly prepared sample of $\Theta = 0.003$ ML Tb on graphene/Ir(111) and its spectra after three hours of exposure to the residual gas of the UHV chamber is shown in Figure 5.20(a). Unlike in the case of divalent lanthanide atoms, the spectra and hence the $4f$ occupation of the trivalent Tb atoms remained unchanged during the course of measurements. The valency of Tb atoms remains unchanged even in clusters. Figure 5.20(b) shows XAS and XMCD spectra acquired for $\Theta = 0.015$ ML Tb, coverage at which there is a considerable amount of Tb dimers and bigger clusters on the graphene/Ir(111) surface. The spectral features of this higher coverage sample resemble those of the low coverage one shown in Figure 5.20(a).

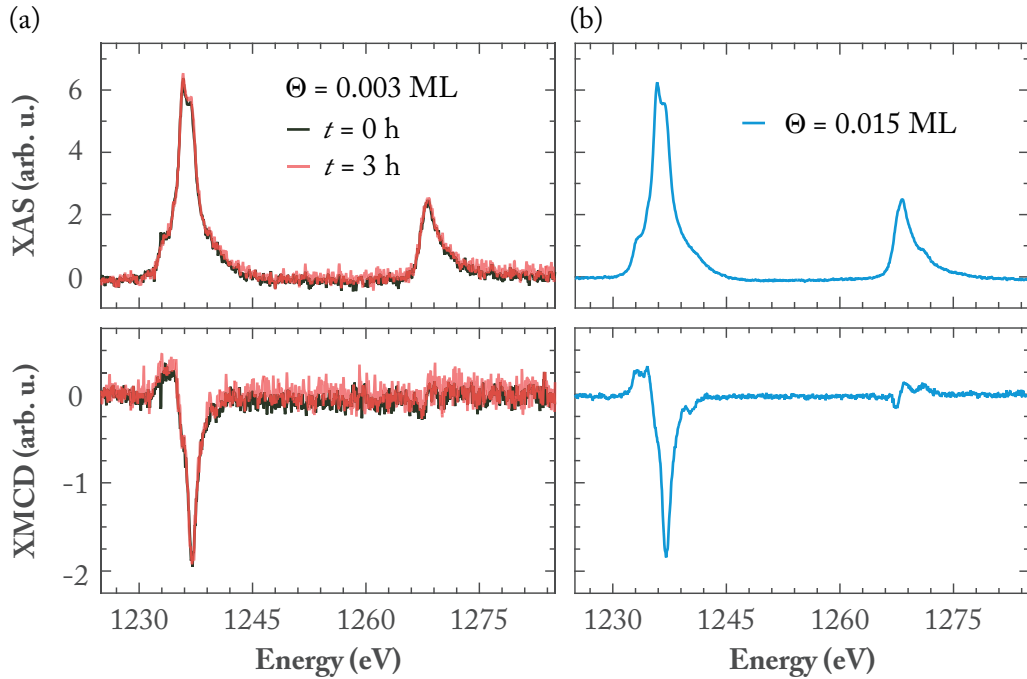


Figure 5.20 – (a) XAS and XMCD spectra of $\Theta = 0.003$ ML Tb on graphene/Ir(111) acquired on freshly prepared sample (black) and after $t = 3$ h of measurements (red). (b) XAS and XMCD spectra of $\Theta = 0.015$ ML Tb on graphene/Ir(111) ($T_{\text{dep}} = 4$ K, $T = 2.5$ K, $B = 6.8$ T). Spectra in (b) were scaled to match the scale of spectra in (a)

5.9 Sum rules for lanthanide atoms

Sum rules give a valid estimate of angular momenta of atoms only in case where all the XAS signal originates from a single species on a surface. In the case of lanthanide atoms, the divalent atomic species are liable to contamination and dimers form already for very low coverages due to the large impingement area for dimer formation [71, 87]. The energy range in which the XAS spectral features of these three species appear overlaps, and they all contribute to the acquired XAS spectra of a certain lanthanide studied. Therefore, when applying sum

rules to the XAS and XMCD spectra, the resulting momenta do not describe the desired single atoms, but give average values over the entire ensemble, consisting of all the species on the surface. In addition, sum rules are valid only in the case of the isotropic integral of the XAS intensity, which is generally not the case with lanthanide atoms on surfaces [85]. Multiplet calculations are, on the other hand, done for the single atoms only and hence represent a better tool for estimating angular momenta of lanthanide atoms.

Nevertheless, we have applied the sum rules to the experimental spectra of lanthanide atoms on graphene. The resulting expectation values of spin, orbital and total angular momenta, together with values resulting from multiplet calculations, are given in Table 5.3.

Table 5.3 – Expectation values of spin $\langle S_z \rangle$, orbital $\langle L_z \rangle$ and total $\langle J_z \rangle$ angular momenta of lanthanide atoms on graphene/Ir(111), resulting from both multiplet calculations and sum rules applied to experimental spectra. n_h marks the number of $4f$ holes used in calculations. The values are given for normal direction of x-rays, $\theta = 0^\circ$.

	n_h	calculation	$\langle S_z \rangle$	$\langle L_z \rangle$	$\langle J_z \rangle$
Tb	6	<i>sum rules</i>	0.7 ± 0.1	0.88 ± 0.05	1.6 ± 0.1
		<i>multiplet calc.</i>	1.44	1.56	3.0
Dy	4	<i>sum rules</i>	1.2 ± 0.1	3.8 ± 0.1	5.0 ± 0.1
		<i>multiplet calc.</i>	1.68	5.32	7.0
Nd	10	<i>sum rules</i>	-0.75 ± 0.04	4.4 ± 0.2	3.7 ± 0.2
		<i>multiplet calc.</i>	-1.53	5.36	3.84
Ho	3	<i>sum rules</i>	0.63 ± 0.04	2.7 ± 0.1	3.3 ± 0.1
		<i>multiplet calc.</i>	0.84	3.44	4.29
Er	2	<i>sum rules</i>	0.38 ± 0.06	1.7 ± 0.1	2.1 ± 0.1
		<i>multiplet calc.</i>	0.33	1.67	2.0

In most cases, the sum rules underestimate the values of angular momenta. In the case of Dy atoms, all angular momenta resulting from sum rules are about 30% smaller than those resulting from multiplet calculations, and a similar difference is also found for Ho atoms. The largest difference is obtained for Tb atoms, where sum rules' angular momenta are about 50% smaller than their counterparts resulting from multiplet calculations. Surprisingly, an excellent match of angular momenta is achieved for Er atoms. Considering the large amount of trivalent Er objects on the graphene/Ir(111) surface, this must be ascribed to coincidence rather than being considered as a confirmation that sum rules work well in this case. The same is true for Nd atoms, where sum rules underestimate spin angular momentum by 50% and orbital by about 20%, but the total angular momentum shows a good agreement between these two methods.

To this day, among all the lanthanide atoms we studied, the DFT calculations were carried out only for Nd atoms on freestanding graphene [102]. The obtained value for spin angular momentum, $\langle S_z \rangle = 1.84$ is only a little larger than the value we obtained from multiplet calculations, and the main difference originates from the value of orbital angular momentum,

$\langle L_z \rangle = 2.58$, which is greatly underestimated by DFT calculations.

6 Co atoms on hexagonal boron nitride

In addition to lanthanide atoms on decoupling layers, we investigated one transition metal atom, Co. We investigated its magnetic properties on *h*-BN. A free Co atom has a large orbital momentum. If this momentum remains preserved upon adsorption on the *h*-BN surface, this could result in a large magnetic anisotropy. In this Chapter, we present the results of the combined XMCD and multiplet studies for Co atoms on *h*-BN/Ru(0001) and *h*-BN/Ir(111).

Work contribution. *As part of a team led by Dr. Stefano Rusponi, I contributed to all XMCD measurements presented in this Chapter. Further, I carried out the data analysis and multiplet calculations.*

6.1 Co on *h*-BN

As already discussed in Section 4.5, *h*-BN is a two-dimensional material, isostructural to graphene. However, unlike graphene, it is a wide band gap insulator, with a gap of about 6 eV [98]. Growing *h*-BN on supporting substrates results in a moiré superstructure whose properties depend on the interaction between the *h*-BN layer and the underlying substrate. The weak interaction of *h*-BN with Ir(111) results in their large mean separation of 3.13 Å, and a weak corrugation of the *h*-BN layer of 0.35 Å [101]. The interaction with Ru(0001) is strong, resulting in a smaller mean distance, 2.75 Å, and a greater corrugation of the *h*-BN layer of about 1.5 Å [100].

The interaction of a decoupling layer with the underlying metal surface can greatly influence the magnetic properties of adsorbed atoms, as is the case for Co atoms on graphene [108]. To investigate whether the same is true for Co atoms on *h*-BN, we investigated their magnetic properties on *h*-BN/Ru(0001) and *h*-BN/Ir(111).

6.1.1 Co on *h*-BN/Ru(0001)

To investigate the magnetic properties of Co on *h*-BN/Ru(0001), we deposited $\Theta = 0.008$ ML of Co on a freshly prepared *h*-BN/Ru(0001) surface. Subsequently, we acquired the XAS, XMCD and XMLD spectra, as well as the magnetization curves at normal and grazing incidence at Co $L_{2,3}$ edges shown in Figure 6.1(a-d).

The XAS and XMCD spectra of Co atoms are characterized by pronounced features at L_3 edge, notably peaks at 777 eV and 778.9 eV, whereas a broad featureless L_2 edge is present in XAS, and absent in XMCD spectra (Figure 6.1(a,b)). The presence of multiplet features at the Co L_3 edge indicates a weak hybridization of Co $3d$ orbitals with *h*-BN surface, and their high degree of localization. These spectra are characteristic of Co $3d^8$ occupancy [108, 109]. The $3d^9$ occupancy can be excluded as the Co XAS spectra for this configuration are characterized by a single peak at the L_3 edge [110]. Similar weak hybridization has also been observed for Co atoms on other decoupling substrates [8, 108, 111–113] and alkali metal films [109].

The long tail present at the right side of the L_3 edge in XAS spectra does not have its counterpart in XMCD spectra. This suggests that, in addition to magnetic Co atoms, there are one or more Co species with no or almost no net magnetization [113] present at the *h*-BN/Ru(0001) surface, possibly Co contaminated with hydrogen atoms. For Co atoms on *h*-BN/Rh(111), it has been demonstrated that the adsorption of one or two hydrogen atoms on a single Co atom can result in the strong reduction of the magnetic moment due to the distortion of the crystal field or Kondo effect, respectively [114].

The higher intensity of the XMCD spectra in normal with respect to grazing incidence of x-rays indicates an out-of-plane easy magnetization axis for Co atoms on this surface. The paramagnetic behavior of both normal and grazing magnetization curves (Figure 6.1(d)) indicates lifetime of seconds or less. In addition, the magnetization curves indicate a weak magnetic anisotropy of this system.

Experimental linear XAS spectra, which was used to obtain XMLD spectra shown in Figure 6.1(c), had only a partial overlap with the background spectra we acquired prior to deposition of Co atoms. Hence, the process of subtracting a polynomial background may have affected the spectral features. As a result, the only feature that should be retained is the variation of XMLD with the magnetic field. As it can be seen, the intensity of XMLD is larger at $B = 0.05$ T than at $B = 6.8$ T.

To this day, the adsorption site of Co atoms on *h*-BN/Ru(0001) has not been determined experimentally. Thus, we used multiplet calculations to gain an insight into the electronic properties of this system as a function of the local environment generated by the possible adsorption site. The DFT calculations performed for Co atoms on freestanding *h*-BN found a hollow adsorption site for these atoms [114–116]. The same adsorption site was found by DFT for Co atoms adsorbed on *h*-BN/Ni(111) [116]. Hence, we started our calculations by considering hollow adsorption site for Co atoms on *h*-BN/Ru(0001).

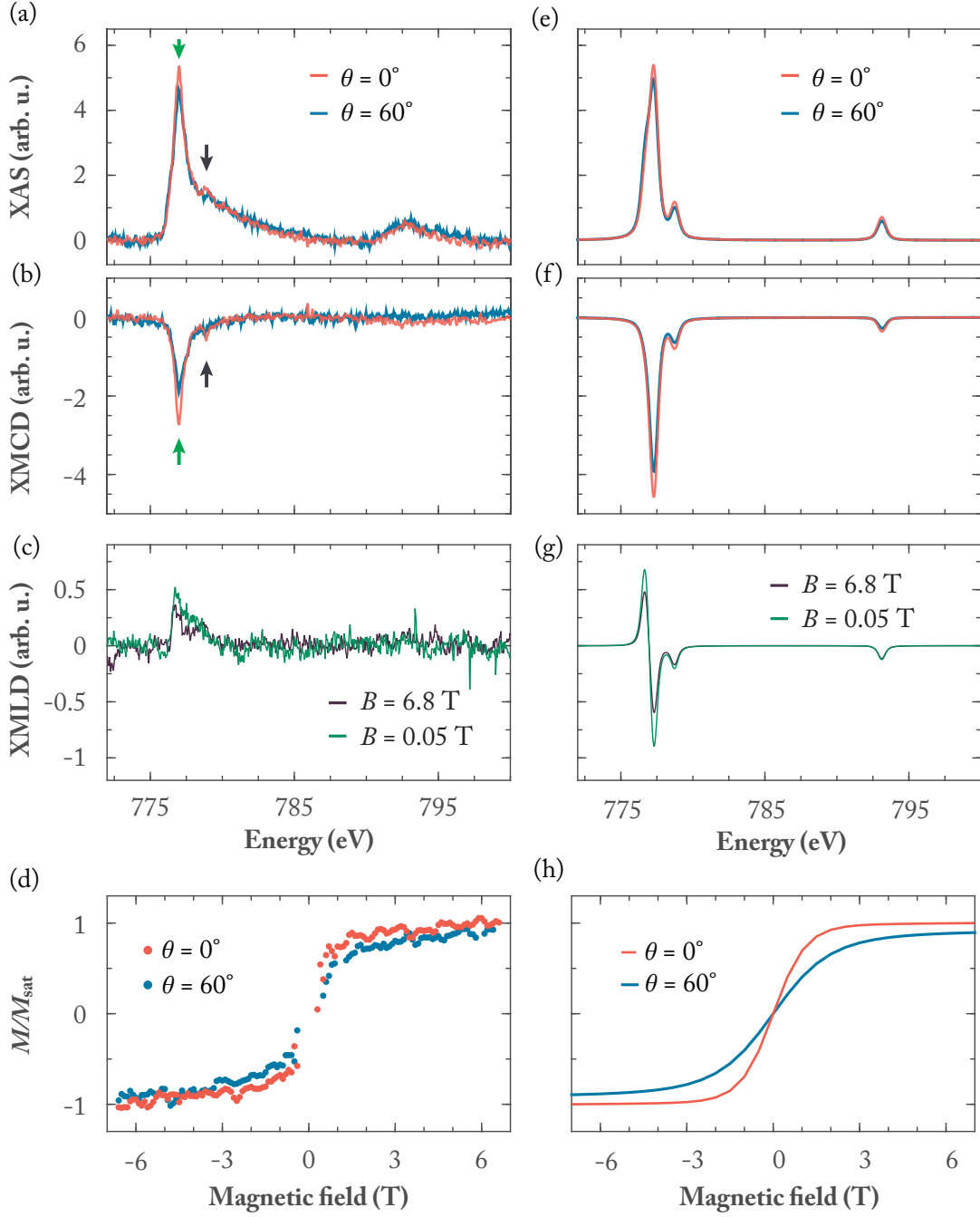


Figure 6.1 – (a-d) Experimentally acquired XAS, XMCD and XMLD spectra, as well as magnetization curves of $\Theta = 0.008$ ML Co on *h*-BN/Ru(0001). Magnetization curves were acquired by measuring the XMCD signal at 777 eV as a function of the magnetic field. This peak is indicated by the green arrow in (b). The black arrow points to the peak at 778.9 eV. ($T_{\text{dep}} = 4$ K, $T = 2.5$ K; (a,b) $B = 6.8$ T, (d) $\phi = 13\phi_0$, with $\phi_0 = 0.003$ photons $\text{nm}^{-2} \text{s}^{-1}$, $\dot{B} = 33$ mT s^{-1}). (e-h) XAS, XMCD and XMLD spectra, as well as magnetization curves resulting from multiplet calculations for Co atoms in the C_{3v} CF of *h*-BN/Ru(0001) surface.

Multiplet calculations were performed using the point charge crystal field scheme, whose planar representation is shown in Figure 6.2. It consists of negative charges placed at positions of nitrogen atoms, and positive charges placed at positions of boron atoms of *h*-BN hexagonal ring. In addition, there is small positive charge in the middle of this hexagonal ring. In calculations, Co atoms were assumed to be adsorbed in the center of this hexagonal ring. This adsorption site generates a three-fold symmetric C_{3v} crystal field to the adsorbed Co atoms. The exact geometry and strength of employed point charges are given in Appendix A.

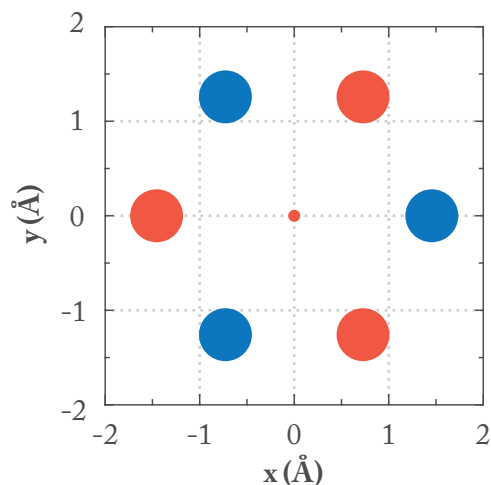


Figure 6.2 – Planar representation of the point charge crystal field employed in the multiplet calculations for Co atoms on *h*-BN/Ru(0001). The blue circles represent negative and red positive charge. The exact geometry and strength of depicted charges are given in Appendix A.

In addition to the hollow adsorption site, we performed a series of multiplet calculations for adsorption of Co atoms on top of the negatively charged nitrogen ion. This adsorption site was considered since Co atoms show a tendency to adsorb on negatively charged atomic sites, such as on the negatively charged oxygen ions of MgO [8, 117]. Nevertheless, these simulations did not reproduce the experimental spectra as well as simulations for the hollow adsorption site did. Hence, in the following, only the simulations obtained for the hollow adsorption site are considered. The XAS, XMCD and XMLD spectra, as well as magnetization curves, resulting from multiplet calculations are shown in Figure 6.1, together with their experimental counterparts.

Overall, the simulations of XAS and XMCD reproduce the experimental spectra well and confirm the $3d^8$ electronic occupation of Co atoms. In particular, multiplet features of XAS and XMCD spectra are well reproduced (Figure 6.1(e,f)), apart from the long tail of L_3 edge. As mentioned before, this tail originates from Co species with vanishing magnetic moment which were not considered in our calculations. These additional Co species are also responsible for the dissimilar ratios of intensities between Co XAS and XMCD spectra obtained for experiment and simulation. Nevertheless, our simulations reproduce the higher intensity of XMCD in normal incidence of x-rays, and hence an out-of-plane easy magnetization axis of Co atoms

on *h*-BN/Ru(0001). The trend in XMLD spectra is also reproduced, showing higher intensity of XMLD for $B = 0.05$ T with respect to $B = 6.8$ T. Finally, the simulated magnetization curves are also well reproduced.

Using the information on the occupancy and hence the number of holes in Co 3*d* orbitals gained from multiplet calculations, $n_h = 2$, we performed sum rule analysis for the experimentally acquired XAS and XMCD spectra, as well as for the simulated ones, to obtain effective spin ($m_{S_{eff}}$) and orbital (m_L) magnetic moments for Co atoms on *h*-BN/Ru(0001). The effective spin magnetic moment resulting from sum rules is comprised of both spin magnetic moment and spin dipole magnetic moment, as with this technique it is not possible to determine their contributions independently. Further, we calculated the ratio of the orbital and effective spin magnetic moments, $m_L/m_{S_{eff}}$. This ratio is obtained without the assumption of n_h and considers the XMCD spectra only [109]. The obtained values are given in Table 6.1.

Table 6.1 – Effective spin and orbital magnetic moments of Co atoms on *h*-BN/Ru(0001), resulting from sum rule analysis of experimental and simulated XAS and XMCD spectra using $n_h = 2$; the values are expressed in μ_B .

		$\theta = 0^\circ$	$\theta = 60^\circ$
sum rules	$m_{S_{eff}}$	1.0 ± 0.1	0.9 ± 0.1
	m_L	0.7 ± 0.1	0.6 ± 0.1
	$m_L/m_{S_{eff}}$	0.67	0.67
multiplet calc.	$m_{S_{eff}}$	2.21	1.98
	m_L	1.81	1.60
	$m_L/m_{S_{eff}}$	0.82	0.81

In comparison with the values obtained for simulated spectra, the magnetic moments obtained for experimental spectra are rather low. For instance, for normal incidence of x-rays, the obtained values for experimental spectra are $m_{S_{eff}(E)} = (1.0 \pm 0.1) \mu_B$ and $m_{L(E)} = (0.7 \pm 0.1) \mu_B$. These values are over two times smaller than the values obtained for respective simulated spectra. This discrepancy could be attributed to a significant proportion of the nonmagnetic Co species on the *h*-BN surface, which would reduce the overall effective spin and orbital moments of the Co ensemble. The ratio of orbital and spin effective moment depends only on the XMCD spectrum. Therefore, only the magnetic Co species contribute to its value. As a result, the $m_L/m_{S_{eff}}$ values show much better matching between experiment and simulation. For both incidences of x-rays, the experimental $m_L/m_{S_{eff}}$ values are less than 20% smaller than the ones obtained for simulations.

Multiplet calculations reveal that a large part of the orbital momentum of free Co atoms ($L = 3$ in $3d^8$ configuration) is preserved upon adsorption of these atoms on the *h*-BN surface, resulting in orbital magnetic moment of $m_{L(S)} = 1.81 \mu_B$ in normal incidence. This confirms a weak hybridization of Co atoms with *h*-BN/Ru(0001).

6.1.2 Co on *h*-BN/Ir(111)

With the aim of investigating the magnetic properties of Co on *h*-BN/Ir(111), we deposited $\Theta = 0.005$ ML of Co on a clean *h*-BN/Ir(111) surface. The experimentally acquired XAS, XMCD and XMLD spectra, as well as magnetization curves at Co $L_{2,3}$ edges are shown in Figure 6.3(a-d).

Similar to Co atoms on *h*-BN/Ru(0001), XAS and XMCD spectra of Co atoms on *h*-BN/Ir(111) are characterized by multiplet features in their L_3 edge, with peaks at 777 eV and 778.9 eV, indicating the highly localized nature of their $3d$ orbitals. The long tail of the XAS L_3 edge, seen in the case of Co on *h*-BN/Ru(0001), is less pronounced (Figure 6.3(a)). The Co L_2 edge is present only in XAS spectra and it lacks a multiplet structure.

The XMCD spectra acquired in normal and grazing incidence of x-rays have equal intensities (Figure 6.1(b)), indicating a lack of magnetic anisotropy for Co atoms on *h*-BN/Ir(111) and no preferential direction of the magnetization. This is furthermore corroborated by the magnetization curves (Figure 6.3(d)) which show identical paramagnetic behavior for the two incidence angles of x-rays.

Since the acquired XAS and XMCD spectra of Co on *h*-BN/Ir(111) look similar to those of Co on *h*-BN/Ru(0001), it is safe to assume the same adsorption site and electronic configuration in these two cases. We performed multiplet calculations assuming $3d^8$ electronic configuration and using the point charge crystal field scheme shown in Figure 6.2 as a starting point in our simulations. As it turned out, the charge configuration that gave the best results was very similar to the one for Co on *h*-BN/Ru(0001). The only difference between these two cases is the vertical position of the central positive charge. In the case of *h*-BN/Ir(111), this charge is 0.1 Å further from the Co atom than in the case of *h*-BN/Ru(0001). The exact geometry and strength of employed point charges are given in Appendix A. The spectra and magnetization curves resulting from our simulations are shown with their experimental counterparts in Figure 6.3.

The simulated XAS and XMCD spectra reproduce the multiplet features observed in the experimental spectra well (Figure 6.3(e,f)). However, in our simulations, we were unable to entirely reproduce the isotropy of the XMCD spectra, which is also reflected in the small anisotropy shown by the simulated magnetization curves (Figure 6.3(h)). In addition, we were unable to reproduce experimental ratios between Co XAS and XMCD spectra. Similar to the case of *h*-BN/Ru(0001), this can be ascribed to additional Co species on the *h*-BN/Ir(111) surface with vanishing magnetic moment. The simulated XMLD spectra shown in Figure 6.3(g) capture the trend in XMLD intensity observed in experimental spectra, with the XMLD intensity at $B = 6.8$ T being larger than the one at $B = 0.05$ T. This is opposite to the case of Co atoms on *h*-BN/Ru(0001).

To obtain the effective spin and orbital magnetic moments, we applied sum rules to both experimental and simulated XAS and XMCD spectra. The obtained values, together with their

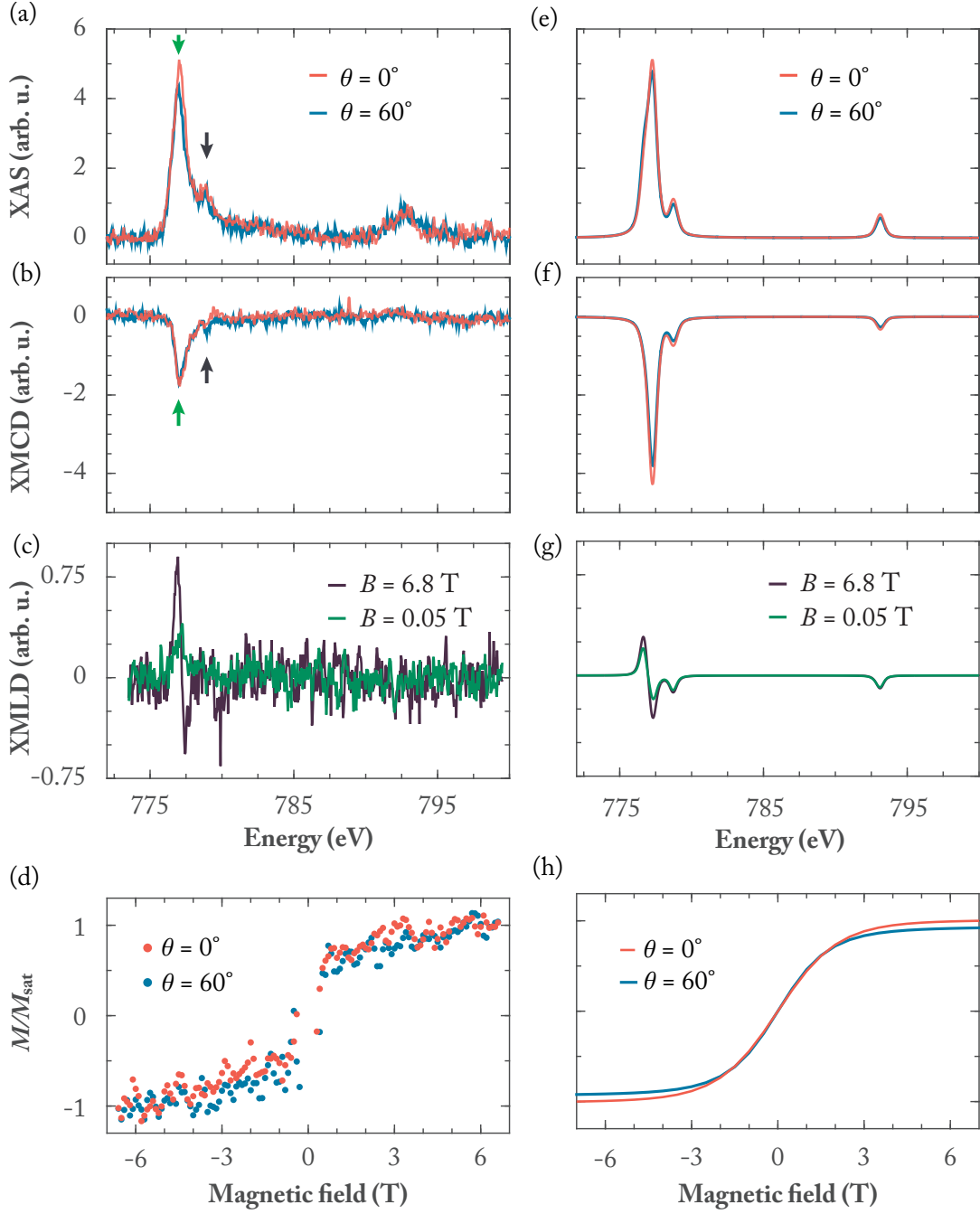


Figure 6.3 – (a-d) Experimentally acquired XAS, XMCD and XMLD spectra, as well as magnetization curves of $\Theta = 0.005$ ML Co on *h*-BN/Ir(111). Magnetization curves were acquired by measuring the XMCD signal at 777 eV as a function of the magnetic field. This peak is indicated by the green arrow in (b). The black arrow points to the peak at 778.9 eV ($T_{\text{dep}} = 4$ K, $T = 2.5$ K; (a,b) $B = 6.8$ T, (d) $\phi = 12\phi_0$, $\dot{B} = 33$ mT s $^{-1}$). (e-h) XAS, XMCD and XMLD spectra, as well as magnetization curves resulting from multiplet calculations for Co atoms in the C_{3v} CF of *h*-BN/Ir(111) surface.

ratios, are given in Table 6.2. Peculiarly, despite the differences in the experimental spectra between Co on *h*-BN/Ru(0001) and *h*-BN/Ir(111), the values obtained from sum rules for these experimental spectra are, within the error bars, the same. The values obtained for simulated spectra are also comparable to those for simulated spectra of Co atoms on *h*-BN/Ru(0001). Hence, in this case as well, the effective spin and orbital magnetic moments obtained for the experimental spectra are relatively small in comparison to the ones obtained from simulated spectra. This could also be ascribed to the Co species with vanishing magnetization, which contribute to the experimental XAS but not to XMCD spectra, and would reduce the overall magnetic moments of the investigated Co ensemble.

Table 6.2 – Effective spin and orbital magnetic moments of Co atoms on *h*-BN/Ir(111), resulting from sum rule analysis of experimental and simulated XAS and XMCD spectra $n_h = 2$; the values are expressed in μ_B .

		$\theta = 0^\circ$	$\theta = 60^\circ$
sum rules	$m_{S_{eff}}$	1.0 ± 0.2	1.0 ± 0.2
	m_L	0.6 ± 0.1	0.7 ± 0.1
	$m_L/m_{S_{eff}}$	0.67	0.67
multiplet calc.	$m_{S_{eff}}$	2.17	2.01
	m_L	1.77	1.62
	$m_L/m_{S_{eff}}$	0.82	0.81

6.2 Discussion

The observed multiplet features Co atoms suggest their low hybridization with the *h*-BN surface and the preservation of the atomic character of their electronic states. This is further supported by the sum rule analysis of their XAS and XMCD spectra which reveals unquenched orbital momenta for these atoms. The analysis of experimental spectra in normal incidence reveals comparable orbital magnetic moments for Co atoms on both *h*-BN/Ru(0001) and *h*-BN/Ir(111) of about $m_{L(E)} = 0.7 \mu_B$. In addition, the analysis of simulated spectra indicates that the preserved orbital momentum could be even larger. In the case of experimental spectra, the additional Co species with vanishing magnetization greatly reduce the overall magnetic moment of the ensemble, which is not taken into account in simulations. The preservation of orbital momenta in Co atoms did not result in a large magnetic anisotropy for these atoms on *h*-BN. Their adsorption in the hollow site of the *h*-BN lattice, and the surrounding alternating positive and negative charges placed on the positions of boron and nitrogen atoms, respectively, did not result in the strong uniaxial bond which would promote large magnetic anisotropy in Co atoms.

In the case of graphene grown on supporting substrates, changing the supporting metal surface greatly influences both adsorption site and magnetic properties of Co adatoms on graphene [108]. In particular, for strongly interacting graphene/Ru(0001) system, Co atoms adsorb on top of carbon atoms, resulting in an out-of-plane easy axis with large magnetic anisotropy.

In the case of weakly interacting graphene/Ir(111) system, Co atoms adsorb in hollow sites of the graphene lattice, resulting in an in-plane easy axis and lower magnetic anisotropy. In contrast, the interaction of *h*-BN with the supporting metal substrate does not have such a great effect on the adsorbed Co atoms. Both in the case of strongly interacting *h*-BN/Ru(0001) and weakly interacting *h*-BN/Ir(111) systems, our multiplet calculations suggest the adsorption of Co atoms in the hollow site. In the case of *h*-BN/Ru(0001), this site results in an out-of-plane easy axis of Co with a weak magnetic anisotropy, whereas in the case of *h*-BN/Ir(111), the magnetic moment of Co atoms is isotropic. The small difference in the crystal field caused by the change of supporting metal substrate from Ru(0001) to Ir(111) is further emphasized by the point charge crystal field we used to simulate the experimental spectra of Co atoms in these two cases. They only differ in the position of the small charge of $q = 0.27 e$, which is in the case of *h*-BN/Ir(111) 0.1 Å further away from the Co atom.

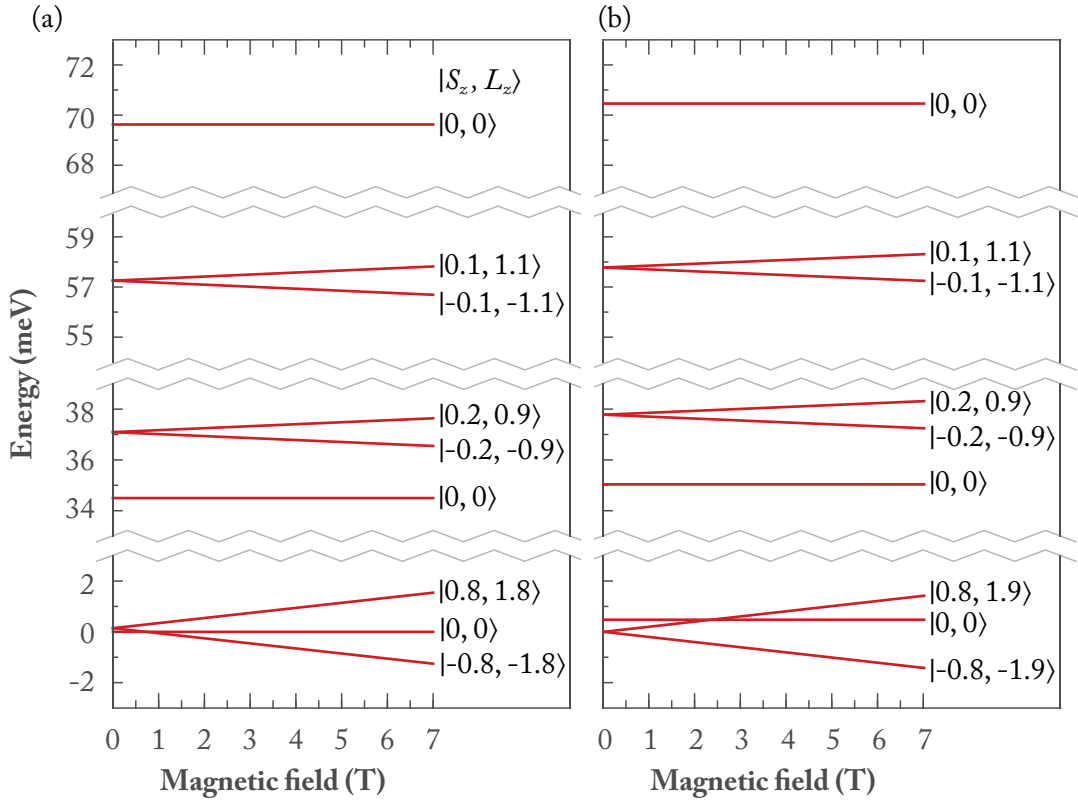


Figure 6.4 – Zeeman diagram of the Co magnetic levels between $B = 0$ T and $B = 7$ T for these atoms on (a) *h*-BN/Ir(111) and (b) *h*-BN/Ru(0001). All states are labeled with the following notation: $|S_z, L_z\rangle$.

Cobalt atoms on both *h*-BN/Ru(0001) and *h*-BN/Ir(111) show paramagnetic behavior in their magnetization curves, indicating a magnetic lifetime of order of seconds or less on these substrates. Our multiplet calculations indicate a very small barrier for the magnetization reversal of Co atoms. In the case of Co on *h*-BN/Ir(111), we obtained the $\langle S_z \rangle = 0$ ground state, with the excited doublet $\langle S_z \rangle = \pm 0.8$ only 0.14 meV above the ground state. For this

Chapter 6. Co atoms on hexagonal boron nitride

system, the ground state singlet is not compatible with magnetic bistability. In the case of Co on *h*-BN/Ru(0001), its ground state doublet $\langle S_z \rangle = \pm 0.8$ would be compatible with magnetic bistability; however, the $\langle S_z \rangle = 0$ state is only 0.4 meV higher in energy. This effective barrier is very small and at the measurement temperature of $T = 2.5$ K no magnetic stability is expected for Co atoms on this surface. The resulting energy level diagrams for these two systems are shown in Figure 6.4.

Conclusion and outlook

The aim of the work presented in this thesis was to study the underlying interactions and conditions governing the magnetic stability in surface supported atoms, and, ultimately, to achieve the long magnetic lifetime in such systems. Further, we investigated the moiré pattern of graphene/Ir(111) surface as a template for the self-assembly of single atom magnets.

The first step towards achieving magnetic stability in surface supported atoms is decoupling them from the metallic substrate to minimize the scattering with electrons and phonons. This step, although necessary, is not sufficient to achieve the desired long magnetic lifetimes as the key role is played by the crystal field and its symmetry, imposed to the atom's magnetic levels by the adsorption site on the chosen decoupling surface.

On the surface of graphene, the investigated lanthanide atoms adsorb in its hollow site. This generates a six-fold symmetric crystal field environment to the adsorbed atoms. Throughout our analysis, we established that the graphene surface provides each of these atoms with a unique crystal field environment. This is in contrast to lanthanide molecular magnets, where replacing one lanthanide ion with another does not cause the redistribution of crystal field charges, but rather rescales them [118]. Further, the interaction between lanthanide atoms and graphene leads to two different electronic configurations, namely divalent $4f^n$ and trivalent $4f^{n-1}$. Lanthanide atoms on graphene are predominantly found in their divalent configuration, and, among the studied atoms, only Tb is found in its trivalent configuration. We established that, on substrates with low DOS at E_F like graphene, the $4f$ occupation of lanthanide atoms follows the trend in their atomic correction energy, given by the sum of the $f-d$ promotion energy and the intershell coupling energy. For Tb, this value is about three times smaller than for other investigated lanthanide atoms [104]. Hence, unlike the other atoms, Tb readily promotes one electron from the inner $4f$ into the outer spd shell and assumes a trivalent configuration. The $4f$ occupation of divalent lanthanide atoms is readily changed by the change in their coordination. An increase in the coordination, either via cluster formation or attachment of contaminants leads to the promotion of the trivalent configuration. This was especially important while performing experiments, as contamination during sample preparation or prolonged exposure to the residual gas of the UHV environment lead to erroneous measurements.

The magnetic stability of lanthanide atoms is governed by their quantum level structure,

Conclusion and outlook

in particular their ground state and the height of the energy barrier required for thermally assisted magnetization reversal, U_{rev} . As a general rule, this barrier is much smaller than the total zero field splitting of the J_z levels in the crystal field as coupling among these levels, induced by the transverse crystal field parameters, facilitates magnetization reversal either via QTM or through spin scattering with electrons and phonons of the substrate. We have established that, in the C_{6v} symmetry, for both integer and non-integer J systems U_{rev} is limited by the first excited states enabling the thermally assisted QTM.

If U_{rev} is sufficiently large, it will result in a long magnetic lifetime. Among the studied atoms on graphene/Ir(111), Dy atoms show the largest U_{rev} of 5.6 meV. This resulted in their magnetic lifetime of about 1000 s at 2.5 K. Ho atoms, with U_{rev} of 4.2 meV, have an estimated lifetime of about 1.2 s; however, due to the experimental restrictions, this lifetime is too short to be observed in our measurements. All other systems have smaller U_{rev} and shorter lifetimes.

The interaction of graphene with the supporting substrate greatly influences the splitting of the magnetic levels of an adsorbed atom, and consequently its magnetic lifetime, by altering the surrounding crystal field. Replacing weakly coupled graphene/Ir(111) with strongly hybridized graphene/Ru(0001) completely quenches the magnetic lifetime and hysteresis of adsorbed Dy atoms. In the case of weakly bound HOPG, a small variation in crystal field sufficiently reduces U_{rev} to quench the remanence, whereas hysteresis still persists in the magnetization curve.

The magnetic lifetime is in addition strongly affected by the doping of the supporting substrate. Based on the characteristics of acquired hysteresis, graphene/Ir(111) and graphene/Cu provide comparable crystal field environments to the adsorbed Dy atoms. However, the n -doping of graphene/Cu surface is larger and provides more scattering events, resulting in shorter lifetime over the entire area of hysteresis for Dy atoms on this surface. The question of magnetic remanence for this system, due to the inability to unambiguously interpret its hysteresis around $B = 0$ T, is still open and it requires further measurements.

Large electronic screening from the metallic substrate, if not accompanied with an appropriate crystal field symmetry, will not result in long magnetic lifetime of adsorbed atoms. h -BN provides a superior electronic screening with its band gap of about 6 eV [98]. However, it also provides a lower, C_{3v} crystal field symmetry which enables magnetization reversal with a single scattering event. As a consequence, no magnetic remanence or hysteresis is observed for Dy atoms on this surface. Likewise, such superior decoupling did not result in a long magnetization lifetime for Co atoms, where it generally results in a small magnetic anisotropy, regardless of the substrate upon which h -BN is grown.

Dy single atom magnets can be ordered into a regular pattern using the moiré superstructure of the graphene/Ir(111) surface as a template for their self-assembly. When deposited on a surface kept at a temperature between 30 and 50 K, Dy atoms form a well-ordered superlattice. Their separation is given by the periodicity of the moiré superstructure and it amounts to about 2.5 nm. Dy atoms in these superlattices have identical magnetic properties to those in disordered systems, proving that they indeed are non-interacting. To this day this represents

the only known example of a superlattice of single atomic magnets.

The magnetic lifetime studied in this work is commonly referred to as spin-lattice relaxation time, T_1 , and it marks the time needed for a system to relax to its steady state population, given by the thermal distribution at a given temperature. In addition to T_1 , there is another relaxation time of importance, called phase coherence time, T_2 . T_2 refers to the lifetime of a superposition of quantum states and its value is bound by T_1 , $T_2 \leq T_1$ [119]. This value is of particular importance in quantum computing as it limits the available time for computation. In case of surface supported atoms, to this day, T_2 has only been measured for Fe atoms adsorbed on MgO/Ag(100) [120] by employing electron paramagnetic resonance (EPR) spectroscopy. Considering the long T_1 of Dy atoms on graphene/Ir(111), it would be of great interest to measure their value of T_2 time.

A Crystal field parameters

In this appendix the parameters of point charge crystal fields used in multiplet calculations for transition metal and lanthanide atoms on supporting substrates are given.

Table A.1 – Point charge CF scheme employed in multiplet calculations for Dy on graphene/Ir(111).

x (Å)	y (Å)	z (Å)	q (e)
+0.00	+0.000000	-2.0	+0.13
+1.4	+0.000000	-2.0	-0.22
-1.4	-0.000000	-2.0	-0.22
+0.7	+1.212436	-2.0	-0.22
+0.7	-1.212436	-2.0	-0.22
-0.7	+1.212436	-2.0	-0.22
-0.7	-1.212436	-2.0	-0.22
+2.8	+0.000000	-2.5	+0.09
-2.8	-0.000000	-2.5	+0.09
+1.4	+2.424871	-2.5	+0.09
+1.4	-2.424871	-2.5	+0.09
-1.4	+2.424871	-2.5	+0.09
-1.4	-2.424871	-2.5	+0.09
+2.8	+2.424871	-2.5	-0.01
+2.8	-2.424871	-2.5	-0.01
+3.5	+1.212436	-2.5	-0.01
+3.5	-1.212436	-2.5	-0.01
+0.7	+3.637307	-2.5	-0.01
+0.7	-3.637307	-2.5	-0.01
-0.7	+3.637307	-2.5	-0.01
-0.7	-3.637307	-2.5	-0.01
-2.8	+2.424871	-2.5	-0.01
-2.8	-2.424871	-2.5	-0.01
-3.5	+1.212436	-2.5	-0.01
-3.5	-1.212436	-2.5	-0.01

Appendix A. Crystal field parameters

Table A.2 – Point charge CF scheme employed in multiplet calculations for Dy on *h*-BN/Ir(111).

x (Å)	y (Å)	z (Å)	q (e)
+0.000	+0.000000	-2.25	+2.8
+1.450	+0.000000	-2.25	-2.7
-0.725	-1.255737	-2.25	-2.7
-0.725	+1.255737	-2.25	-2.7
-1.450	+0.000000	-2.25	+0.1
+0.725	-1.255737	-2.25	+0.1
+0.725	+1.255737	-2.25	+0.1

Table A.3 – Point charge CF scheme employed in multiplet calculations for Nd on graphene/Ir(111).

x (Å)	y (Å)	z (Å)	q (e)
1.4	0	-0.5	-0.025
-1.4	0	-0.5	-0.025
0.7	1.212436	-0.5	-0.025
0.7	-1.212436	-0.5	-0.025
-0.7	1.212436	-0.5	-0.025
-0.7	-1.212436	-0.5	-0.025

Table A.4 – Point charge CF scheme employed in multiplet calculations for Ho on graphene/Ir(111).

x (Å)	y (Å)	z (Å)	q (e)
0	0	-2	-0.05
1.4	0	-2.5	-0.12
-1.4	0	-2.5	-0.12
0.7	1.212436	-2.5	-0.12
0.7	-1.212436	-2.5	-0.12
-0.7	1.212436	-2.5	-0.12
-0.7	-1.212436	-2.5	-0.12
0	1.4	-1.07	0.25
0	-1.4	-1.07	0.25
1.212436	0.7	-1.07	0.25
-1.212436	0.7	-1.07	0.25
1.212436	-0.7	-1.07	0.25
-1.212436	-0.7	-1.07	0.25

Table A.5 – Point charge CF scheme employed in multiplet calculations for Er on graphene/Ir(111).

x (Å)	y (Å)	z (Å)	q (e)
0	0	-1.3	-0.0235
1.4	0	-2.0	0.01
-1.4	0	-2.0	0.01
0.7	1.212436	-2.0	0.01
0.7	-1.212436	-2.0	0.01
-0.7	1.212436	-2.0	0.01
-0.7	-1.212436	-2.0	0.01
0	1.4	-1.5	-0.002
0	-1.4	-1.5	-0.002
1.212436	0.7	-1.5	-0.002
-1.212436	0.7	-1.5	-0.002
1.212436	-0.7	-1.5	-0.002
-1.212436	-0.7	-1.5	-0.002

Table A.6 – Point charge CF scheme employed in multiplet calculations for Tb on graphene/Ir(111).

x (Å)	y (Å)	z (Å)	q (e)
0	0	-1.5	-0.017
1.4	0	-1.5	0.034
-1.4	0	-1.5	0.034
0.7	1.212436	-1.5	0.034
0.7	-1.212436	-1.5	0.034
-0.7	1.212436	-1.5	0.034
-0.7	-1.212436	-1.5	0.034

Table A.7 – Point charge CF scheme employed in multiplet calculations for Co on h -BN/Ru(0001).

x (Å)	y (Å)	z (Å)	q (e)
+0.725	+1.255737	-2.5	-2.8
+0.725	-1.255737	-2.5	-2.8
-1.450	+0.000000	-2.5	-2.8
+1.450	+0.000000	-2.5	2.8
-0.725	-1.255737	-2.5	2.8
-0.725	+1.255737	-2.5	2.8
+0.000	+0.000000	-2.9	0.27

Appendix A. Crystal field parameters

Table A.8 – Point charge CF scheme employed in multiplet calculations for Co on *h*-BN/Ir(111).

x (Å)	y (Å)	z (Å)	q (e)
+0.725	+1.255737	-2.5	-2.8
+0.725	-1.255737	-2.5	-2.8
-1.450	+0.000000	-2.5	-2.8
+1.450	+0.000000	-2.5	2.8
-0.725	-1.255737	-2.5	2.8
-0.725	+1.255737	-2.5	2.8
+0.000	+0.000000	-3.0	0.27

B Tunnel splitting $\Delta_{7,-8}$ for Dy on graphene/Ir(111)

In Section 3.5, we reported the estimated tunnel splitting between levels $J_z = \pm 7$ and $J_z = \mp 8$ at $B = \pm 2.7$ T, $\Delta_{\pm 7, \mp 8}$ in case of Dy atoms on graphene/Ir(111) from the Landau-Zener model [83, 84]. Here we present the full calculation.

From the Landau-Zener formula, shown in Section 3.5, the tunnel splitting can be expressed in the following way:

$$\Delta = \sqrt{\frac{-\ln(1-P)}{\pi}} \sqrt{2\hbar g \mu_B |J_z - J_{z'}| \dot{B}_z}. \quad (\text{B.1})$$

The following values are used in calculation:

$$\mu_B = 5.79 \times 10^{-5} \text{ eV/T}$$

$$\hbar = 6.58 \times 10^{-16} \text{ eV s}$$

$$\dot{B}_z = 0.033 \text{ T/s}$$

$$|J_z - J_{z'}| = 15.$$

The Landé factor can be calculated from the following formula [18]:

$$g = \frac{3}{2} + \frac{S(S+1) - L(L+1)}{2J(J+1)} \quad (\text{B.2})$$

where moments for divalent Dy atoms are used, $J = 8$, $L = 6$ and $S = 2$. This gives $g = 1.25$.

The tunneling probability P between $J_z = \pm 7$ and $J_z = \mp 8$ levels can be estimated from the height of the corresponding step in the Dy magnetization curve. Figure B.1 shows the step at $B = -2.7$ T where levels $J_z = -7$ and $J_z = 8$ cross. The height h_1 in Figure B.1 is proportional to the total number of spins that are available for tunneling before the level crossing, while h_2 is proportional to the number of spins that have tunneled at the level crossing. The ratio of these two values gives their tunneling probability, $P = 0.71$. Hence, the tunnel splitting between

Appendix B. Tunnel splitting $\Delta_{7,-8}$ for Dy on graphene/Ir(111)

levels $J_z = \pm 7$ and $J_z = \mp 8$ at $B = \pm 2.7$ T resulting from Equation B.1 is $\Delta_{\pm 7, \mp 8} = 1.4 \times 10^{-7}$ meV. Note that, due to an unintentional error made in calculation, this value differs from the one reported in [121].

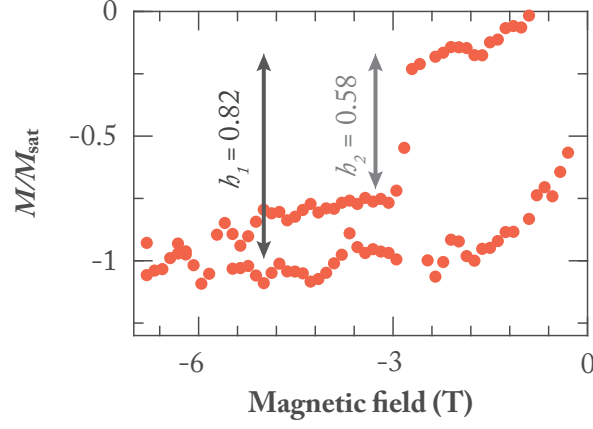


Figure B.1 – The magnetic hysteresis of Dy atoms on graphene/Ir(111) for magnetic fields between $B = -6.8$ T and $B = 0$ T. h_1 marks the height of the normalized magnetization before the step, while h_2 marks the height of the step in the hysteresis.

Bibliography

- [1] T. Komeda, H. Isshiki, J. Liu, Y.-F. Zhang, N. Lorente, K. Katoh, B. K. Breedlove, and M. Yamashita. *Observation and electric current control of a local spin in a single-molecule magnet*. Nat. Commun. 2, 217 (2011).
- [2] C. Wackerlin, F. Donati, A. Singha, R. Baltic, S. Rusponi, K. Diller, F. Patthey, M. Pivetta, Y. Lan, S. Klyatskaya, M. Ruben, H. Brune, and J. Dreiser. *Giant Hysteresis of Single-Molecule Magnets Adsorbed on a Nonmagnetic Insulator*. Adv. Mater. 28, 5195–5199 (2016).
- [3] P. Gambardella, S. Stepanow, A. Dmitriev, J. Honolka, F. M. F. de Groot, M. Lingenfelder, S. S. Gupta, D. D. Sarma, P. Bencok, S. Stanescu, S. Clair, S. Pons, N. Lin, A. P. Seitsonen, H. Brune, J. V. Barth, and K. Kern. *Supramolecular control of the magnetic anisotropy in two-dimensional high-spin Fe arrays at a metal interface*. Nat. Mater. 8, 189 (2009).
- [4] P. Gambardella, S. Rusponi, M. Veronese, S. S. Dhesi, C. Grazioli, A. Dallmeyer, I. Cabria, R. Zeller, P. H. Dederichs, K. Kern, C. Carbone, and H. Brune. *Giant Magnetic Anisotropy of Single Cobalt Atoms and Nanoparticles*. Science 300, 1130–1133 (2003).
- [5] C. F. Hirjibehedin, C.-Y. Lin, A. F. Otte, M. Ternes, C. P. Lutz, B. A. Jones, and A. J. Heinrich. *Large Magnetic Anisotropy of a Single Atomic Spin Embedded in a Surface Molecular Network*. Science 317, 1199–1203 (2007).
- [6] A. F. Otte, M. Ternes, K. von Bergmann, S. Loth, H. Brune, C. P. Lutz, C. F. Hirjibehedin, and A. J. Heinrich. *The role of magnetic anisotropy in the Kondo effect*. Nat. Phys. 4, 847–850 (2008).
- [7] B. Bryant, A. Spinelli, J. J. T. Wagenaar, M. Gerrits, and A. F. Otte. *Local Control of Single Atom Magnetocrystalline Anisotropy*. Phys. Rev. Lett. 111, 127203 (2013).
- [8] I. G. Rau, S. Baumann, S. Rusponi, F. Donati, S. Stepanow, L. Gragnaniello, J. Dreiser, C. Piamonteze, F. Nolting, S. Gangopadhyay, O. R. Albertini, R. M. Macfarlane, C. P. Lutz, B. A. Jones, P. Gambardella, A. J. Heinrich, and H. Brune. *Reaching the magnetic anisotropy limit of a 3d metal atom*. Science 344, 988–992 (2014).

Bibliography

- [9] A. A. Khajetoorians, S. Lounis, B. Chilian, A. T. Costa, L. Zhou, D. L. Mills, J. Wiebe, and R. Wiesendanger. *Itinerant Nature of Atom-Magnetization Excitation by Tunneling Electrons*. Phys. Rev. Lett. 106, 037205 (2011).
- [10] F. Donati, S. Rusponi, S. Stepanow, C. Wäckerlin, A. Singha, L. Persichetti, R. Baltic, K. Diller, F. Patthey, E. Fernandes, J. Dreiser, Ž. Šljivančanin, K. Kummer, C. Nistor, P. Gambardella, and H. Brune. *Magnetic remanence in single atoms*. Science 352, 318–321 (2016).
- [11] F. Donati, A. Singha, S. Stepanow, C. Wäckerlin, J. Dreiser, P. Gambardella, S. Rusponi, and H. Brune. *Magnetism of Ho and Er Atoms on Close-Packed Metal Surfaces*. Phys. Rev. Lett. 113, 237201 (2014).
- [12] A. Singha. *Magnetic properties of surface-adsorbed single rare earth atoms, molecules, atomic scale clusters*. Ph.D. thesis, EPFL, Switzerland (2017).
- [13] J. Stöb and H. C. Siegmann. *Magnetism: From Fundamentals to Nanoscale Dynamics*. Springer (2006).
- [14] R. A. Layfield and M. Murugesu. *Lanthanides and Actinides in Molecular Magnetism*. John Wiley & Sons (2015).
- [15] H. N. Russell and F. A. Saunders. *New Regularities in the Spectra of the Alkaline Earths*. The Astrophysical Journal 61, 38 (1925).
- [16] F. Hund. *Zur Deutung der Molekelspektren. I*. Z. Physik 40, 742–764 (1927).
- [17] F. Hund. *Zur Deutung der Molekelspektren. II*. Z. Physik 42, 93–120 (1927).
- [18] J. Jensen and A. R. Mackintosh. *Rare Earth Magnetism: Structures and Excitations*. International Series of Monographs on Physics. Oxford University Press, Oxford, New York (1991).
- [19] S. Baumann, F. Donati, S. Stepanow, S. Rusponi, W. Paul, S. Gangopadhyay, I. Rau, G. Pacchioni, L. Gragnaniello, M. Pivetta, J. Dreiser, C. Piamonteze, C. P. Lutz, R. M. Macfarlane, B. A. Jones, P. Gambardella, A. J. Heinrich, and H. Brune. *Origin of Perpendicular Magnetic Anisotropy and Large Orbital Moment in Fe Atoms on MgO*. Phys. Rev. Lett. 115, 237202 (2015).
- [20] K. W. H. Stevens. *Matrix Elements and Operator Equivalents Connected with the Magnetic Properties of Rare Earth Ions*. Proc. Phys. Soc. A 65, 209 (1952).
- [21] S. K. Misra, C. P. Poole, and H. A. Farach. *A review of spin Hamiltonian forms for various point-group site symmetries*. Appl. Magn. Reson. 11, 29–46 (1996).
- [22] C. Hübner. *Single Spin Switching in Open Quantum Systems*. Ph.D. thesis, University of Hamburg (2015).

-
- [23] T. Miyamachi, T. Schuh, T. Märkl, C. Bresch, T. Balashov, A. Stöhr, C. Karlewski, S. André, M. Marthaler, M. Hoffmann, M. Geilhufe, S. Ostanin, W. Hergert, I. Mertig, G. Schön, A. Ernst, and W. Wulfschel. *Stabilizing the magnetic moment of single holmium atoms by symmetry*. Nature 503, 242–246 (2013).
- [24] L. Thomas, F. Lioni, R. Ballou, D. Gatteschi, R. Sessoli, and B. Barbara. *Macroscopic quantum tunnelling of magnetization in a single crystal of nanomagnets*. Nature 383, 145 (1996).
- [25] D. Gatteschi and R. Sessoli. *Quantum Tunneling of Magnetization and Related Phenomena in Molecular Materials*. Angew. Chem. Int. Ed. 42, 268–297 (2003).
- [26] A. Abragam and B. Bleaney. *Electron paramagnetic resonance of transition ions*. Oxford University Press, Oxford, United Kingdom (2012).
- [27] L. Ungur and L. F. Chibotaru. *Magnetic anisotropy in the excited states of low symmetry lanthanide complexes*. Phys. Chem. Chem. Phys. 13, 20086–20090 (2011).
- [28] M. N. Leuenberger and D. Loss. *Spin tunneling and phonon-assisted relaxation in Mn₁₂-acetate*. Phys. Rev. B 61, 1286–1302 (2000).
- [29] M. Mannini, F. Pineider, C. Danieli, F. Totti, L. Sorace, P. Saintavrit, M.-A. Arrio, E. Otero, L. Joly, J. C. Cezar, A. Cornia, and R. Sessoli. *Quantum tunnelling of the magnetization in a monolayer of oriented single-molecule magnets*. Nature 468, 417–421 (2010).
- [30] H. Brune and P. Gambardella. *Magnetism of individual atoms adsorbed on surfaces*. Surf. Sci. 603, 1812–1830 (2009).
- [31] B. T. Thole, G. van der Laan, and G. A. Sawatzky. *Strong Magnetic Dichroism Predicted in the M_{4,5} X-Ray Absorption Spectra of Magnetic Rare-Earth Materials*. Phys. Rev. Lett. 55, 2086–2088 (1985).
- [32] B. T. Thole, G. van der Laan, J. C. Fuggle, G. A. Sawatzky, R. C. Karnatak, and J.-M. Esteve. *3d x-ray-absorption lines and the 3d⁹4fⁿ⁺¹ multiplets of the lanthanides*. Phys. Rev. B 32, 5107–5118 (1985).
- [33] G. van der Laan, B. T. Thole, G. A. Sawatzky, J. B. Goedkoop, J. C. Fuggle, J.-M. Esteve, R. Karnatak, J. P. Remeika, and H. A. Dabkowska. *Experimental proof of magnetic x-ray dichroism*. Phys. Rev. B 34, 6529–6531 (1986).
- [34] G. Schütz, W. Wagner, W. Wilhelm, P. Kienle, R. Zeller, R. Frahm, and G. Materlik. *Absorption of circularly polarized x rays in iron*. Phys. Rev. Lett. 58, 737–740 (1987).
- [35] J. B. Goedkoop, B. T. Thole, G. van der Laan, G. A. Sawatzky, F. M. F. de Groot, and J. C. Fuggle. *Calculations of magnetic x-ray dichroism in the 3d absorption spectra of rare-earth compounds*. Phys. Rev. B 37, 2086–2093 (1988).

Bibliography

- [36] C. T. Chen, N. V. Smith, and F. Sette. *Exchange, spin-orbit, and correlation effects in the soft-x-ray magnetic-circular-dichroism spectrum of nickel*. Phys. Rev. B 43, 6785–6787 (1991).
- [37] B. T. Thole, P. Carra, F. Sette, and G. van der Laan. *X-ray circular dichroism as a probe of orbital magnetization*. Phys. Rev. Lett. 68, 1943–1946 (1992).
- [38] Y. Wu, J. Stöhr, B. D. Hermsmeier, M. G. Samant, and D. Weller. *Enhanced orbital magnetic moment on Co atoms in Co/Pd multilayers: A magnetic circular x-ray dichroism study*. Phys. Rev. Lett. 69, 2307–2310 (1992).
- [39] C. T. Chen, Y. U. Idzerda, H.-J. Lin, N. V. Smith, G. Meigs, E. Chaban, G. H. Ho, E. Pellegrin, and F. Sette. *Experimental Confirmation of the X-Ray Magnetic Circular Dichroism Sum Rules for Iron and Cobalt*. Phys. Rev. Lett. 75, 152–155 (1995).
- [40] D. Weller, J. Stöhr, R. Nakajima, A. Carl, M. G. Samant, C. Chappert, R. Mégy, P. Beauvilain, P. Veillet, and G. A. Held. *Microscopic Origin of Magnetic Anisotropy in Au/Co/Au Probed with X-Ray Magnetic Circular Dichroism*. Phys. Rev. Lett. 75, 3752–3755 (1995).
- [41] R. Nakajima. *X-ray magnetic circular dichroism spectroscopy in transition metal thin films*. Ph.D. thesis, Stanford University (1998).
- [42] P. A. M. Dirac. *The Quantum Theory of the Emission and Absorption of Radiation*. Proc. R. Soc. A 114, 243–265 (1927).
- [43] C. Brouder. *Angular dependence of X-ray absorption spectra*. J. Phys.: Condens. Matter 2, 701 (1990).
- [44] E. Beaurepaire, H. Bulou, F. Scheurer, and J.-P. Kappler, eds. *Magnetism: A Synchrotron Radiation Approach*, volume 697 of *Lecture Notes in Physics*. Springer Berlin Heidelberg (2006).
- [45] N. V. Smith, C. T. Chen, F. Sette, and L. F. Mattheiss. *Relativistic tight-binding calculations of x-ray absorption and magnetic circular dichroism at the L_2 and L_3 edges of nickel and iron*. Phys. Rev. B 46, 1023–1032 (1992).
- [46] J. Stöhr and Y. Wu. *X-Ray Magnetic Circular Dichroism: Basic Concepts and Theory for 3D Transition Metal Atoms*. In *New Directions in Research with Third-Generation Soft X-Ray Synchrotron Radiation Sources*, NATO ASI Series, 221–250. Springer, Dordrecht (1994).
- [47] G. van der Laan. *Magnetic Linear X-Ray Dichroism as a Probe of the Magnetocrystalline Anisotropy*. Phys. Rev. Lett. 82, 640–643 (1999).
- [48] P. Carra, B. T. Thole, M. Altarelli, and X. Wang. *X-ray circular dichroism and local magnetic fields*. Phys. Rev. Lett. 70, 694–697 (1993).

-
- [49] P. Carra, H. König, B. T. Thole, and M. Altarelli. *Magnetic X-ray dichroism: General features of dipolar and quadrupolar spectra*. Physica B 192, 182–190 (1993).
- [50] C. Piamonteze, U. Flechsig, S. Rusponi, J. Dreiser, J. Heidler, M. Schmidt, R. Wetter, M. Calvi, T. Schmidt, H. Pruchova, J. Krempasky, C. Quitmann, H. Brune, and F. Nolting. *X-Treme beamline at SLS: X-ray magnetic circular and linear dichroism at high field and low temperature*. J. Synchrotron Rad. 19, 661–674 (2012).
- [51] J. Coraux, A. T. N'Diaye, C. Busse, and T. Michely. *Structural Coherency of Graphene on Ir(111)*. Nano Lett. 8, 565–570 (2008).
- [52] F. D. Natterer, S. Rusponi, M. Papagno, C. Carbone, and H. Brune. *Optimizing long-range order, band gap, and group velocities for graphene on close-packed metal surfaces*. J. Phys.: Condens. Matter 24, 314203 (2012).
- [53] M. Corso, W. Auwärter, M. Muntwiler, A. Tamai, T. Greber, and J. Osterwalder. *Boron Nitride Nanomesh*. Science 303, 217–220 (2004).
- [54] A. Goriachko, He, M. Knapp, H. Over, M. Corso, T. Brugger, S. Berner, J. Osterwalder, and T. Greber. *Self-Assembly of a Hexagonal Boron Nitride Nanomesh on Ru(0001)*. Langmuir 23, 2928–2931 (2007).
- [55] M. Weissbluth. *Atoms and Molecules*. Academic Press, New York (1978).
- [56] R. D. Cowan. *The Theory of Atomic Structure and Spectra*. University of California Press (1981).
- [57] C. J. Ballhausen. *Introduction to Ligand Field Theory*. McGraw-Hill (1962).
- [58] S. Sugano. *Multiplets of Transition-Metal Ions in Crystals*. Academic Press, New York (1972).
- [59] F. De Groot. *High-resolution X-ray emission and X-ray absorption spectroscopy*. Chem. Rev. 101, 1779–1808 (2001).
- [60] F. de Groot and J. Vogel. *Fundamentals of X-ray Absorption and Dichroism: The Multiplet Approach*. In F. Hippert, E. Geissler, J. L. Hodeau, E. Lelièvre-Berna, and J.-R. Regnard, eds., *Neutron and X-ray Spectroscopy*, 3–66. Springer Netherlands, Dordrecht (2006).
- [61] N. F. Chilton, D. Collison, E. J. L. McInnes, R. E. P. Winpenny, and A. Soncini. *An electrostatic model for the determination of magnetic anisotropy in dysprosium complexes*. Nat. Commun. 4, 2551 (2013).
- [62] J. J. Baldoví, J. M. Clemente-Juan, E. Coronado, and A. Gaita-Ariño. *Molecular Anisotropy Analysis of Single-Ion Magnets Using an Effective Electrostatic Model*. Inorg. Chem. 53, 11323 (2014).

Bibliography

- [63] A. Uldry, F. Vernay, and B. Delley. *Systematic computation of crystal-field multiplets for X-ray core spectroscopies*. Phys. Rev. B 85, 125133 (2012).
- [64] R. Gaisch, J. K. Gimzewski, B. Reihl, R. R. Schlittler, M. Tschudy, and W. D. Schneider. *Low-temperature ultra-high vacuum scanning tunneling microscope*. Ultramicroscopy 42-44, 1621 (1992).
- [65] R. Brako, D. Šokčević, P. Lazić, and N. Atodiresei. *Graphene on the Ir(111) surface: from van der Waals to strong bonding*. New J. Phys. 12, 113016 (2010).
- [66] A. T. N'Diaye, S. Bleikamp, P. J. Feibelman, and T. Michely. *Two-Dimensional Ir Cluster Lattice on a Graphene Moiré on Ir(111)*. Phys. Rev. Lett. 97, 215501 (2006).
- [67] A. T. N'Diaye, J. Coraux, T. N. Plasa, C. Busse, and T. Michely. *Structure of epitaxial graphene on Ir(111)*. New J. Phys. 10, 043033 (2008).
- [68] C. Busse, P. Lazić, R. Djemour, J. Coraux, T. Gerber, N. Atodiresei, V. Caciuc, R. Brako, A. T. N'Diaye, S. Blügel, J. Zegenhagen, and T. Michely. *Graphene on Ir(111): Physisorption with Chemical Modulation*. Phys. Rev. Lett. 107, 036101 (2011).
- [69] M. Hupalo, X. Liu, C.-Z. Wang, W.-C. Lu, Y.-X. Yao, K.-M. Ho, and M. C. Tringides. *Metal Nanostructure Formation on Graphene: Weak versus Strong Bonding*. Adv. Mater. 23, 2082 (2011).
- [70] X. Liu, C.-Z. Wang, M. Hupalo, H.-Q. Lin, K.-M. Ho, and M. C. Tringides. *Metals on Graphene: Interactions, Growth Morphology, and Thermal Stability*. Crystals 3, 79–111 (2013).
- [71] M. Pivetta, S. Rusponi, and H. Brune. *Self-assembled Superlattices of Rare-Earth Atoms on Graphene*. In preparation .
- [72] C.-L. Song, B. Sun, Y.-L. Wang, Y.-P. Jiang, L. Wang, K. He, X. Chen, P. Zhang, X.-C. Ma, and Q.-K. Xue. *Charge-Transfer-Induced Cesium Superlattices on Graphene*. Phys. Rev. Lett. 108, 156803 (2012).
- [73] S. Pichler, M. I. Bodnarchuk, M. V. Kovalenko, M. Yarema, G. Springholz, T. D. V., and W. Heiss. *Evaluation of ordering in single-component and binary nanocrystal superlattices by analysis of their autocorrelation functions*. ACS Nano 5, 1703 (2011).
- [74] J. Dreiser, R. Westerström, C. Piamonteze, F. Nolting, S. Rusponi, H. Brune, S. Yang, A. Popov, L. Dunsch, and T. Greber. *X-ray induced demagnetization of single-molecule magnets*. Appl. Phys. Lett. 105, 032411 (2014).
- [75] C. Hübner, B. Baxevanis, A. A. Khajetoorians, and D. Pfannkuche. *Symmetry effects on the spin switching of adatoms*. Phys. Rev. B 90, 155134 (2014).

-
- [76] N. Ishikawa, M. Sugita, and W. Wernsdorfer. *Quantum Tunneling of Magnetization in Lanthanide Single-Molecule Magnets: Bis(phthalocyaninato)terbium and Bis(phthalocyaninato)dysprosium Anions*. *Angew. Chem. Int. Ed.* 44, 2931–2935 (2005).
- [77] M. Endlich, A. Molina-Sánchez, L. Wirtz, and J. Kröger. *Screening of electron-phonon coupling in graphene on Ir(111)*. *Phys. Rev. B* 88, 205403 (2013).
- [78] L. Chen, Z. Huang, and S. Kumar. *Phonon transmission and thermal conductance across graphene/Cu interface*. *Appl. Phys. Lett.* 103, 123110 (2013).
- [79] S. Rusponi, M. Papagno, P. Moras, S. Vlaic, M. Etzkorn, P. M. Sheverdyaeva, D. Pacilé, H. Brune, and C. Carbone. *Highly Anisotropic Dirac Cones in Epitaxial Graphene Modulated by an Island Superlattice*. *Phys. Rev. Lett.* 105, 246803 (2010).
- [80] S. K. Hämäläinen, M. Stepanova, R. Drost, P. Liljeroth, J. Lahtinen, and J. Sainio. *Self-Assembly of Cobalt-Phthalocyanine Molecules on Epitaxial Graphene on Ir(111)*. *J. Phys. Chem. C* 116, 20433–20437 (2012).
- [81] B. Uchoa, L. Yang, S.-W. Tsai, N. M. R. Peres, and A. H. Castro Neto. *Orbital symmetry fingerprints for magnetic adatoms in graphene*. *New J. Phys.* 16, 013045 (2014).
- [82] C. Cervetti, A. Rettori, M. G. Pini, A. Cornia, A. Repollés, F. Luis, M. Dressel, S. Rauschenbach, K. Kern, M. Burghard, and L. Bogani. *The classical and quantum dynamics of molecular spins on graphene*. *Nat. Mater.* 15, 164 (2016).
- [83] W. Wernsdorfer and R. Sessoli. *Quantum Phase Interference and Parity Effects in Magnetic Molecular Clusters*. *Science* 284, 133–135 (1999).
- [84] W. Wernsdorfer, R. Sessoli, A. Caneschi, D. Gatteschi, and A. Cornia. *Nonadiabatic Landau-Zener tunneling in Fe₈ molecular nanomagnets*. *Europhys. Lett.* 50, 552 (2000).
- [85] A. Singha, R. Baltic, F. Donati, C. Wäckerlin, J. Dreiser, L. Persichetti, S. Stepanow, P. Gambardella, S. Rusponi, and H. Brune. *4f occupancy and magnetism of rare-earth atoms adsorbed on metal substrates*. *Phys. Rev. B* 96, 224418 (2017).
- [86] H. Brune. *Microscopic view of epitaxial metal growth: nucleation and aggregation*. *Surf. Sci. Rep.* 31, 125 – 229 (1998).
- [87] A. Singha, F. Donati, C. Wäckerlin, R. Baltic, J. Dreiser, M. Pivetta, S. Rusponi, and H. Brune. *Magnetic Hysteresis in Er Trimers on Cu(111)*. *Nano Lett.* 16, 3475–3481 (2016).
- [88] M. Domke, C. Laubschat, M. Prietsch, T. Mandel, G. Kaindl, and W. D. Schneider. *Experimental Proof for Coordination-Dependent Valence of Tm Metal*. *Phys. Rev. Lett.* 56, 1287–1290 (1986).
- [89] G. Giovannetti, P. A. Khomyakov, G. Brocks, V. M. Karpan, J. van den Brink, and P. J. Kelly. *Doping Graphene with Metal Contacts*. *Phys. Rev. Lett.* 101, 026803 (2008).

Bibliography

- [90] P. A. Khomyakov, G. Giovannetti, P. C. Rusu, G. Brocks, J. van den Brink, and P. J. Kelly. *First-principles study of the interaction and charge transfer between graphene and metals*. Phys. Rev. B 79, 195425 (2009).
- [91] M. Petrović, P. Lazić, S. Runte, T. Michely, C. Busse, and M. Kralj. *Moiré-regulated self-assembly of cesium adatoms on epitaxial graphene*. Phys. Rev. B 96, 085428 (2017).
- [92] B. Wang, M.-L. Bocquet, S. Marchini, S. Gunther, and J. Wintterlin. *Chemical origin of a graphene moire overlayer on Ru(0001)*. Phys. Chem. Chem. Phys. 10, 3530–3534 (2008).
- [93] S. J. Altenburg, J. Kröger, B. Wang, M.-L. Bocquet, N. Lorente, and R. Berndt. *Graphene on Ru(0001): Contact Formation and Chemical Reactivity on the Atomic Scale*. Phys. Rev. Lett. 105, 236101 (2010).
- [94] D. Martoccia, P. R. Willmott, T. Brugger, M. Björck, S. Günther, C. M. Schlepütz, A. Cervellino, S. A. Pauli, B. D. Patterson, S. Marchini, J. Wintterlin, W. Moritz, and T. Greber. *Graphene on Ru(0001): A 25×25 Supercell*. Phys. Rev. Lett. 101, 126102 (2008).
- [95] A. L. Vázquez de Parga, F. Calleja, B. Borca, M. C. G. Passeggi, J. J. Hinarejos, F. Guinea, and R. Miranda. *Periodically Rippled Graphene: Growth and Spatially Resolved Electronic Structure*. Phys. Rev. Lett. 100, 056807 (2008).
- [96] B. Borca, S. Barja, M. Garnica, J. J. Hinarejos, A. L. V. d. Parga, R. Miranda, and F. Guinea. *Periodically modulated geometric and electronic structure of graphene on Ru(0001)*. Semicond. Sci. Technol. 25, 034001 (2010).
- [97] A. G. Güell, S.-y. Tan, P. R. Unwin, and G. Zhang. *Electrochemistry at Highly Oriented Pyrolytic Graphite (HOPG): Toward a New Perspective*. In R. C. Alkire, P. N. Bartlett, and J. Lipkowski, eds., *Electrochemistry of Carbon Electrodes*, 31–82. Wiley-VCH Verlag GmbH & Co. KGaA (2015).
- [98] B. Arnaud, S. Lebègue, P. Rabiller, and M. Alouani. *Huge Excitonic Effects in Layered Hexagonal Boron Nitride*. Phys. Rev. Lett. 96, 026402 (2006).
- [99] T. Brugger, S. Günther, B. Wang, J. H. Dil, M.-L. Bocquet, J. Osterwalder, J. Wintterlin, and T. Greber. *Comparison of electronic structure and template function of single-layer graphene and a hexagonal boron nitride nanomesh on Ru(0001)*. Phys. Rev. B 79, 045407 (2009).
- [100] J. G. Díaz, Y. Ding, R. Koitz, A. P. Seitsonen, M. Iannuzzi, and J. Hutter. *Hexagonal boron nitride on transition metal surfaces*. Theor. Chem. Acc. 132, 1350 (2013).
- [101] F. Schulz, R. Drost, S. K. Hämäläinen, T. Demonchaux, A. P. Seitsonen, and P. Liljeroth. *Epitaxial hexagonal boron nitride on Ir(111): A work function template*. Phys. Rev. B 89, 235429 (2014).

-
- [102] A. L. Kozub, A. B. Shick, F. Máca, J. Kolorenč, and A. I. Lichtenstein. *Electronic structure and magnetism of samarium and neodymium adatoms on free-standing graphene*. Phys. Rev. B 94, 125113 (2016).
- [103] E. M. Chudnovsky, D. A. Garanin, and R. Schilling. *Universal mechanism of spin relaxation in solids*. Phys. Rev. B 72, 094426 (2005).
- [104] A. Delin, L. Fast, B. Johansson, J. M. Wills, and O. Eriksson. *Method for Calculating Valence Stability in Lanthanide Systems*. Phys. Rev. Lett. 79, 4637–4640 (1997).
- [105] L. Peters, I. Di Marco, M. S. Litsarev, A. Delin, M. I. Katsnelson, A. Kirilyuk, B. Johansson, B. Sanyal, and O. Eriksson. *Valence and spectral properties of rare-earth clusters*. Phys. Rev. B 92, 035143 (2015).
- [106] L. Peters, S. Ghosh, B. Sanyal, C. van Dijk, W. de Heer, A. Delin, I. Di Marco, O. Eriksson, M. I. Katsnelson, B. Johansson, and A. Kirilyuk. *Magnetism and exchange interaction of small rare-earth clusters; Tb as a representative*. Sci. Rep. 6, 19676 (2016).
- [107] S. Stepanow, J. Honolka, P. Gambardella, L. Vitali, N. Abdurakhmanova, T.-C. Tseng, S. Rauschenbach, S. L. Tait, V. Sessi, S. Klyatskaya, M. Ruben, and K. Kern. *Spin and Orbital Magnetic Moment Anisotropies of Monodispersed Bis(Phthalocyaninato)Terbium on a Copper Surface*. J. Am. Chem. Soc. 132, 11900–11901 (2010).
- [108] F. Donati, Q. Dubout, G. Autès, F. Patthey, F. Calleja, P. Gambardella, O. V. Yazyev, and H. Brune. *Magnetic Moment and Anisotropy of Individual Co Atoms on Graphene*. Phys. Rev. Lett. 111, 236801 (2013).
- [109] P. Gambardella, S. S. Dhesi, S. Gardonio, C. Grazioli, P. Ohresser, and C. Carbone. *Localized Magnetic States of Fe, Co, and Ni Impurities on Alkali Metal Films*. Phys. Rev. Lett. 88, 047202 (2002).
- [110] F. d. Groot and A. Kotani. *Core Level Spectroscopy of Solids*. CRC Press (2008).
- [111] A. Lehnert, S. Rusponi, M. Etzkorn, S. Ouazi, P. Thakur, and H. Brune. *Magnetic anisotropy of Fe and Co adatoms and Fe clusters magnetically decoupled from Ni₃Al(111) by an alumina bilayer*. Phys. Rev. B 81, 104430 (2010).
- [112] M. Etzkorn, C. F. Hirjibehedin, A. Lehnert, S. Ouazi, S. Rusponi, S. Stepanow, P. Gambardella, C. Tieg, P. Thakur, A. I. Lichtenstein, A. B. Shick, S. Loth, A. J. Heinrich, and H. Brune. *Comparing XMCD and DFT with STM spin excitation spectroscopy for Fe and Co adatoms on Cu₂N/Cu(100)*. Phys. Rev. B 92, 184406 (2015).
- [113] A. Barla, V. Bellini, S. Rusponi, P. Ferriani, M. Pivetta, F. Donati, F. Patthey, L. Persichetti, S. K. Mahatha, M. Papagno, C. Piamonteze, S. Fichtner, S. Heinze, P. Gambardella, H. Brune, and C. Carbone. *Complex Magnetic Exchange Coupling between Co Nanostructures and Ni(111) across Epitaxial Graphene*. ACS Nano 10, 1101–1107 (2016).

Bibliography

- [114] P. Jacobson, T. Herden, M. Muenks, G. Laskin, O. Brovko, V. Stepanyuk, M. Ternes, and K. Kern. *Quantum engineering of spin and anisotropy in magnetic molecular junctions*. Nat. Commun. 6, 8536 (2015).
- [115] O. V. Yazyev and A. Pasquarello. *Metal adatoms on graphene and hexagonal boron nitride: Towards rational design of self-assembly templates*. Phys. Rev. B 82, 045407 (2010).
- [116] Y. Hwang and Y.-C. Chung. *Comparative study of metal atom adsorption on free-standing h-BN and h-BN/Ni (111) surfaces*. Appl. Surf. Sci. 299, 29–34 (2014).
- [117] E. Fernandes, F. Donati, F. Patthey, S. Stavrić, Ž. Šljivančanin, and H. Brune. *Adsorption sites of individual metal atoms on ultrathin MgO(100) films*. Phys. Rev. B 96, 045419 (2017).
- [118] N. Ishikawa, M. Sugita, T. Okubo, N. Tanaka, T. Iino, and Y. Kaizu. *Determination of Ligand-Field Parameters and f-Electronic Structures of Double-Decker Bis(phthalocyaninato)lanthanide Complexes*. Inorg. Chem. 42, 2440–2446 (2003).
- [119] T. D. Ladd, F. Jelezko, R. Laflamme, Y. Nakamura, C. Monroe, and J. L. O’Brien. *Quantum computers*. Nature 464, 45–53 (2010).
- [120] S. Baumann, W. Paul, T. Choi, C. P. Lutz, A. Ardavan, and A. J. Heinrich. *Electron paramagnetic resonance of individual atoms on a surface*. Science 350, 417–420 (2015).
- [121] R. Baltic, M. Pivetta, F. Donati, C. Wäckerlin, A. Singha, J. Dreiser, S. Rusponi, and H. Brune. *Superlattice of Single Atom Magnets on Graphene*. Nano Lett. 16, 7610–7615 (2016).

Acknowledgements

I would like to thank my thesis advisor, Prof. Harald Brune, for giving me the opportunity to be part of his research group and to carry out my PhD studies at EPFL.

I would like to express my gratitude to Dr. Stefano Rusponi for co-directing my thesis project, his support throughout my studies, and for his invaluable role in the success of our synchrotron experiments. I would like to thank Dr. Marina Pivetta for her support and her STM study of Dy atoms on graphene/Ir(111).

I would particularly like to thank Dr. Fabio Donati for our countless scientific and non-scientific discussions, learning with me how to do multiplet calculations and helping me to improve my writing skills. I would like to thank Dr. Jan Dreiser, Dr. Christian Wäckerlin and Dr. Aparajita Singha for their collaboration in our XMCD projects, discussions and time shared at SLS, especially during the nightshifts. I would also like to thank all of my other LNS colleagues with whom I had the pleasure of spending time during these four years.

I would like to thank all of my friends who have accompanied me on this journey. Special thanks to Vjeran! I never even dreamed we would have (so many) lunches at Banane! And to Lada and Domagoj, for their daily support and chatting.

Hvala mami na svoj ljubavi i potpori. Bez tebe danas ne bih bila gdje jesam.

Last but not least, I would like to thank Julian. Thank you for being by my side all these years, for your patience and support. Thank you for being my companion in our adventures, for being my buddy and holding my hand in the depths of seas, and for picking me up when snow was just too hard.

Lausanne, 11 January 2018

R. B.

Curriculum Vitae

Name: Romana Baltić
Nationality: Croatian
Date of Birth: 12 January 1988

Education

2014 – 2017 Doctoral Assistant, EPFL, Lausanne, Switzerland
2006 – 2013 Master of Science in Physics, University of Zagreb, Croatia

Publications

R. Baltić, M. Pivetta, F. Donati, C. Wäckerlin, A. Singha, J. Dreiser, S. Rusponi, and H. Brune, *Superlattice of Single Atom Magnets on Graphene*, Nano Letters 16, 7610-7615 (2016).

A. Singha, **R. Baltić**, F. Donati, C. Wäckerlin, J. Dreiser, L. Persichetti, S. Stepanow, P. Gambardella, S. Rusponi, and H. Brune, *4f occupancy and magnetism of rare-earth atoms adsorbed on metal substrates*, Phys. Rev. B 96, 224418 (2017).

F. Donati, S. Rusponi, S. Stepanow, C. Wäckerlin, A. Singha, L. Persichetti, **R. Baltić**, K. Diller, F. Patthey, E. Fernandes, J. Dreiser, Ž. Šljivančanin, K. Kummer, C. Nistor, P. Gambardella, and H. Brune, *Magnetic remanence in single atoms*, Science 352, 318-321 (2016).

C. Wäckerlin, F. Donati, A. Singha, **R. Baltić**, S. Rusponi, K. Diller, F. Patthey, M. Pivetta, Y. Lan, S. Klyatskaya, M. Ruben, H. Brune and J. Dreiser, *Giant Hysteresis of Single-Molecule Magnets Adsorbed on a Nonmagnetic Insulator*, Advanced Materials 28, 5195-5199 (2016).

A. Singha, F. Donati, C. Wäckerlin, **R. Baltić**, J. Dreiser, M. Pivetta, S. Rusponi, and H. Brune, *Magnetic hysteresis in Er trimers on Cu(111)*, Nano Letters 16, 3475 (2016).

C. Wäckerlin, F. Donati, A. Singha, **R. Baltić**, A.-C. Uldry, B. Delley, S. Rusponi and J. Dreiser, *Strong antiferromagnetic exchange between manganese phthalocyanine and ferromagnetic europium oxide*, Chem. Commun. 51 12958 (2015).